Robird Wind Tunnel Test Setup Design

C.S.E. (Cyrano) Vaseur

MSc Report

Committee:
Prof.dr.ir. S. Stramigioli
Ir. G.A. Folkertsma
Prof.dr.ir. H.W.M. Hoeijmakers

November 2014

Report nr. 020RAM2014
Robotics and Mechatronics
EE-Math-CS
University of Twente
P.O. Box 217
7500 AE Enschede
The Netherlands

Acknowledgements

After taking courses throughout the first year, the second year of the master program in Systems and Control at the University of Twente (UTwente) is continued with a three month internship and completed with a seven month graduation project. The graduation project I chose is titled “Robird wind tunnel test setup design”. Robird is a robotic bird which establishes flight through flapping. These robotic birds are manufactured by Clear Flight Solutions (CFS). The designed test setup is intended to provide insight in the (aero) dynamics of (Ro) birds, especially in the yet far from fully understood flapping flight, beneficial to both UTwente and CFS. The graduation project is intended for the student to demonstrate his/her ability to independently and creatively integrate the gained knowledge and experience during coursework and the internship while still expanding his/her own knowledge. This has been a process which would not have been possible without the help of others to whom I wish to express my thanks. According to the saying “well begun is half done” I owe Dr. Aarts and Dr. van Dijk my thanks for half the work. Our fruitful discussions on model development in Spacar and controller design enabled me a good kick-off. I thank prof. Hoeijmakers for providing me with insight on the aerodynamic requirements the setup needed to meet. I would like to thank the technicians of the faculty of Engineering Technology (CTW), Norbert Spikker, Theo Pünt, Peter Bolscher, Joop Tiehuis and Martin Spenkeler for their valuable advice on the construction of the test setup and for helping me with manufacturing some of the parts. I would like to thank Freek Tonis of Hankamp Gears for helping me customize the gears I used in the setup. I thank Rob Beltman for helping with the assembly of the setup. I say thanks to Gerben teRietogScholten for the technical advice on the construction of the setup, advice on manufacturers, ordering the parts and for the installation of the controllers and connecting the motors. Again I thank Dr. Aarts. This time for allowing me to work with the force sensor of Mechanical Automation and providing me with the necessary space (in their lab), hardware and software and helping me with the installation and initialization together with Gerald Ebberink and Bert van de Ridder. A thank you goes to Nico Nijenhuis of CFS and his personnel for their advice and enthusiasm. I say thanks to my daily supervisor Ir. Geert Folkertsma for assessing my work critically and not settling for little, allowing me to deliver good quality work. I thank my head supervisor, prof. Stramigioli, for his inspiration and giving me the opportunity and having confidence in me for doing this project. Last but not least, I thank my friends and family for their love and support especially during difficult times.

Thank you!

Cyrano Vaseur,
October 2014, Enschede, The Netherlands

In memory of my father, Erick Roy Vaseur (1954 - 2012)

Abstract

Robird is a robot bird which mimics flapping motion by two con rod mechanisms per wing which transform motor rotational motion into flapping, i.e. plunging and pitching. The latter caused by introducing a phase shift phs between the motion of the two con rod mechanisms.

To gain understanding in the (aero) dynamics of (Ro) birds, a wind tunnel test setup is designed to among others measure aerodynamic loads. In the design, the desired phase shift phs, typically between 6° and 7°, is fixed actively with a desired accuracy of $e_{max} = \pm 0.1°$. This is done through the use of two motors (2-DOF). This task is interpreted as a set-point error problem for position control with flapping frequencies f up to 7 $[\mathrm{Hz}]$.

A nonlinear model of the 2-DOF setup mechanism is developed in Spacar using a finite element formulation. Wing stiffness is modeled as a torsional spring. The model is validated through state space system identification and parameter estimation of the actual setup. Based on an identified simplified linearized model, capturing only low frequency behavior, an optimal PID controller is designed by locating its maximum phase-lead at the desired cross-over frequency dependent on the performance specifications.

However, due to limitations of the applied ELMO controllers cascaded position-velocity (PIP) control is applied instead. The results show that for frequencies up to $f = 4$ $[\mathrm{Hz}]$ the desired phase shift (up to 7°) is obtained with the desired accuracy of $\pm 0.1°$.

Finally, initial reaction force measurements with the setup show good agreement with simulations for frequencies up to $1[\mathrm{Hz}]$. For higher frequencies, the measured forces exceed the simulations. This is as expected because the developed model only captures inertia forces and stress resultants whereas the measurements in addition also capture aerodynamic loads. In this way, for wind tunnel experiments to follow, aerodynamic loads can be distinguished by subtracting the measurements with the simulations.

Contents

Summary

Robird is a flying robot bird, currently manufactured in both a peregrine falcon version and a bald eagle version (both birds of prey), which accomplishes flight through a specific flapping wing mechanism. Due to good imitation of its real life counterpart, it can be used in both espionage applications and to scare away birds from places they are undesired at, such as airports and farms.

For a single 2D wing section, bird flapping flight can be described through combined plunging and pitching motion. In Robird, this motion is mimicked by two con rod mechanisms per wing that transform the motor rotational motion into wing flapping, i.e. plunging and pitching. The pitching is caused by introducing a phase shift phs between the motions of the two con rod mechanisms. Although Robird has already achieved flight through flapping, its underlying aerodynamics are far from fully understood. To gain understanding in the (aero) dynamics of (Ro) birds, a wind tunnel test setup must be built. This has been the focus of this graduation project.

The setup to be designed should meet a number of requirements: (i) for freedom in experiments it must allow for an adjustable phase shift phs, typically between 6° and 7° with an accuracy of $e_{max} = 0.1°$ for flapping frequencies up to $f = 7$ [Hz], (ii) with it, it must be possible to measure reaction forces and torques in all directions, (iii) for interpretable measurements it must represent a symmetric half of the actual mechanism, (iv) due to wind tunnel dimensions it must be mounted under a quarter turn and (v) to reduce flow disturbances it must be provided with an aerodynamic shield.

For the first requirement, a control and mechanical solution have been combined. In the mechanical solution, the desired phase shift is fixed passively/mechanically through a frictional disc connection. In the control solution on the other hand, the desired phase shift phs is fixed actively through the use of two motors, each predominantly driving a single con rod mechanism. In this way the plant is extended from SISO to TITO. This task is interpreted as a set-point error problem for position control. The position references for both motors are ramp signals with gradients corresponding to $f = 7$ [Hz]. However there is a delay between them, corresponding to the required phase shift phs typically between 6° and 7°. Because both references are controlled individually, the allowed set-point error is set to $\frac{1}{2} \cdot e_{max} = 0.05°$. The chosen control strategy is classic SISO control design combined with decoupling. Regarding the second requirement, a 6-DOF sensor is mounted at the base of the setup and remaining requirements are incorporated into the design straightforwardly.

To tackle this position control problem, first a model of the setup mechanism is developed using a finite element formulation using computer software Spacar. The setup mechanism is constructed from elements that are connected through joint nodal and/or deformation coordinates. Hereby the wing stiffness is modeled as a simple torsional spring element. The system coordinates are partitioned in order to describe the system in terms of the degrees of freedom through geometric transfer functions. The system position, velocity and acceleration are described by means of the zeroth, first and first and second order geometric transfer functions respectively. Unlike the velocity and acceleration, the system position cannot be solved analytically due to the highly nonlinear first order geometric transfer function. The position is solved numerically using the Newton-Raphson method and taking into account only the first and second order terms. System dynamics are described by equations of motion which are derived by means of the principle of virtual work and d'Alembert's principle.

Next a PID controller is designed using an analytical one parameter method. The procedure followed here is classic SISO design combined with decoupling. As performance is a low frequency issue, first a simple, low frequency, linear model of the system is developed. This simple model is deduced from the low frequency region of the linearized system of the more elaborate nonlinear model developed in Spacar. Based on this simplified model, a PID controller is designed. Proportional control is applied to set the cross-over frequency such that desired system responsiveness is obtained. Integral control is applied to reduce or even remove the steady state error. Derivative control is applied to improve system stability by applying phase margin at the cross-over frequency. The controller is optimized by making optimal use of the maximum phase-lead. This is done by locating the frequency

at which this maximum phase-lead appears at the desired cross-over frequency. In such a way, the control parameters are expressed in terms of the desired cross-over frequency. The cross-over frequency on its turn is determined from the maximum allowed set-point error and the chosen reference through the sensitivity function. Also considered is the possible application of plant decoupling prior to SISO control application. The designed controller is tested on the nonlinear model. Hereby rough first estimations (order of magnitude) of the aerodynamic loads are introduced as plant input disturbances. Simulation results showed that the designed controller has been able to deal with these disturbances while still also achieving its target performance. I.e. for a flapping frequency of $f = 7$ [Hz] a phase shift of $phs = 7[°]$ is obtained with an accuracy of $e_{max} = \pm 0.1°$

After controller design, mechanical design of the setup is conducted. In addition, a mechanical (passive) solution of the desired phase shift is introduced as an alternative. This is done by means of an optional disc frictional connection established by preload provided through a bolt. Further, the setup is supplied with the needed gears and bearings which have been chosen based on their mechanical sufficiency, i.e. durability against gear tooth side damage and acceptable bearing lifetime respectively. The setup represents a symmetric half of the Robird mechanism, as this was necessary to obtain interpretable aerodynamic loads to be measured. This symmetric half is rotated a quarter turn in order to utilize the wind tunnel dimension optimally with regard to flow disturbances near the walls. Finally, the setup mechanism is provided with an aerodynamic shield to eliminate its flow disturbances as far as possible. This shield is fabricated out of plastic through a vacuum forming process with a designed mold.

Next, setup equipment is selected based on them meeting specific requirements. Maxon motors are chosen based on meeting power, torque, current and electric requirements. Maxon gearboxes are chosen based on meeting transmission and torque requirements. Maxon position encoders are chosen based on meeting resolution requirements. ELMO controllers are chosen based on meeting voltage and current requirements. And a 6-DOF force sensor is chosen based on range and resolution requirements.

After ordering and assembling the parts and equipment, first system identification and parameter estimation is conducted on the plant to gain confidence on the developed model and the controller designed based on it. The stable open-loop (upside-down) plant is sufficiently excited by an appropriate input signal (motor input current). There is chosen for a chirp signal (a sinusoidal signal with increasing frequency) in order to utilize a range of frequencies in one signal. The frequency range is chosen to cover all significant resonances. The signal amplitude is chosen such that the system is excited sufficiently. The sample frequency is restricted by the Nyquist frequency and the highest relevant resonance frequency. System output is measured, and together with the input, first the model order is estimated and next the state space is estimated. The results proved that the developed model fits the experiment. The estimated order (four) was as expected and is in agreement with the theory (model) and the frequency responses showed that the resonances existent in the model are also reflected by the experiment. From the cross-correlation it was found that the model estimation was correct, as this was within the confidence bounds. One obvious difference between the identified plant and the model has been the existence of damping in the actual system and the absence thereof in the model. Hence, damping estimation is conducted and the model is improved with the estimated damping.

Due to the good agreement between model and identification, it has not been necessary to redesign the PID controller. However, due to limitations of the applied ELMO controllers, application of PID controller seemed not straightforward: instead cascaded position (P) velocity (PI) control is applied. To prevent the wing from breaking, a flapping frequency of $f = 4$ [Hz] is applied in the tests. After tweaking and implementation of the PIP controller, the results show that the desired phase shift phs is obtained within ± 0.1 [°]. The performance target of ± 0.1 [°] is met. Also, from comparison with simulations, using a PIP controller with the same parameters as in the implementation, it follows that the current profiles do agree well qualitatively. However, in the simulation a much higher accuracy is obtained. This raises the suspicion of higher loads and disturbances in the actual setup, possibly caused by e.g. backlash, frictional losses, wrongfully estimated aerodynamic loads or incompleteness of the developed model.

Finally, aerodynamic loads are determined through the measurement of reaction forces with a 6-DOF force sensor. The sensor platform is connected to six 1DOF load cells through six wire flexures (each rigid in only the longitudinal direction) in an exactly constraint fashion, enabling it to measure forces and torques in all directions. The six load cell voltage measurements are converted to six forces through the load cell sensitivity matrix. Subsequently these forces are, through a conversion matrix, transposed to the reaction forces in the sensor origin. Through a second conversion matrix these forces are transposed to an arbitrary point on the setup. Measurements are compared to simulation results followed by the distinction of aerodynamic loads. The loads are then transposed to the center of the body and alternatively to the center of the wing. Initial reaction force measurements have indicated good agreement with reaction force simulations for low frequencies, i.e. frequencies up to $1[\mathrm{Hz}]$. For higher frequencies, i.e. above $1[\mathrm{Hz}]$, the measured forces exceed the simulated ones. This is as expected, because the developed model only captures inertia forces and stress resultants whereas the measurements in addition also capture aerodynamic loads. In this way, for wind tunnel experiments to follow, aerodynamic loads can be distinguished by subtracting the measurements from the developed setup with the simulations from the developed model.

Besides studying (aero) dynamics of (Ro) birds, the setup (representing a symmetric half of Robird) can be used for a number of other purposes. It can be used to validate further models developed for (Ro) birds, through system identification. For the purpose of self lift off by Robird, alternative wings (including more DOFs) and variable phase shift during flight can be studied with the test setup. To keep Robird in the air longer, energy saving through adding spring elements (to store and recover energy at appropriate moments) can be investigated using the setup. Finally, an interesting, but quite different, utilization of the setup would be energy generation exploration.

1 Introduction

Robird and its application
Robird is a flying robot bird, manufactured by Clear Flight Solutions (CFS) currently in both a peregrine falcon version and a bald eagle version (both birds of prey), which accomplishes flight through a specific flapping wing mechanism.

This robot bird is indistinguishable from its real life counterpart in both looks and motion to both humans and animals. This is exactly why Robird is such an appealing robot. Due to good imitation of its real life counterpart, Robird can be used in both espionage applications and to scare away birds from places they are undesired at, such as airports and farms.

Bird flapping flight
Taking a single two dimensional (2D) wing section, the flapping wing kinematics of a bird are described by two motions occurring simultaneously, namely plunging and pitching, see Appendix 3.1 and for more detail see [1]. This combined motion is determinative for the wing angle of attack which is crucial for achieving flight.

Due to the complex physics behind flapping wing flight in comparison to fixed wing flight, it is far from fully understood and thus leaves room enough for investigation.

Robird's flapping flight
The Robird flapping wing mechanism is provided with two con rod mechanisms per wing which transform the motor rotational motion into the wing flapping, i.e. plunging and pitching, motion. The latter is obtained by mechanically introducing a phase shift phs into the motion of these two con rod mechanisms.

In such, the flapping wing mechanism on which the flight of Robird is based, requires wing flexibility and causes deformation of the wings, apart from deformation caused by inertial and aerodynamic forces during flapping, and presumably has influences on its flight performance.

Goal
This project is concerned with designing a wind tunnel test setup for the peregrine falcon Robird.

Purpose of the test setup
The designed test setup is intended to provide insight in and understanding of the (aero) dynamics of Robird:

- *Body dynamics*: Data retrieved from system identification and parameter estimation, using the designed test setup, should serve to improve and validate developed models, e.g. for control design purposes and energy efficiency studies.
- *Flapping wing aerodynamics*: Data retrieved from wind tunnel experiments, using the designed test setup, should serve as empirical data and validation data for numerical and analytical studies on flapping flight, see e.g. [1].

Setup requirements

With regard to the purpose of the test setup the following requirements should be met:

1. *Adjustable phase shift* phs: For freedom in experiments, the test setup should allow for an adjustable phase shift phs, typically between 6° and 7°, with an accuracy of $e_{max} = 0.1°$ for flapping frequencies up to $f = 7\ [\mathrm{Hz}]$.
2. *Measurement*: With the test setup it should be possible to measure reaction forces and torques in all directions.
3. *Symmetric half*: The setup should represent a symmetric half of the actual mechanism in order to obtain interpretable aerodynamic force measurements.
4. *Vertical Orientation*: Due to the dimensions of the wind tunnel the setup should be mounted vertically, i.e. under a quarter turn w.r.t. actual mechanism.
5. *Aerodynamic Shield*: The setup should be provided with an aerodynamic shield to reduce flow disturbances.

Early design choices

- For the first requirement two solutions are considered and combined:

    - *Control solution*: Hereby, in contrast to the actual Robird mechanism, there is aimed at establishing the desired phase shift phs actively through the use of two (servo) motors, each predominantly driving a single con rod mechanism. In this way the plant is extended from SISO to TITO.

      This task is interpreted as a set-point error problem for position control. The position references for both motors are ramp signals with gradients corresponding to $f = 7\ [\mathrm{Hz}]$. However there is a delay in-between them, corresponding to the required phase shift phs typically between 6° and 7°. Because both references are controlled individually, the allowed set-point error is set to $\frac{1}{2} \cdot e_{max} = 0.05°$. The chosen control strategy is classic SISO control design combined with decoupling.
    - *Mechanical solution*: Hereby, optionally the desired phase shift phs is fixed passively/mechanically through a frictional disc connection and consequently both con rods are driven by a single motor.

- With regard to requirement two, a straightforward solution is followed, i.e. a 6-DOF (degrees of freedom) force sensor is mounted at the base of the setup, enabling measurement of reaction forces and torques in all directions.
- The remaining requirements are incorporated in the mechanical design quite straightforwardly.

Approach

For the purpose of controller design, in section 2 first a model of the proposed TITO setup has been developed in Spacar using a finite element formulation. Additionally, with the aim at applying position control design, the model is linearized and simplified. Next, in section 0 controller and mechanical design are conducted and appropriate equipment is selected. For control design a one parameter approach is followed using classic SISO control techniques combined with plant decoupling and for the mechanical solution, a frictional disc connection is designed for obtaining the desired phase shift phs. After ordering and assembly of the setup, first system identification and parameter estimation are conducted in section 4. Thereafter, using the identified plant, in section 5 the developed model is validated and the controller is redesigned. This is followed by controller implementation and tweaking in section 6. In section 7 force measurements experiments have been conducted and finally conclusions and recommendations are given. This process has been executed according to the schedule included in Appendix 10.

2 Model development

First, a model of the proposed TITO setup has been developed in Spacar using a finite element formulation. With the aim at applying position control design, using classic SISO control techniques combined with plant decoupling, the model is linearized and simplified. Referring to the latter, aiming at performance, only the low frequency region is captured for control design.

2.1 Elaborate model development

In this section an elaborate non-linear model, also accounting for the coupling of the (servo) motors through the wing stiffness, is developed in Spacar. The developed model contains 2 DOFs accounting for the rotation applied by the motors (see Figure 1).

2.1.1 Kinematic analysis

First all nodal and deformation coordinates of the system are identified. The nodal coordinates x are partitioned into support coordinates $x^{(\mathrm{o})}$, independent nodal coordinates $x^{(m)}$ and calculable nodal coordinates $x^{(c)}$, i.e.:

1 $$x = \begin{bmatrix} [x^{(\mathrm{o})}] \\ [x^{(c)}] \\ [x^{(m)}] \end{bmatrix}$$

The deformation coordinates are in turn partitioned into zero deformation coordinates $\varepsilon^{(\mathrm{o})} = D(x)^{(\mathrm{o})}$, independent deformation coordinates $\varepsilon^{(m)} = D(x)^{(m)}$ and redundant deformation coordinates $\varepsilon^{(c)} = D(x)^{(c)}$, i.e.:

2 $$\varepsilon = \begin{bmatrix} [\varepsilon^{(\mathrm{o})}] \\ [\varepsilon^{(m)}] \\ [\varepsilon^{(c)}] \end{bmatrix} = \begin{bmatrix} [D(x)^{(\mathrm{o})}] \\ [D(x)^{(m)}] \\ [D(x)^{(c)}] \end{bmatrix}$$

Then there is checked whether the system is kinematically determinate, simply by evaluating if the number of unknown variables (number of $x^{(c)}$) equals the number of useful equations (number of $D(x)^{(\mathrm{o})}$ and $D(x)^{(m)}$).

The number of degrees of freedom within the system equals the number of x minus the number of $x^{(\mathrm{o})}$ minus the number $\varepsilon^{(\mathrm{o})}$. For exact restriction, this should be equal to the number of $x^{(m)}$ and $\varepsilon^{(m)}$.

Next, the configuration and deformation state and their derivatives of the mechanism are described in terms of the degrees of freedom which are grouped as follows:

3 $$q = \begin{bmatrix} [x^{(m)}] \\ [\varepsilon^{(m)}] \end{bmatrix}$$

The nodal and deformation coordinates are then described in terms of q as follows:

4 $$x = F(q)$$

5 $$\begin{aligned} &\varepsilon = E(q) \Leftrightarrow \\ &D(x) = E(q) \Leftrightarrow \\ &E(q) = D\big(F(q)\big) \end{aligned}$$

These equations, i.e. the zeroth order geometric transfer functions $F(q)$ and $E(q)$, are highly nonlinear and the position of the mechanism is solved numerically by use of a Newton-Raphson iteration method. Although the position may not be solved analytically, the velocity and acceleration may be:

After time derivation of Eq.4 and Eq.5, the following applies for the velocities:

6
$$\begin{aligned}\dot{x} &= F_{,q}\dot{q}\\ \dot{\varepsilon} &= E_{,q}\dot{q}\end{aligned}$$

After time derivation of Eq.6, the following applies for the accelerations:

7
$$\begin{aligned}\ddot{x} &= F_{,q}\ddot{q} + \left(F_{,qq}\dot{q}\right)\dot{q}\\ \dot{\varepsilon} &= E_{,q}\ddot{q} + \left(E_{,qq}\dot{q}\right)\dot{q}\end{aligned}$$

Hereby $F_{,q}$ and $E_{,q}$ are the first order geometric transfer functions and $F_{,qq}$ and $E_{,qq}$ are de second order geometric transfer functions. In contrast to the zeroth order geometric transfer functions $F(q)$ and $E(q)$, these can be solved analytically as will be illustrated in the following.

Differentiating Eq. 5 with respect to q yields:

8
$$E_{,q} = D_{,x}F_{,q}$$

Rewriting this equation by using the partitioning as introduced in equations1,2 and 3 yields:

9
$$\begin{bmatrix} E_{,q}^{(o)} \\ E_{,q}^{(m)} \\ E_{,q}^{(c)} \end{bmatrix} = \begin{bmatrix} D_{,x^{(o)}}^{(o)} & D_{,x^{(c)}}^{(o)} & D_{,x^{(m)}}^{(o)} \\ D_{,x^{(o)}}^{(m)} & D_{,x^{(c)}}^{(m)} & D_{,x^{(m)}}^{(m)} \\ D_{,x^{(o)}}^{(c)} & D_{,x^{(c)}}^{(c)} & D_{,x^{(m)}}^{(c)} \end{bmatrix} \begin{bmatrix} F_{,q}^{(o)} \\ F_{,q}^{(c)} \\ F_{,q}^{(m)} \end{bmatrix}$$

Then for the first order geometric transfer function applies:

10
$$\begin{aligned}
F_{,q}^{(o)} &= \begin{bmatrix} \frac{\delta x^{(o)}}{\delta x^{(m)}} & \frac{\delta x^{(o)}}{\delta \varepsilon^{(m)}} \end{bmatrix}\\
F_{,q}^{(m)} &= \begin{bmatrix} \frac{\delta x^{(m)}}{\delta x^{(m)}} & \frac{\delta x^{(m)}}{\delta \varepsilon^{(m)}} \end{bmatrix}\\
E_{,q}^{(o)} &= \begin{bmatrix} \frac{\delta \varepsilon^{(o)}}{\delta x^{(m)}} & \frac{\delta \varepsilon^{(o)}}{\delta \varepsilon^{(m)}} \end{bmatrix}\\
E_{,q}^{(m)} &= \begin{bmatrix} \frac{\delta \varepsilon^{(m)}}{\delta x^{(m)}} & \frac{\delta \varepsilon^{(m)}}{\delta \varepsilon^{(m)}} \end{bmatrix}\\
F_{,q}^{(c)} &= \left(\mathrm{D}^{(c)}\right)^{-1} \left(\begin{bmatrix} E_{,q}^{(o)} \\ E_{,q}^{(m)} \end{bmatrix} - \begin{bmatrix} D_{,x^{(m)}}^{(o)} \\ D_{,x^{(m)}}^{(m)} \end{bmatrix} F_{,q}^{(m)} \right)\\
E_{,q}^{(c)} &= D_{,x^{(c)}}^{(c)} F_{,q}^{(c)} + D_{,x^{(m)}}^{(c)} F_{,q}^{(m)}
\end{aligned}$$

With:

$$\mathrm{D}^{(c)} = \begin{bmatrix} D_{,x^{(c)}}^{(o)} \\ D_{,x^{(c)}}^{(m)} \end{bmatrix}$$

Differentiating Eq. 8 with respect to q yields:

$$E_{,qq} = (D_{,xx}F_{,q})F_{,q} + D_{,x}F_{,qq} \tag{11}$$

Rewriting this equation by using the partitioning as introduced in equations 1,2 and 3 yields:

$$\begin{bmatrix} E_{,qq}^{(o)} \\ E_{,qq}^{(m)} \\ E_{,qq}^{(c)} \end{bmatrix} = \begin{bmatrix} \left(D_{,xx}^{(o)}F_{,q}\right)F_{,q} \\ \left(D_{,xx}^{(m)}F_{,q}\right)F_{,q} \\ \left(D_{,xx}^{(c)}F_{,q}\right)F_{,q} \end{bmatrix} + \begin{bmatrix} D_{,x^{(o)}}^{(o)} & D_{,x^{(c)}}^{(o)} & D_{,x^{(m)}}^{(o)} \\ D_{,x^{(o)}}^{(m)} & D_{,x^{(c)}}^{(m)} & D_{,x^{(m)}}^{(m)} \\ D_{,x^{(o)}}^{(c)} & D_{,x^{(c)}}^{(c)} & D_{,x^{(m)}}^{(c)} \end{bmatrix} \begin{bmatrix} F_{,qq}^{(o)} \\ F_{,qq}^{(c)} \\ F_{,qq}^{(m)} \end{bmatrix} \tag{12}$$

Then for the second order geometric transfer function applies:

$$\begin{aligned} F_{,qq}^{(o)} &= \begin{bmatrix} \frac{\delta F_{,q}^{(o)}}{\delta x^{(m)}} & \frac{\delta F_{,q}^{(o)}}{\delta \varepsilon^{(m)}} \end{bmatrix} \\ F_{,qq}^{(m)} &= \begin{bmatrix} \frac{\delta F_{,q}^{(m)}}{\delta x^{(m)}} & \frac{\delta F_{,q}^{(m)}}{\delta \varepsilon^{(m)}} \end{bmatrix} \\ E_{,qq}^{(o)} &= \begin{bmatrix} \frac{\delta E_{,q}^{(o)}}{\delta x^{(m)}} & \frac{\delta E_{,q}^{(o)}}{\delta \varepsilon^{(m)}} \end{bmatrix} \\ E_{,qq}^{(m)} &= \begin{bmatrix} \frac{\delta E_{,q}^{(m)}}{\delta x^{(m)}} & \frac{\delta E_{,q}^{(m)}}{\delta \varepsilon^{(m)}} \end{bmatrix} \\ F_{,qq}^{(c)} &= -\left(\mathrm{D}^{(c)}\right)^{-1} \begin{bmatrix} (D_{,xx}^{(o)}F_{,q})F_{,q} \\ \left(D_{,xx}^{(m)}F_{,q}\right)F_{,q} \end{bmatrix} \\ E_{,qq}^{(c)} &= (D_{,xx}^{(c)}F_{,q})F_{,q} + D_{,x^{(m)}}^{(c)}F_{,qq}^{(c)} \end{aligned} \tag{13}$$

Now that the first and second order transfer functions are known, the position can be solved numerically by means of the Newton-Raphson method, hereby taking into account the first and second order terms of the Taylor series expansion of equation 4 and 5:

$$\begin{aligned} x_{(1)} &= x_0 + \left(F_{,q}\right)_0 \Delta q + \tfrac{1}{2}\left(\left(F_{,qq}\right)_0 \Delta q\right) \Delta q \\ \varepsilon_{(1)} &= \varepsilon_0 + \left(E_{,q}\right)_0 \Delta q + \tfrac{1}{2}\left(\left(E_{,qq}\right)_0 \Delta q\right) \Delta q \end{aligned} \tag{14}$$

For more detail on this see [2] and [3].

2.1.2 Dynamic analysis

The dynamics of the system is described by a relatively elaborate equation of motion, which can be derived by means of the principle of virtual work and d'Alembert's principle (again, for more detail see [2] and [3]):

$$\bar{M}\ddot{q} = F_{,q}^{T}\left[f - h - M\left(F_{,qq}\dot{q}\right)\dot{q}\right] - E_{,q}^{T}\sigma \tag{15}$$

Where: $\bar{M} = F_{,q}^{T} M F_{,q}$ = Reduced mass matrix
M = Mass matrix
f = Nodal forces
h = Convective term of the inertia property which is a function of the position coordinates and quadratic in the velocities
σ = Stress resultants calculated from the linear constitutive Kelvin-Voigt equations: $\sigma = S\varepsilon + S_d\dot{\varepsilon}$
S = Stiffness matrix
S_d = Damping matrix

2.1.3 External forces and reaction forces

Prior to calculating the stress resultants and reaction forces, the motion of the multi-body system must be known already. The external forces (including the reaction forces) can be determined as follows (this is explained very well in [2] and [3]):

16 $$f = D_{,x}^{T}\sigma + h + M\ddot{x}$$

In Appendix 1.1 an example of the kinematic and dynamic analysis as conducted by Spacar is illustrated for a simplified 2D version of the setup mechanism.

2.1.4 Kinematic determinability and exact restriction for the model of the setup mechanism

In the following, kinematic determinability and exact restriction of the developed model for the setup mechanism (see Figure 1) are illustrated.

As discussed in section 2.1.1, the nodal coordinates x are partitioned into support/ absolute constraint coordinates $x^{(\mathrm{o})}$, independent nodal coordinates $x^{(m)}$ and calculable nodal coordinates $x^{(c)}$. With their respective numbers $N_{x^{(o)}}$, $N_{x^{(m)}}$ and $N_{x^{(c)}}$ and their sum N_x. The deformation coordinates are partitioned into zero deformation/ relative constraint coordinates $\varepsilon^{(\mathrm{o})} = D(x)^{(\mathrm{o})}$, independent deformation coordinates $\varepsilon^{(m)} = D(x)^{(m)}$ and redundant deformation coordinates $\varepsilon^{(c)} = D(x)^{(c)}$. With their respective numbers $N_{\varepsilon^{(o)}}$, $N_{x^{(m)}}$ and $N_{\varepsilon^{(c)}}$, and their sum N_ε.

Kinematic determinability applies if the number of unknown variables matches the number of useful equations, i.e.:

17 $$N_{x^{(c)}} = N_{\varepsilon^{(o)}} + N_{\varepsilon^{(m)}}$$

Exact restriction applies when the number of user defined DOFs, $NudDOF$, equals the number of resulting DOFs, $NDOF$, i.e.:

18 $$N_{x^{(m)}} + N_{\varepsilon^{(m)}} = N_x - N_{x^{(o)}} - N_{\varepsilon^{(o)}}$$

With:

$$N_{x^{(m)}} + N_{\varepsilon^{(m)}} = NudDOF$$
$$N_x - N_{x^{(o)}} - N_{\varepsilon^{(o)}} = NDOF$$

The following values apply for the numbers of the partitioned coordinates of this system:

$N_x = 120$, determined from the sum of:

- (16×3) translational coordinates, represented by the (16) blue circles in Figure 1, each representing 3 translational coordinates, x, y and z describing a node position
- (24×3) rotational coordinates, represented by the (24) blue dots in Figure 1, each representing 3 Euler parameters, λ_1, λ_2 and λ_3 describing a node orientation

$N_{x^{(o)}} = 12$, i.e. 12 absolute constraints, represented by the black arrows in Figure 1.

$N_{\varepsilon^{(o)}} = 106$, is determined from the sum of:

- (17×6), i.e. 17 fully rigid beams, represented by the (17) blue lines in Figure 1, each restricted in elongation (1 DOF), torsion(1 DOF) and bending (4 DOFs)
- (2×2), i.e. 2 partially rigid hinges (restricted in orthogonal bending, 2 DOFs; but free in relative rotation 1 DOF), represented by the (2) green circles in Figure 1

$N_{\varepsilon^{(m)}} = 2$, i.e. two relative rotations have been chosen as DOFs, see the red arrows in Figure 1.
$N_{x^{(m)}} = 0$, i.e. zero nodal coordinates are chosen as DOFs.
$N_{x^{(c)}} = \ 108$, i.e. $N_{x^{(c)}} = N_x - N_{x^{(o)}} - N_{x^{(m)}}$

Applying the above determined values to equations 17 and 18 proves the system to be kinematically determinable as well as exactly constraint. I.e., 108 unknown variables (calculable coordinates $N_{x^{(c)}}$) are solved by 108 useful equations ($N_{\varepsilon^{(o)}}$ and $N_{\varepsilon^{(m)}}$) and the 2 user defined DOFs ($NudDOF$) correspond to the 2 resulting degrees of freedom ($NDOF$).

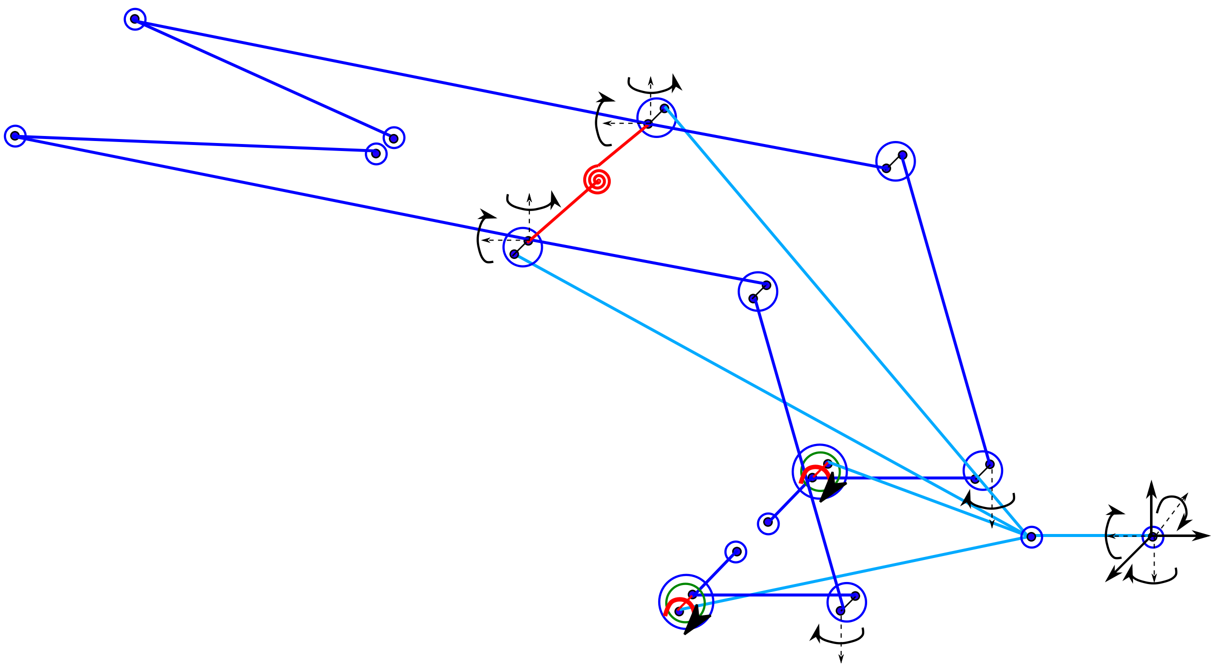

Figure 1 More elaborate model development in Spacar: Wing stiffness is modeled through a torsional spring (see the red colored element)

2.2 Simplified model illustrating coupling

In the following, the elaborate model is somewhat simplified in order to explain the coupling present in the system. The system is reduced to two inertias J_1 and J_2 (each representing half the mechanism) connected to each other by a (rotational) spring k and a (rotational) damper d (representing the wing) (see Figure 2).

Hence the momentum equation reduces to:

19

$$\begin{aligned} J_1\ddot{\theta}_1 &= T_1 - d\big(\dot{\theta}_1 - \dot{\theta}_2\big) - k(\theta_1 - \theta_2) \\ J_2\ddot{\theta}_2 &= T_2 + d\big(\dot{\theta}_1 - \dot{\theta}_2\big) + k(\theta_1 - \theta_2) \end{aligned}$$

Taking the Laplace transform, this can be rewritten into the following form:

20

$$\begin{aligned}(J_1 s^2 + ds + k)\theta_1 - (ds - k)\theta_2 \quad &= T_1 \\ -(ds - k)\theta_2 \quad + (J_2 s^2 + ds + k)\theta_1 \quad &= T_2\end{aligned}$$

In matrix form, this yields:

21 $$A \begin{bmatrix}\theta_1 \\ \theta_2\end{bmatrix} = \begin{bmatrix}T_1 \\ T_2\end{bmatrix}$$

With:

22 $$A = \begin{bmatrix}a_{11} & a_{12} \\ a_{21} & a_{22}\end{bmatrix}$$

Whereby the following applies for the entries of A:

23

$$\begin{aligned}a_{11} &= \ (J_1 s^2 + ds + k) \\ a_{12} &= -(ds - k) \\ a_{21} &= -(ds - k) \\ a_{22} &= (J_2 s^2 + ds + k)\end{aligned}$$

For the transfer function G then applies:

24 $$\begin{bmatrix}\theta_1 \\ \theta_2\end{bmatrix} = G \begin{bmatrix}T_1 \\ T_2\end{bmatrix}$$

From eqs. 21, 22 and 23 follows for G:

25 $$G = \begin{bmatrix}G_{11} & G_{12} \\ G_{21} & G_{22}\end{bmatrix} = A^{-1} = \begin{bmatrix}a_{11} & a_{12} \\ a_{21} & a_{22}\end{bmatrix}^{-1} = \frac{1}{\det(A)} \begin{bmatrix}a_{22} & -a_{12} \\ -a_{21} & a_{11}\end{bmatrix}$$
$$= \frac{1}{(a_{11}a_{22} - a_{12}a_{21})} \begin{bmatrix}a_{22} & -a_{12} \\ -a_{21} & a_{11}\end{bmatrix}$$

Substituting eq. 23 into eq.25 and using a preferred notation as described in [4], yields the following for the transfer functions and allows for obtaining physical interpretations of the occurring resonances:

26 $$G_{11} = \frac{\theta_1}{T_1} = \frac{K\left(\frac{s^2}{\omega_{AR,1}^2} + \frac{2\zeta_{AR,1} s}{\omega_{AR,1}} + 1\right)}{s^2\left(\frac{s^2}{\omega_R^2} + \frac{2\zeta_R s}{\omega_R} + 1\right)}$$

27 $$G_{12} = \frac{\theta_1}{T_2} = \frac{K(\tau s + 1)}{s^2\left(\frac{s^2}{\omega_R^2} + \frac{2\zeta_R s}{\omega_R} + 1\right)}$$

28 $$G_{21} = \frac{\theta_2}{T_1} = \frac{K(\tau s + 1)}{s^2\left(\frac{s^2}{\omega_R^2} + \frac{2\zeta_R s}{\omega_R} + 1\right)}$$

29 $$G_{22} = \frac{\theta_2}{T_2} = \frac{K\left(\frac{s^2}{\omega_{AR,2}^2} + \frac{2\zeta_{AR,2}s}{\omega_{AR,2}} + 1\right)}{s^2\left(\frac{s^2}{\omega_R^2} + \frac{2\zeta_R s}{\omega_R} + 1\right)}$$

With:

30 $$K = \frac{1}{J_1 + J_2}$$

31 $$\tau = \frac{d}{k}$$

32 $$\omega_R = \sqrt{\frac{k(J_1 + J_2)}{J_1 J_2}}$$

33 $$\zeta_R = \frac{d}{2\sqrt{\frac{kJ_1J_2}{J_1 + J_2}}}$$

34 $$\omega_{AR,1} = \sqrt{\frac{k}{J_2}}$$

35 $$\zeta_{AR,1} = \frac{d}{2\sqrt{kJ_2}}$$

36 $$\omega_{AR,2} = \sqrt{\frac{k}{J_1}}$$

37 $$\zeta_{AR,2} = \frac{d}{2\sqrt{kJ_1}}$$

Hereby ω_R and ζ_R represent the resonance/natural frequency and damping of the complete system. $\omega_{AR,1}$ and $\zeta_{AR,1}$ represent the anti-resonance and damping equivalent to the natural frequency of inertia J_2 connected to the fixed world through the compliance k and damping d. The equivalent applies for $\omega_{AR,2}$ and $\zeta_{AR,2}$.

In this case, due to symmetry of the mechanism, $J_1 = J_2$. Applying this to eqs.32, 34 and 36 yields:

38 $\omega_{AR,1} = \omega_{AR,2} = \frac{1}{2}\sqrt{2}\omega_R$, for: $J_1 = J_2$, see Figure 4 and Figure 5

Decoupling

Provided there is enough knowledge of the system G (through either model development or system identification), one way of decoupling is illustrated in the following. As the goal of decoupling is to obtain a diagonal matrix, the decoupling matrix should bring about the following effect:

39 $$GD = \begin{bmatrix} G_{11} & 0 \\ 0 & G_{22} \end{bmatrix}$$

Hence, this would result in a decoupling matrix defined as follows (also see [5]):

40 $$D = G^{-1}\begin{bmatrix} G_{11} & 0 \\ 0 & G_{22} \end{bmatrix}$$

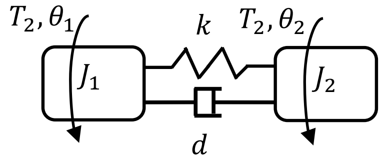

Figure 2 Simplified model illustrating mechanical compliant coupling

2.3 Simplified model for controller design

Previous to controller design a sufficient model should be developed. Because performance analysis is a low frequency subject it is acceptable to only model low frequent behavior when analyzing performance (and when designing a controller for performance improvement). The following assumptions are made for obtaining a sufficient model [6]:

- First only 1 DOF is considered (see Figure 3)
- (Half) The wing mechanism is assumed to be a simple rigid equivalent mass (m) to be moved by the actuator force
- The stiffness in the actuated direction is considered to correspond to the low frequency resonance $k = m \cdot \left(\omega_{R_{low}}^2\right) = \frac{m \cdot g}{L}$; also see Appendix 6
- The back-emf in the actuator (motor and gearbox) is modeled as damping d:

41 $$d = \frac{(k_m \cdot i \cdot \eta_G)^2}{R}$$

With:

k_m = motor torque constant
R = coil resistance
i = gear reduction
η_G = gear efficiency
g = gravitational acceleration
L = half length of the wing

- The actuator (motor and gearbox) force is modeled as an applied force:

42 $$F = \frac{U}{R} \cdot k_m \cdot i \cdot \eta_G = I \cdot k_m \cdot i \cdot \eta_G$$

With:

U = supplied voltage
I = supplied current

To this end, the following is obtained for the equation of motion:

43 $$m\ddot{x} = I \cdot (k_m \cdot i \cdot \eta_G) - kx - d\dot{x}$$

Plant transfer function
Hence with current control ($d = 0$; see [6]) the plant model becomes:

44 $$G = \frac{x(s)}{I(s)} = \frac{\frac{(k_m \cdot i \cdot \eta_G)}{m}}{s^2 + \frac{d}{m}s + \frac{k}{m}} = \frac{\frac{1}{m_{eq}}}{s^2 + \frac{d}{m}s + \frac{k}{m}}$$

With:

45 $$m_{eq} = \frac{m}{k_m \cdot i \cdot \eta_G}$$

In principle the two actuation directions of the wing mechanism are coupled through the wing stiffness. However at first it is assumed that the system is decoupled, hence it could be easily extended to a 2 DOF i.e. two input two output system as follows:

46 $$\begin{bmatrix} x_1 \\ x_2 \end{bmatrix} = \frac{\frac{1}{m_{eq}}}{s^2 + \frac{d}{m}s + \frac{k}{m}} \begin{bmatrix} 1 & 0 \\ 0 & 1 \end{bmatrix} \begin{bmatrix} I_1 \\ I_2 \end{bmatrix}$$

Model parameters
It is worth mentioning that in coming to the values of some of the parameters usage has been made of the more elaborate model developed in which is subject of section 2.1. The values applying to the parameters are given in Table 1.

Bode plot
Supplying all parameters to equation 44 yields the bode plot for 1 DOF of the system as depicted in Figure 5.

Parameter		Symbol	Value	Dimension	Reference
Mass (for 1 DOF)		m	0.0441	[kg]	Appendix 1.2
Equivalent mass		m_{eq}	0.0026	$[{s^2}/{rad^2}]$	
Wing stiffness	Torsional stiffness	k_t	3.35	$[{Nm}/{rad}]$	Appendix 1.3
	Longitudinal stiffness	k	1.6	$[{N}/{m}]$	
Motor parameters	Torque constant	k_m	0.0205	$[{Nm}/{A}]$	Chapter 3.4
	Coil resistance	R	1.39	$[\Omega]$	
Gearbox parameters	Gear reduction	i	18	[ ]	
	Gear efficiency	η_G	0.75	[ ]	

Table 1 Model parameters

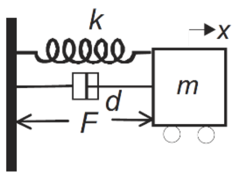

Figure 3 General nominal model of motion system used for performance analyses/synthesis [6]

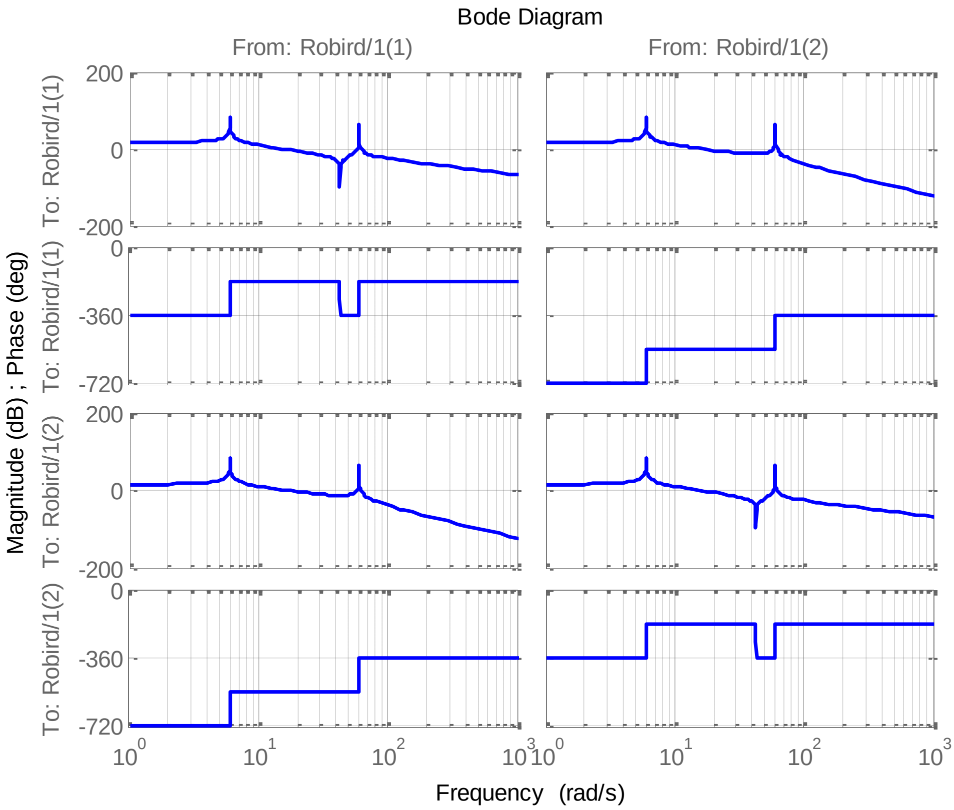

Figure 4 Bode plot for coupled model of Robird

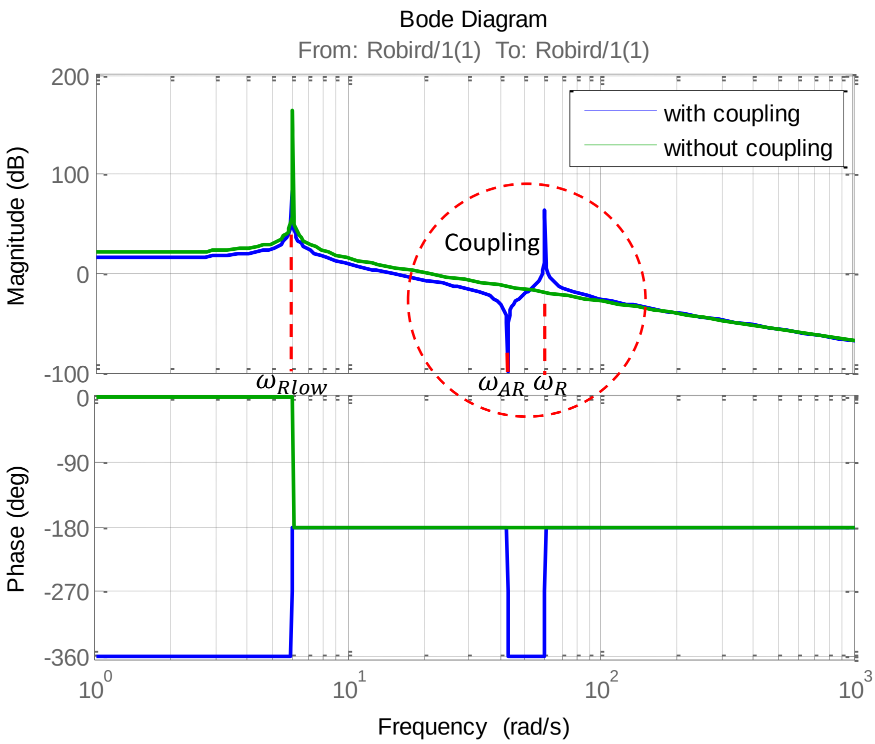

Figure 5 Green: Bode plot for 1 DOF of the simplified model of Robird; Blue: Bode plot for 1 DOF of the coupled model of Robird

3 Controller and mechanical design

3.1 Control Solution

In this section the control solution is considered whereby the aim is establishing the desired phase shift phs through the use of two (servo) motors. This will require sufficient controller design. The strategy that is followed here is decoupling combined with the application of classic SISO design techniques. The controller is designed based on a simplified model of the system and then tested on the more elaborate model after decoupling. Tests are done first on a linearized model and finally on the non-linear model.

3.1.1 (PID) Controller design

Now, a conceptual PID controller is designed based on the following [6]:

- Proportional control: to set the required cross-over frequency (or bandwidth)
- Integral control: to obtain a small steady state error; i.e. to keep the mass in position when positioning (compensating for the spring force)
- Derivative control: to provide enough phase-margin at cross-over frequency

PID controller
To this end the following conceptual PID controller is obtained [6]:

47 $$K = \frac{k_p(s\tau_z+1)(s\tau_i+1)}{s\tau_i(s\tau_p+1)}$$

Its corresponding frequency plot is shown in Figure 6. As the plot also illustrates the following is indicated by the parameters [6]:

- k_p = Proportional gain
- $\frac{1}{\tau_z}$ = Corner frequency where derivative action is started
- $\frac{1}{\tau_p}$ = Corner frequency where derivative action stops
- $\frac{1}{\tau_i}$ = Corner frequency where integral action stops

Requirements [6]

- The Phase-lag of the integral action should not interfere with phase-lead of the derivative action; i.e. τ_i^{-1} should be lower than τ_z^{-1}

- The phase lead of the PID should be used as efficient as possible; i.e. the PID controller parameters are chosen in such a way that the desired cross-over frequency equals the frequency where maximum phase-lead occurs.

PID controller parameters
To this end the PID controller parameters could be expressed in the cross-over frequency [6]:

48

$$\tau_z = \frac{\sqrt{\frac{1}{\alpha}}}{\omega_c}$$
$$\tau_i = \beta\tau_z$$

$$\tau_p = \frac{1}{\omega_c\sqrt{\frac{1}{\alpha}}}$$
$$k_p = \frac{m_{eq}{\omega_c}^2}{\sqrt{\frac{1}{\alpha}}}$$

α (the amount of phase-lead) is between 0.1 and 0.3 and $\beta > 1$. In this case the following is chosen:

49

$$\alpha = 0.2$$
$$\beta = 2$$

Performance specifications (desired cross-over frequency)

In the previous section the PID controller parameters have been expressed in terms of ω_c. It is the focus of the following to determine ω_c. The value of ω_c is chosen in such a way that the set-point error (for the constant-velocity part of the reference; this will be explained later) is below $e = \frac{1}{2} \cdot e_{max} = 0.05° = 8.7 \cdot 10^{-4}[\text{rad}]$. As $e = S \cdot r$, the sensitivity function S of the system will play an important role. Also the nature of the reference signal r is of great importance.

Bode plot of the PID controller and Block diagram

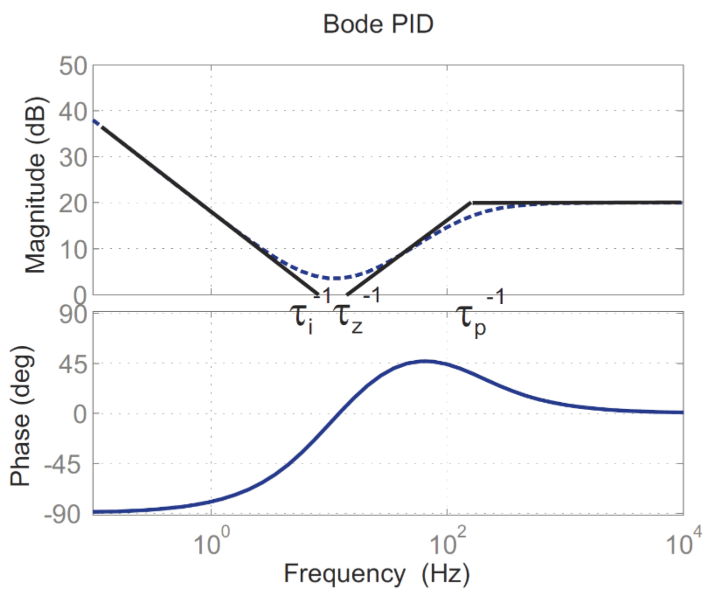

Figure 6 - Bode plot of the conceptual PID controller [6]

The system with feedback has the following configuration:

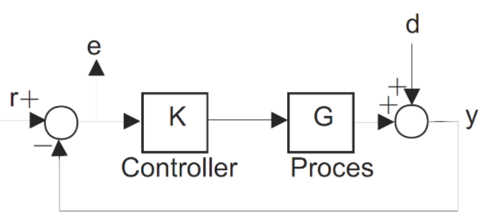

Figure 7 Block diagram of system [6]

Sensitivity function
From the block diagram the following is obtained for the sensitivity function:

50 $$S = \frac{e}{r} = (I + GK)^{-1}$$

Low frequent sensitivity function
Applying Eqs. 44, 47 and 48 to Eq. 50 and only considering relevant low frequent behavior (i.e. admissibly disregarding some high order terms; see [6]), the following sensitivity function is obtained [6]:

51 $$S = \frac{s^3 + \left(\frac{d}{m}\right)s^2 + (\omega_n^2)s}{\left(\frac{\alpha}{\beta}\right)(\omega_c^3)}$$

Desired cross-over and servo-error function
From S (see eq.50 and eq.51) it follows that the desired ω_c is dependent on the reference velocity, acceleration and jerk; as is the servo error:

52 $$\omega_c = \left(\frac{R\beta k\dot{r} + b(k_m \cdot i \cdot \eta_G)^2\ddot{r} + R\beta m\dddot{r}}{R\alpha e m}\right)^{\frac{1}{3}}$$

53 $$e = \frac{\beta\left(\frac{k\dot{r}}{m} + \frac{(k_m \cdot i \cdot \eta_G)^2\ddot{r}}{Rm} + \dddot{r}\right)}{\alpha\omega_c^3}$$

Equation for reference
The following combination of a 3rd order polynomial and linear function, shaping a ramp signal, is taken as the reference signal:

Eq. 54:

$$r = \frac{16h_m t^3}{3t_m^3},\ 0 \le t \le \left(\frac{t_m}{4}\right)$$

$$r = -\frac{32h_m\left(\frac{t^3}{6} - \frac{t^2 t_m}{4} + \frac{t t_m^2}{16} - \frac{t_m^3}{192}\right)}{t_m^3},\ \left(\frac{t_m}{4}\right) < t \le \left(\frac{t_m}{2}\right)$$

$$r = \left(\frac{2h_m}{t_m}\right)t + \left(-\frac{h_m}{2}\right), \left(\frac{t_m}{2}\right) < t \le \left(\frac{t_m}{2} + \Delta t\right)$$

Reference signal parameters

$t_m = 0.1[\mathrm{s}]$
$h_m = \frac{\omega_0 t_m}{2}$
With $\omega_0 = 44\ [\frac{\mathrm{rad}}{\mathrm{s}}]$

Plots
Reference signal
From top to bottom: position, velocity, acceleration and jerk:

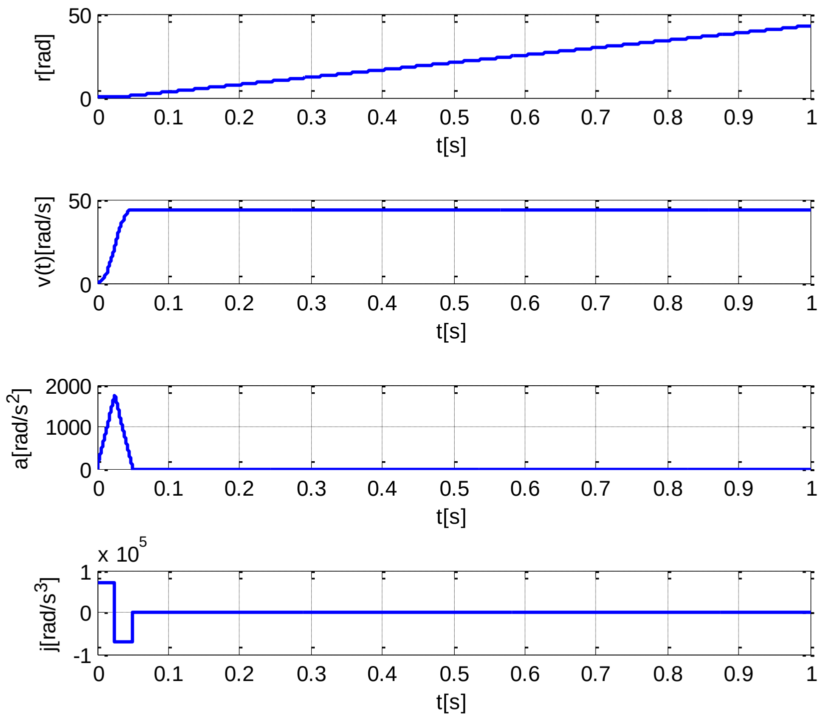

Figure 8 Reference signal

Servo-error

Servo error:

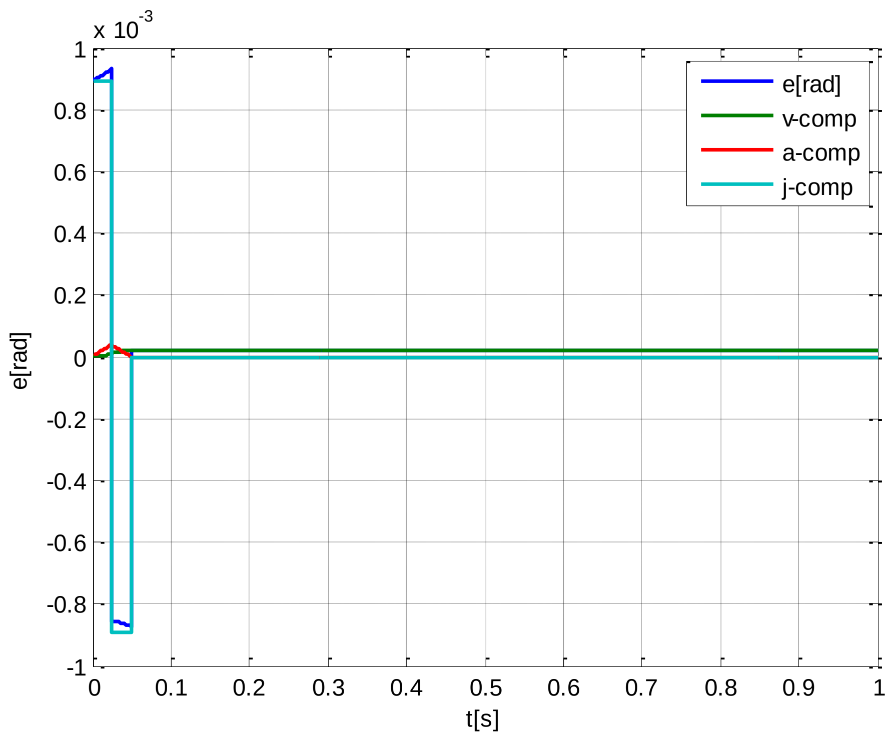

Figure 9: Servo error

The goal set here, is to obtain the performance target as soon as the reference signal reaches the constant velocity part. Hence, the region of interest is the section before the signal changes into the constant velocity part: $\left(\frac{t_m}{4}\right) < t \leq \left(\frac{t_m}{2}\right)$, i.e.: $0.025[\mathrm{s}] < t \leq 0.050$ [s]. Hence, the second line of equation Eq. 54 is substituted into eqs. 52 to obtain the desired cross-over frequency:

$$\omega_c = 126[\mathrm{Hz}] = 793[\mathrm{rad/s}]$$

3.1.2 Controller application

In determining the required cross-over frequency, the PID controller has in fact been designed as all its parameters were expressed in ω_c (see equations 47 and 48). In the design of the PID controller, usage has been made of the series form:

47 $$K = \frac{k_p(s\tau_z+1)(s\tau_i+1)}{s\tau_i(s\tau_p+1)}$$

This can be rewritten as follows:

55 $$K = \frac{K_1 s^2 + K_2 s + K_3}{s(\tau s+1)}$$

With:

$$K_1 = k_p \tau_z$$
$$K_2 = \frac{k_p(\tau_z+\tau_i)}{\tau_i}$$
$$K_3 = \frac{k_p}{\tau_i}$$
$$\tau = \tau_p$$

Then the series form can be converted to the more usual parallel form of an industrial PID controller (as discusses in [7]) as follows:

56 $$K = K_p + \frac{K_i}{s} + \frac{K_d s}{s\tau+1}$$

With:

$$K_p = K_2 - K_3 \tau$$
$$K_i = K_3$$
$$K_d = K_1 - K_2 \tau + K_3 \tau^2$$

With the chosen motor and gearbox the following is obtained for the PID controller parameters:

$$K_p = 1461$$
$$K_i = 2.1559 \cdot 10^5$$
$$K_d = 1.8192$$

Prior to applying the PID controller to the system, the system is first linearized, decoupled and decoupling matrices are formulated. The PID controller is adjusted with these matrices and thereafter it is applied to the system.

Linearization

The system is linearized around the working point where both motors have an angular velocity $\omega_0 = 7\,[\mathrm{Hz}] = 44\,[\frac{\mathrm{rad}}{\mathrm{s}}]$ with a desired phase shift $phs = 7° = \ 0.1222[\mathrm{rad}]$ in-between. In Figure 10, the linearized and simplified plant are exhibited.

Decoupling

Due to the wing stiffness, there is quite some coupling in the system. Because applying a PID controller is a SISO control approach, the system first needs to be decoupled (diagonalized). The diagonal PID controller is assisted with input and output matrices such that it experiences the plant as a decoupled one. This is done by the Owens method (see [8]). In applying the Owens method interaction between the modes is removed for a specified frequency regime. Here the chosen regime has been: $0 \leq \ \omega \geq \ 2\omega_c$. This has been done using the wadyadicd.m script and the decoupling has been successful (see Figure 11).The PID controller is adjusted with the decoupling matrices and has a bode plot as illustrated in Figure 12.

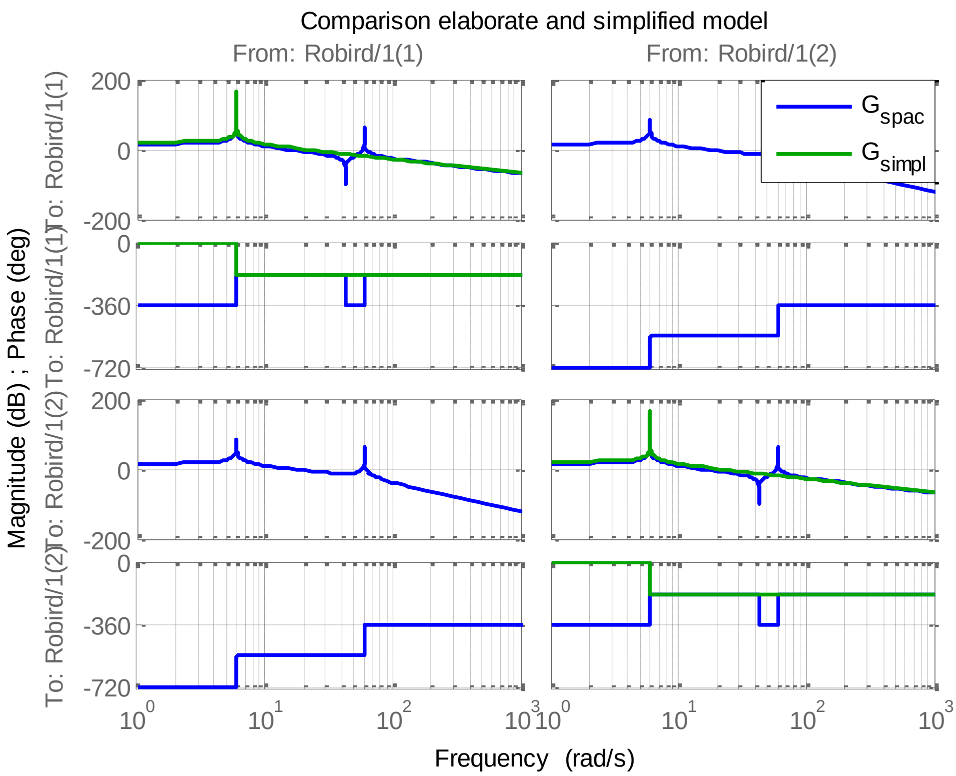

Figure 10 Comparison elaborate and simplified model

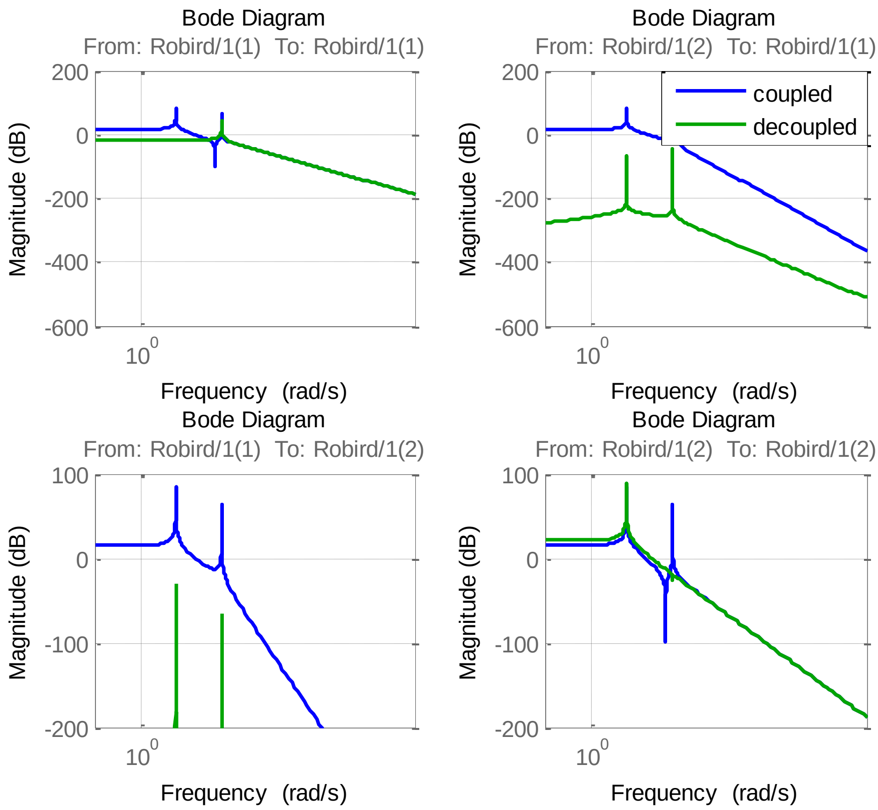

Figure 11 Decoupling by means of the Owens method

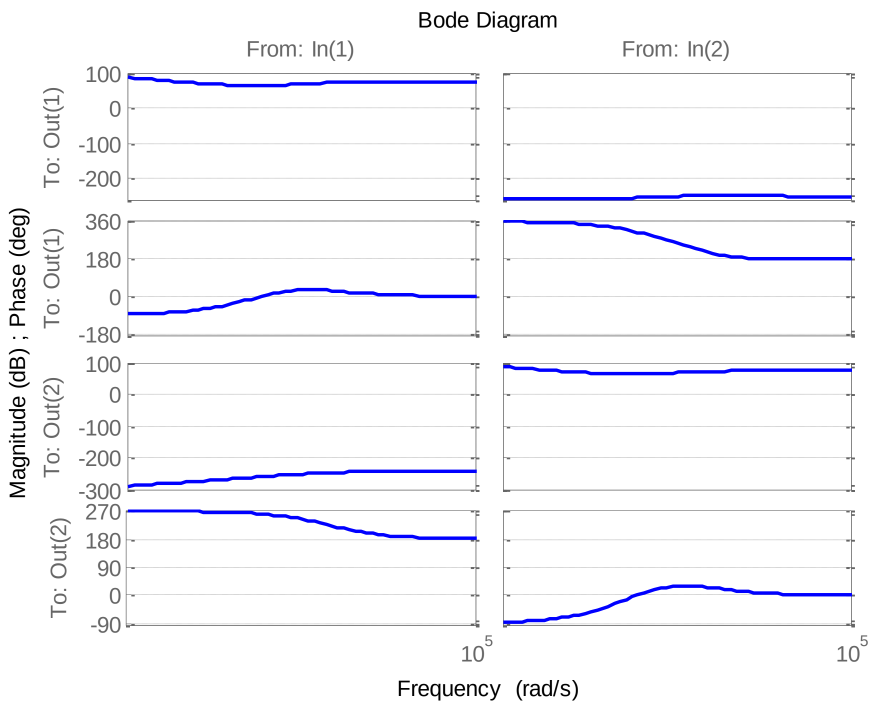

Figure 12 Adjusted PID controller

Control on non-linear plant

In Appendix 2 the designed controller is tested on the linearized plant and in the following it is tested on the non-linear model developed in Spacar (see the block named Robird in the block diagram; Figure 13). Hereby approximations of the aerodynamic forces (see Appendix 3) have been added to the model as plant input disturbances (see Figure 13). From these results (especially Figure 16) it is clear that for the controlled non-linear system, the phase shift of $phs = 7° = 0.1222[\mathrm{rad}]$ is reached with an accuracy of $e_{max} = \pm 0.1° = \pm 0.0017[\mathrm{rad}]$ for a flapping frequency of $f = 7$ $[\mathrm{Hz}]$.

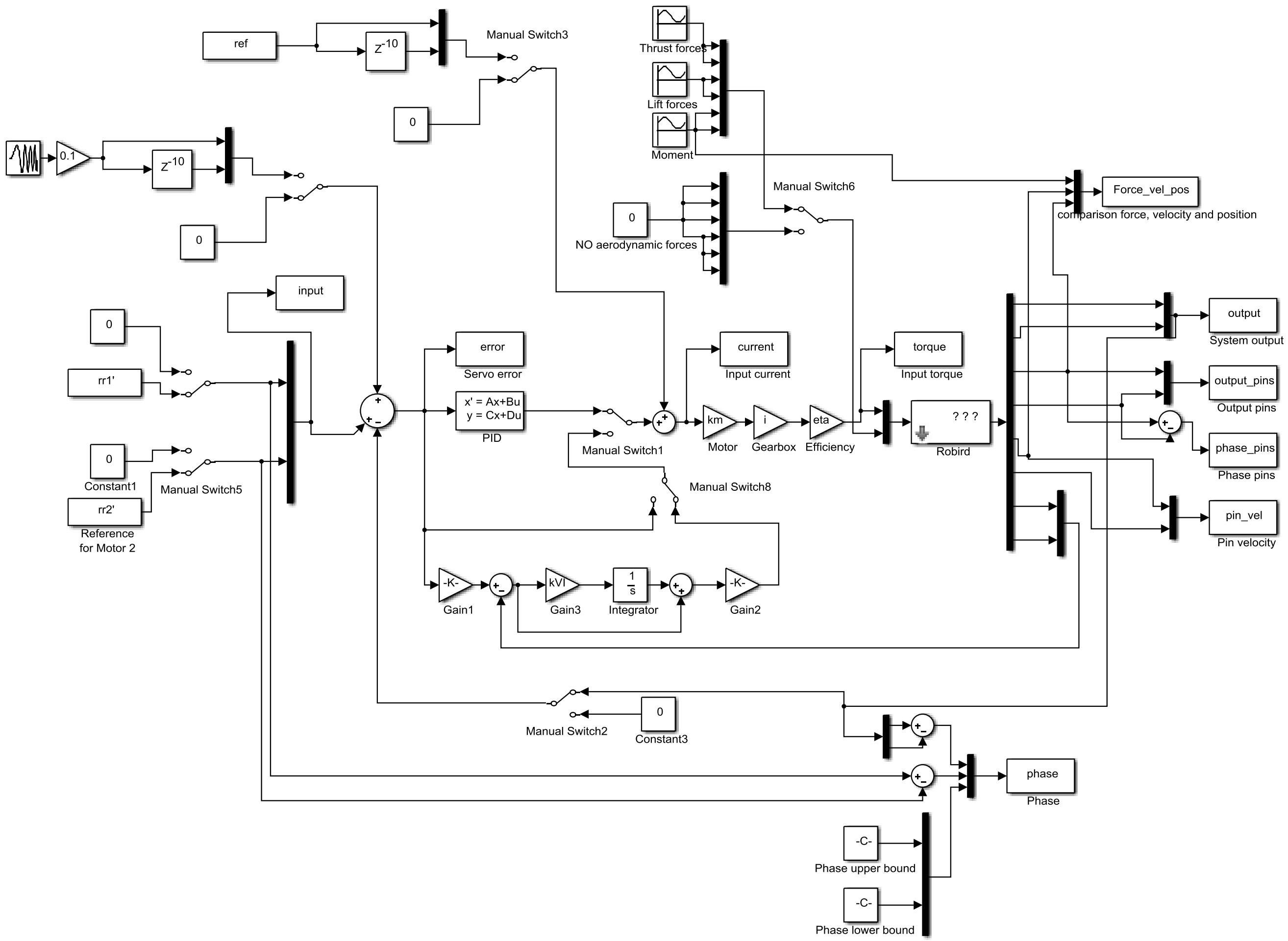

Figure 13 Block diagram nonlinear system

The controlled non-linear system gives the following results:

System output:

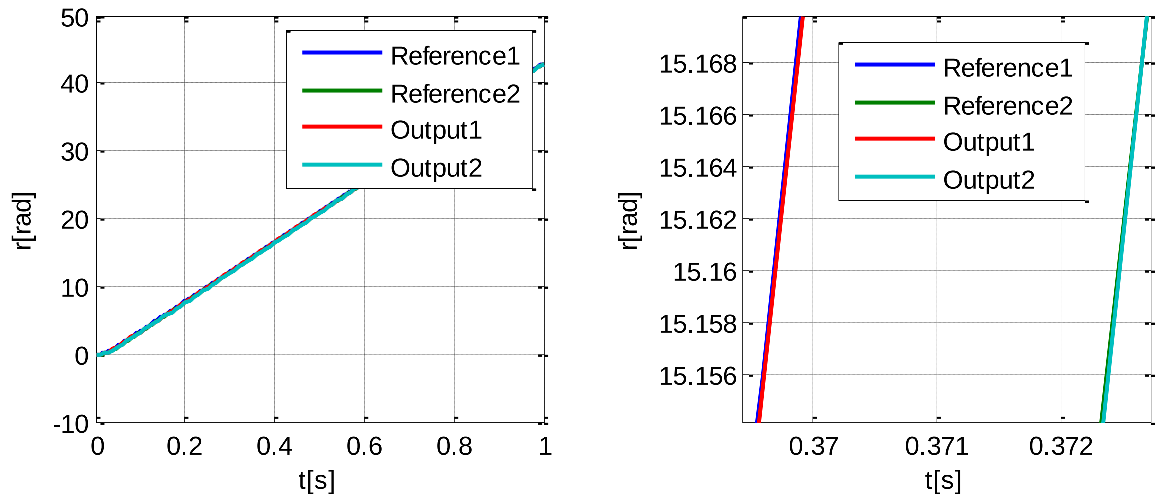

Figure 14 System output of controlled non-linear system

Servo error:

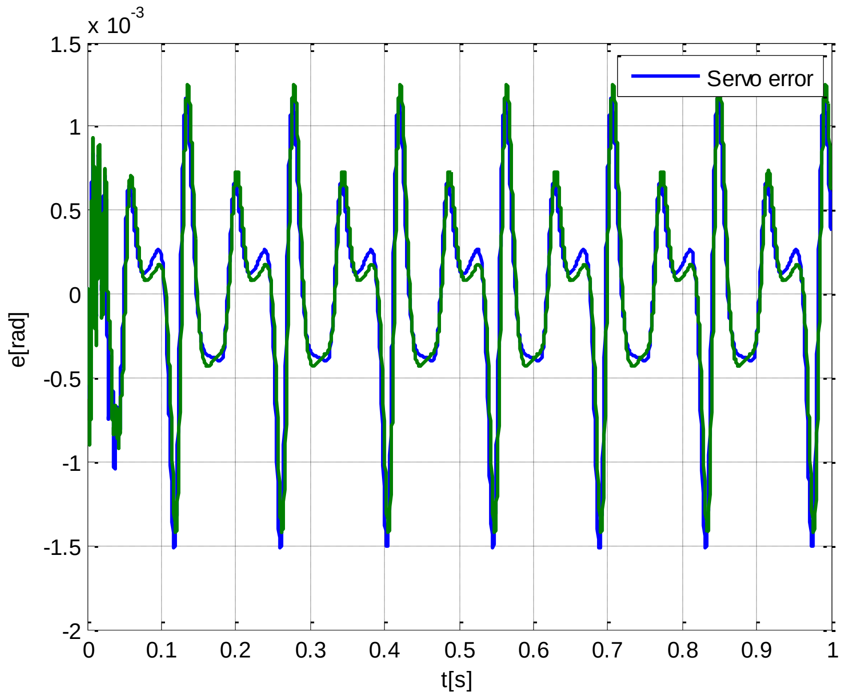

Figure 15 Servo error of controlled non-linear system

Phase shift:

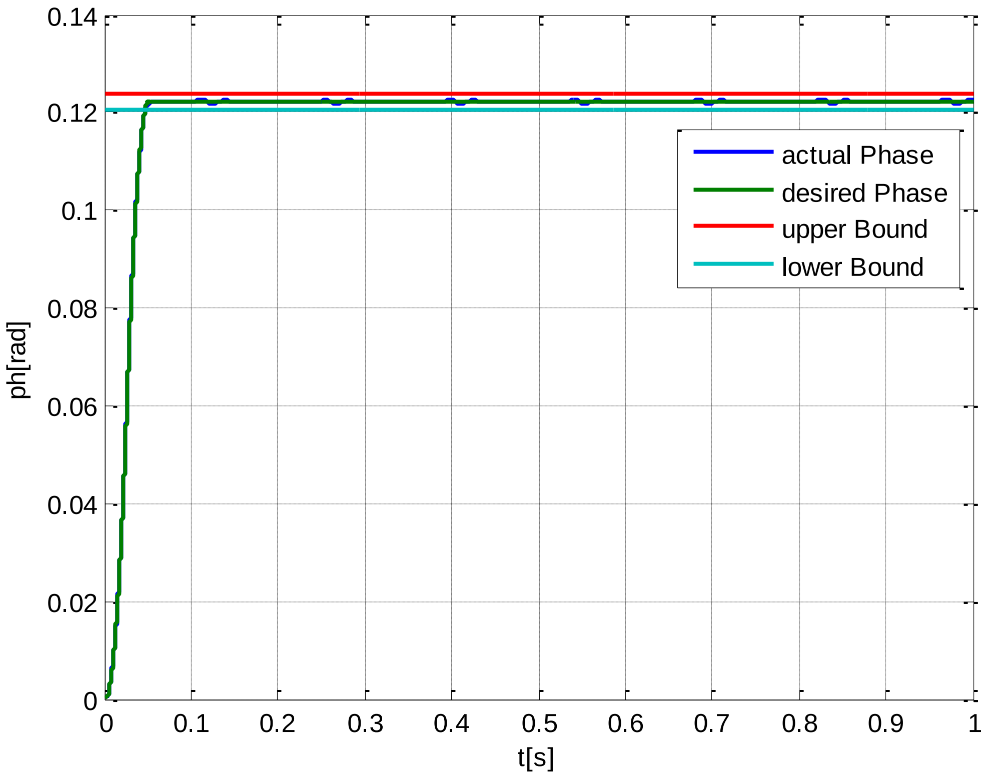

Figure 16 Phase shift of controlled non-linear system

3.2 Mechanical Solution

The main idea here is to mechanically fix the phase shift phs through friction, in particular by using a disc frictional connection. The frictional connection between the discs is established by preload provided by a connection through a bolt. The frictional disc connection ensures that the phase shift is adjustable with an accuracy as high as the measuring equipment allows (see Figure 18)

From the calculations (see Appendix 4) it followed that with a frictional (aluminum) disc connection with a disc radius $r = 0.015$ [m], whereby sufficient preload can be applied by means of a $r_b = 4[\mathrm{mm}]$ radius aluminum bolt (i.e. a M8 – 1.25 bolt), the phase shift can be fixed well to an accuracy as high as the measuring equipment allows. Appendix 4 also illustrates that a spur gear with modulus 1, 36 teeth and a width of 10 [mm] and a radial ball bearing of type 6705 2RS are mechanically sufficient.

Remaining requirements

As Figure 17 illustrates, the setup is oriented vertically, which was required due to the restriction imposed by the wind-tunnel dimensions. The wind tunnel cross-section has a width of 0.9 [m] and a height of 0.7 [m]. Considering the wing with length 0.5 [m] and a flapping angle between 0.6 [rad] and -0.65 [rad] a vertical orientation is more desirable in order to reduce flow disturbance near the walls. As figure 18 illustrates, the setup represents a symmetric half of the actual mechanism in order to obtain interpretable measurements. As is evident in Figure 17 the setup is provided with an aerodynamic shield to reduce flow disturbances. This shield abides by the symmetric requirement. For details on the fabrication of the shield see Appendix 4.4.

3.3 Comparison and choice

Control Solution

From Figure 16 it followed that for the control solution the phase shift of $phs = 7° = 0.1222[\text{rad}]$ is reached with the desired accuracy of$e_{max} = \pm 0.1° = \pm 0.0017[\text{rad}]$. The drawback of the control solution is that it is less reliable than the mechanical solution.

Mechanical Solution

From the calculations (Appendix 4) it followed that with a frictional (aluminum) disc connection with a disc radius $r = 0.015\ [\text{m}]$, whereby sufficient preload can be applied by means of aM8 – 1.25 bolt aluminum bolt, the phase shift can be fixed well to an accuracy as high as the measuring equipment allows. Although the mechanical solution is more reliable than the control solution, it restricts freedom for experiments significantly. Viz. during operation the phase shift cannot be changed.

Choice

Taking the pros and cons of both solutions in consideration, there is concluded that the most desirable solution is a combination of them both (see Figure 17 and Figure 18). In this way the control solution may be used when more flexibility in doing experiments is required and the mechanical solution may be applied when only a constant phase shift is required or when the control solution fails.

3.4 Equipment selection

The test setup is equipped with two (servo) motors and a 6-DOF force sensor. The placement of this equipment in the Spacar model is indicated in Figure 19 by means of arrows. The two motors are connected in the nodes as indicated by the green arrows and the placement of the force sensor is indicated by the red arrow.

In Figure 20, a complete schematic overview is given for the chosen gearbox, motor, encoder and control unit and the achieved requirements. The selection of these equipment is discussed in Appendix 5 in more detail. In Appendix 5.2.1 and 5.2.2 the selection of an appropriate 6-DOF force sensor and the selection of an appropriate power tool are discussed respectively. In Appendix 8 a brief discussion is given on the working principles of the chosen 6-DOF sensor.

In Figure 22 a schematic overview is given of the applied hardware and software of the complete setup (see Figure 21). Motor Control: Using Elmo controllers with the Composer software, position control is applied on the Maxon motors which are provided with encoders to measure the position. Communication between the Elmo controllers and the Composer software is established through a dual RS232 serial connection using a USB-COM232-PLUS2. Both motors are controlled simultaneously through programs written in the Elmo Studio (see Appendix 7.2). Force measurement: Voltages supplied by the load cells during measurements are first amplified and then, through an NI DAQ platform, are sent and saved to an NI PCI-6221 card on an xPC target computer. With a host computer a DAQ application is developed in Matlab/Simulink and build/downloaded to the target computer via Ethernet connection enabling saving measured data. The measured data is processed and compared to results from the non-linear model developed in Spacar and run in Simulink.

For an overview of all parts and their costs, see Appendix 9.

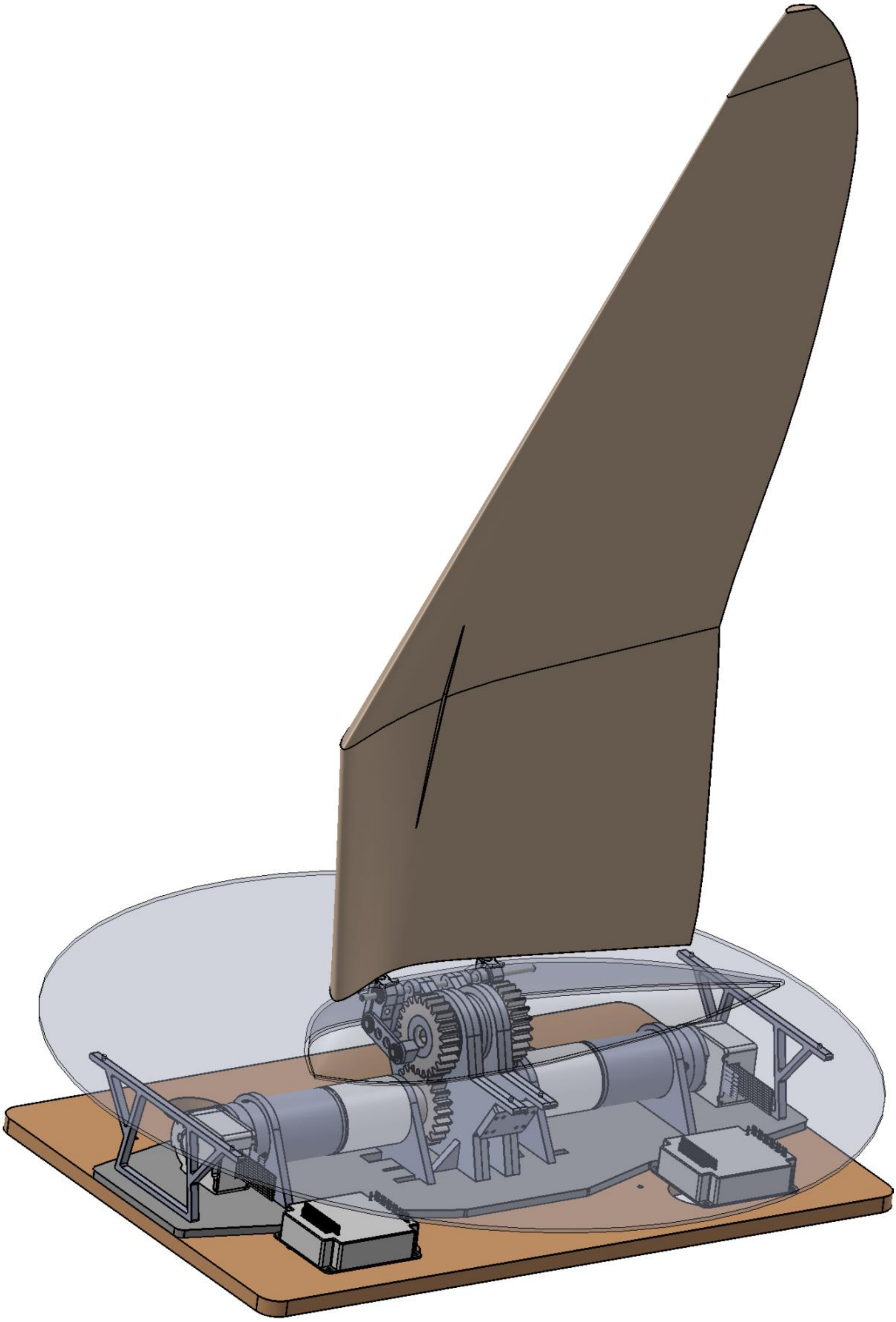

Figure 17 Chosen design concept: A combination of the control and mechanical solution

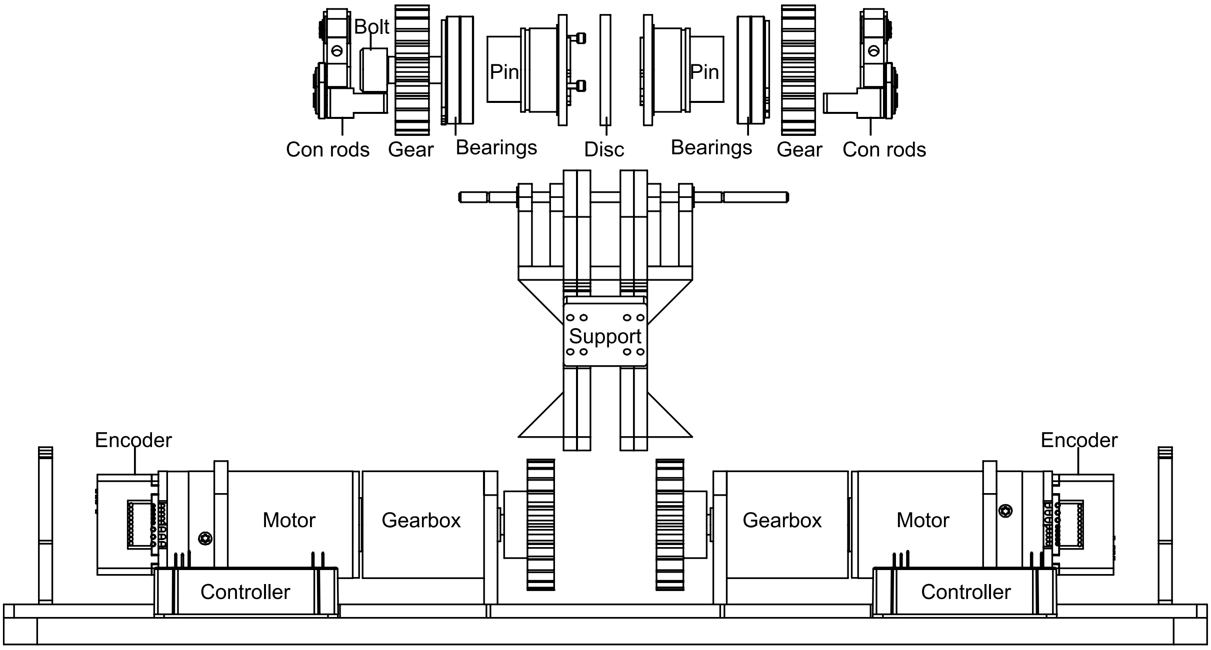

Figure 18 Exploded front view of the setup (without force sensor, wing and aerodynamic shield)

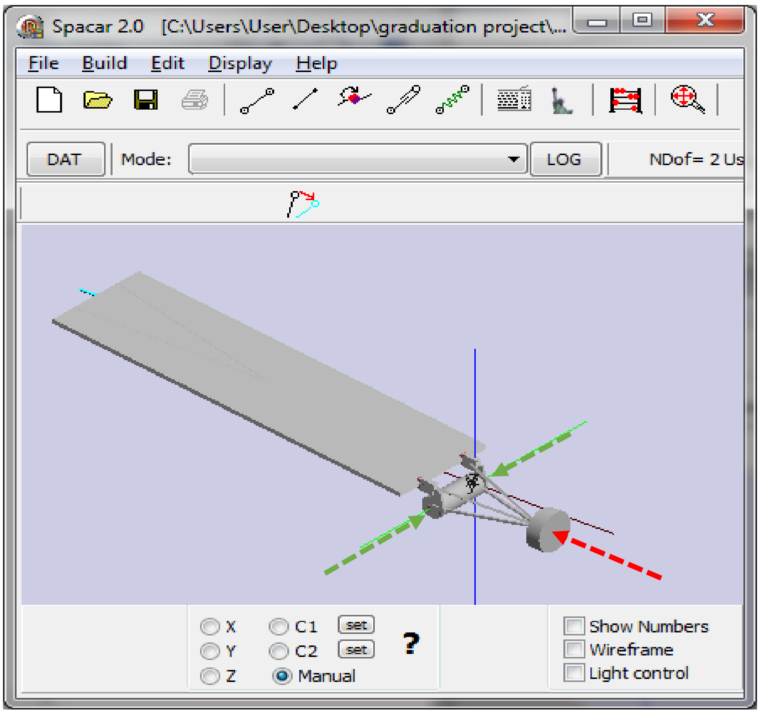

Figure 19 Spacar model

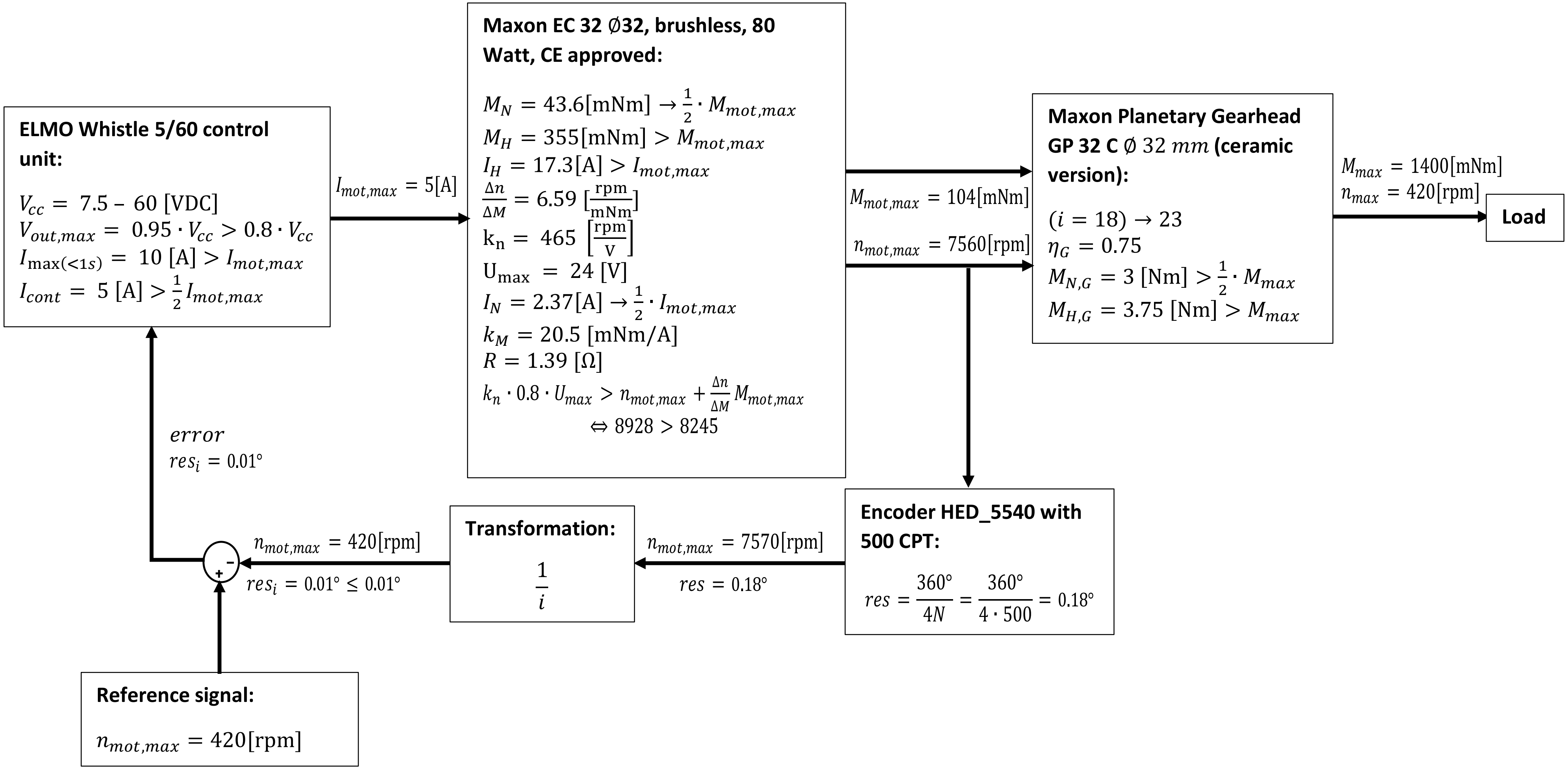

Figure 20 Complete overview of the chosen equipment and the achieved requirement for the control solution

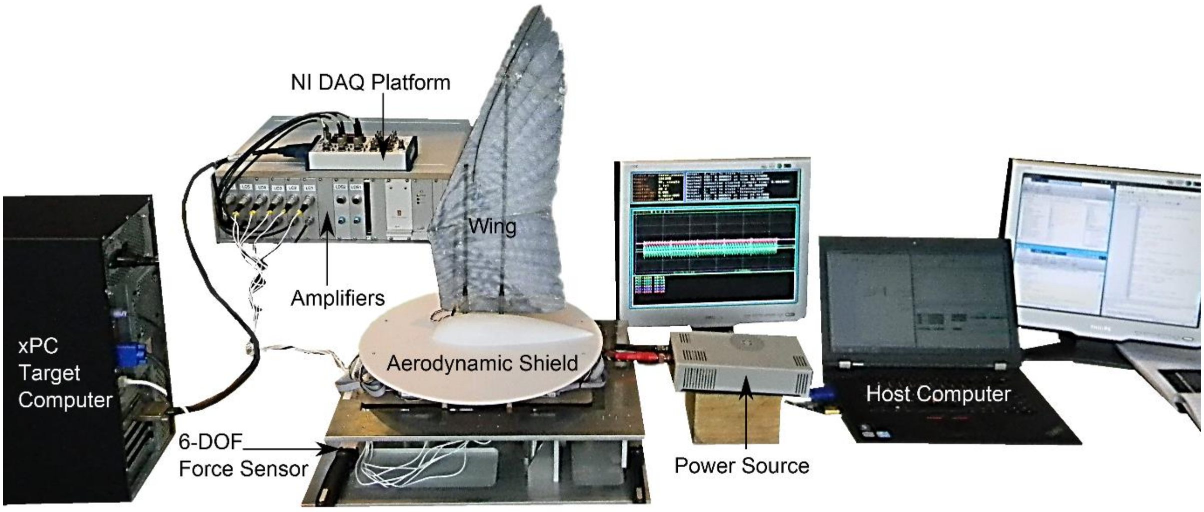

Figure 21 Robird wind tunnel test setup

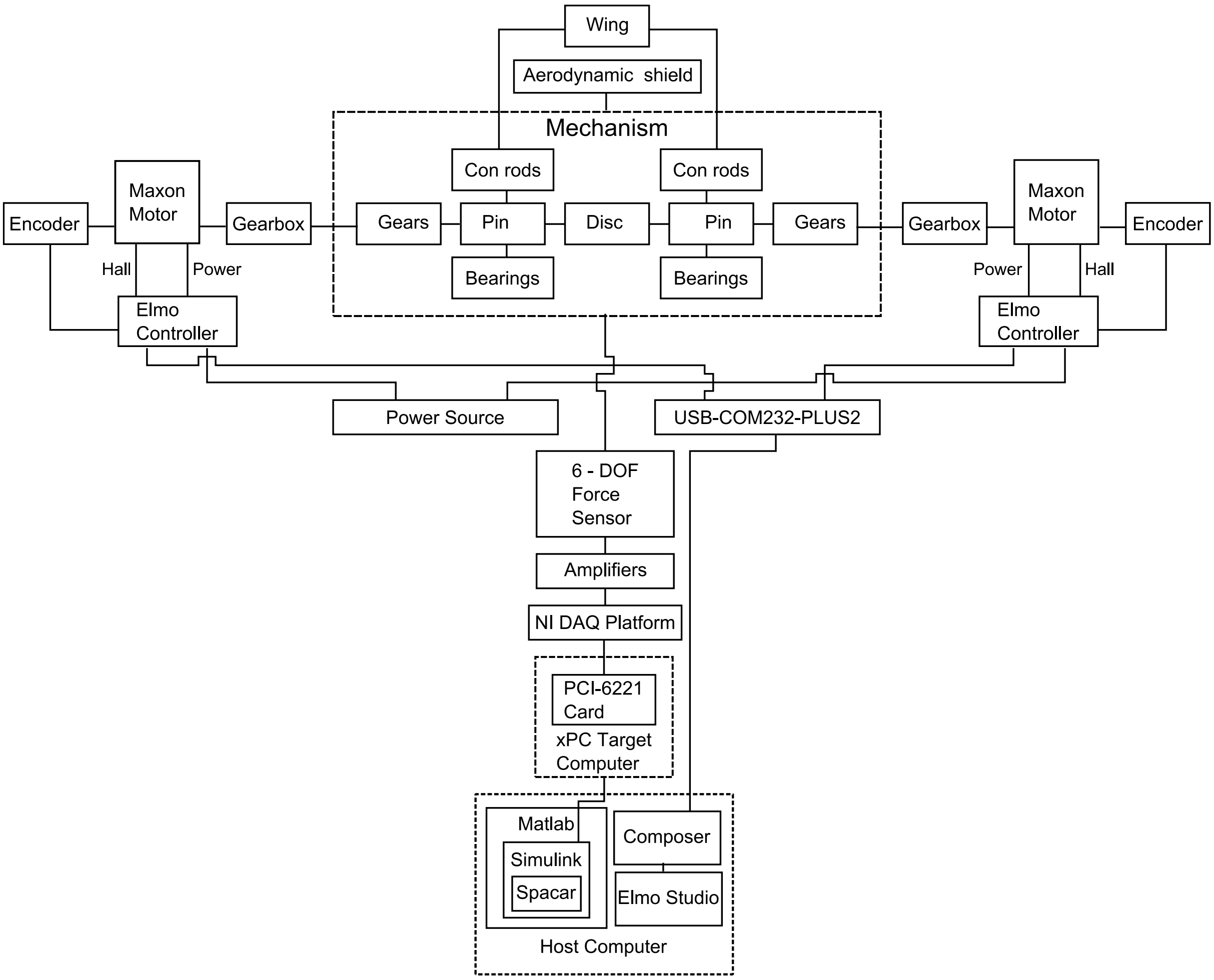

Figure 22 Schematic overview of the applied hardware and software.

4 System identification and parameter estimation

4.1 Identification plan

Actual open loop (upside down configuration) identification

In this section open loop identification is conducted on the stable upside down configuration (see Appendix 6). The system is excited with an input current and the output angle is measured. Subsequently, state space identification is conducted in Matlab ident. The following current input signal is chosen for system excitation (see the plot of u1 in Figure 23; also see Appendix 6):

- Signal type: In order to capture a number of frequencies in one signal a chirp signal is used for current input.
- Frequency range: Considering the developed model as sufficient guidance (relevant resonances at $\omega_{R_{\text{low}}} = 0.95\ [\text{Hz}], \omega_{AR,1} = \ \omega_{AR,2} = 6.8\ [\text{Hz}]$ and $\omega_R = 9.6\ [\text{Hz}]$) (see Figure 5), a frequency range of 0 [Hz] to 10 [Hz] is chosen.
- Signal amplitude: In order to excite the system sufficient enough while keeping the flapping angle small to neglect aerodynamic forces, an amplitude of 0.2 [A] is chosen.
- Sample frequency: The sample time is restricted by the Nyquist frequency ($\omega_N = \frac{\omega_s}{2} = \frac{1}{2t_s}$) and the highest relevant frequency (ω_R), also see Appendix 6:

57 $\omega_N > 5 \cdot \omega_R$

For the sample frequency then applies:

58 $t_s < \frac{1}{10 \cdot \omega_R}$

Hence, with $\omega_R = 9.6\ [\text{Hz}]$ a chosen sample time of $t_s = 0.0072\ [\text{s}]$ is sufficient.

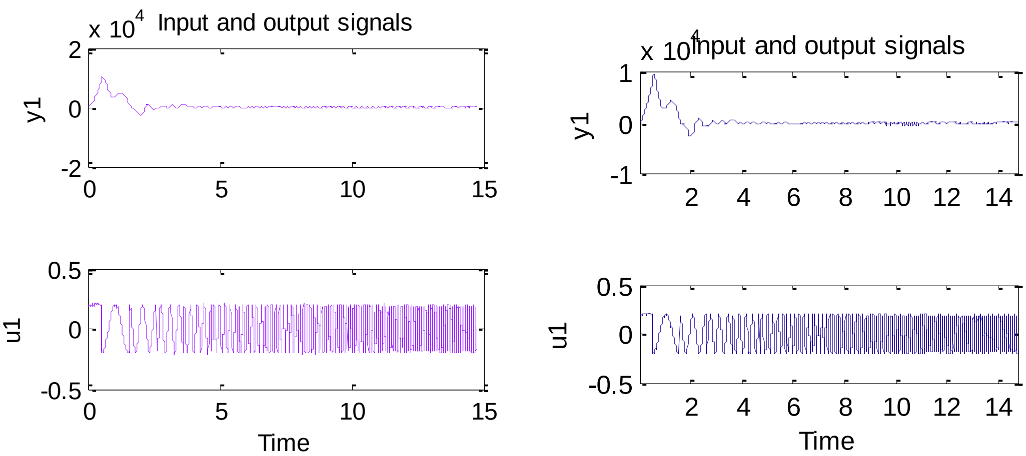

Figure 23 system output (position before gearbox; y1 in [counts]) and input u1 (motor current in [A]). Left: Working data and right: Validation data

4.2 Identification results

Order estimation: In ident (Matlab identification tool) a state space model is estimated. From the singular values, first the system order is estimated to be four as expected (see the left side of Figure 24). Frequency response: Next the state space of the system is estimated and the frequency response is plotted. Model residuals: In order to discuss the accuracy of the estimated model the residuals are plotted (see the left plot in Figure 25).

The fourth order (see Figure 24) estimated system exhibits all three resonances, $\omega_{R_{\text{low}}}, \omega_{AR,1} = \omega_{AR,2}$ and ω_R. This is evident in the frequency plot (see Figure 24) and can also be seen when closely observing the zoomed in working data (see the right part of Figure 25). As the left part of Figure 25 illustrates, i.e. the cross correlation of the input and output data is within the confidence bounds, the estimated model is accurate.

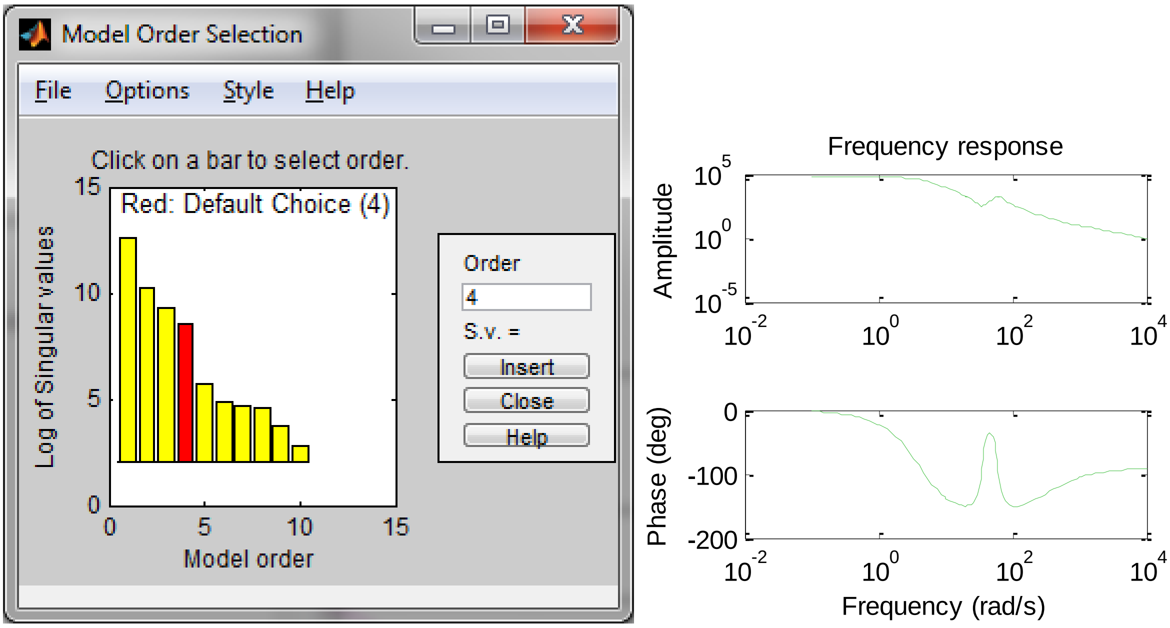

Figure 24 Left: State space order estimation in ident; Right: state space estimated system

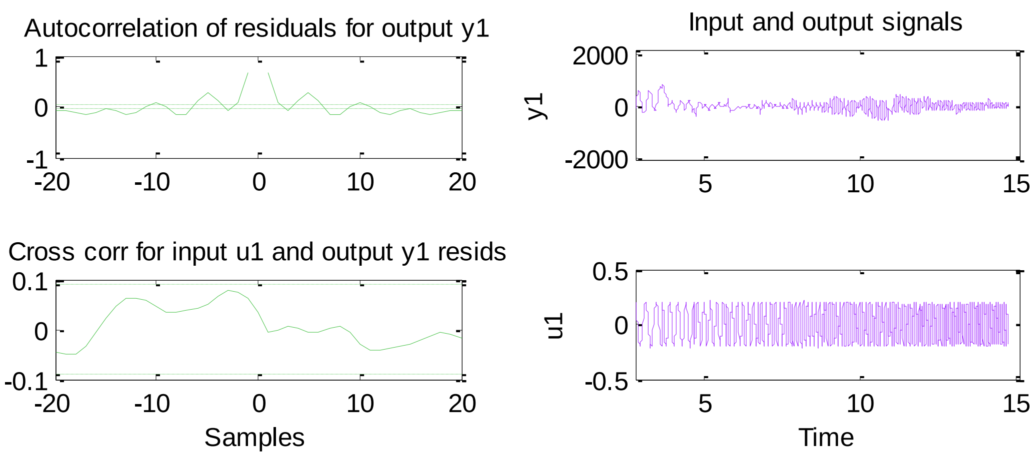

Figure 25 Left: model residuals; Right: zoomed in working data

5 Model validation and controller redesign

Model validation: Comparison frequency response

Previous to comparing the frequency responses, system damping is measured and added to the Spacar model (see Appendix 6.2). Comparing the frequency response of the estimated system and the modeled system shows that the model fits the measured plant relatively well (see Figure 26). To a great extent, the various resonances agree with each other.

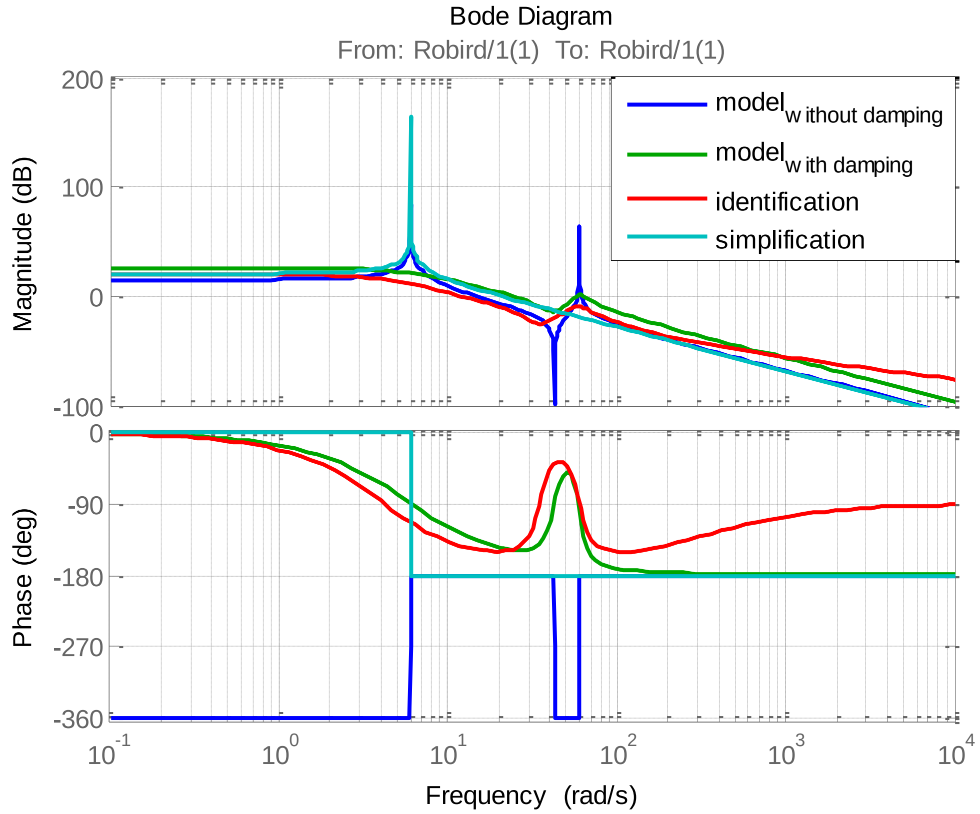

Figure 26 Frequency response of the modeled and estimated system

Controller redesign

Considering the model matches the identified plant well, the controller redesign is considered redundant. I.e. the simplified model based on which the controller has been designed (see equation44) matches the low frequency behavior of the model well.

However, due to limitations of the applied ELMO controllers, application of PID controller did not seem straightforward, instead cascaded position (P) velocity (PI) control is applied. This PIP controller is tweaked using tuning rules as described in Appendix 7.

6 Controller implementation and tweaking

Due to mechanical limitations of the wing, the controlled system is tested for a flapping frequency up to 4 [Hz], rather than 7 [Hz] that is achieved in-flight. As mentioned previously, due to limitations of the ELMO controllers a tuned PIP controller is implemented instead of the designed PID controller.

From the results (especially Figure 29) it is clear that for the controlled non-linear system, at a flapping frequency of 4 [Hz], the phase shift of $phs = 7° = 0.1222[\mathrm{rad}]$ is reached with an accuracy of $e_{max} = \pm 0.1° = \pm 0.0017[\mathrm{rad}]$. I.e. the target performance of $e_{max} = \pm 0.1° = \pm 0.0017[\mathrm{rad}]$ is reached.

System output:

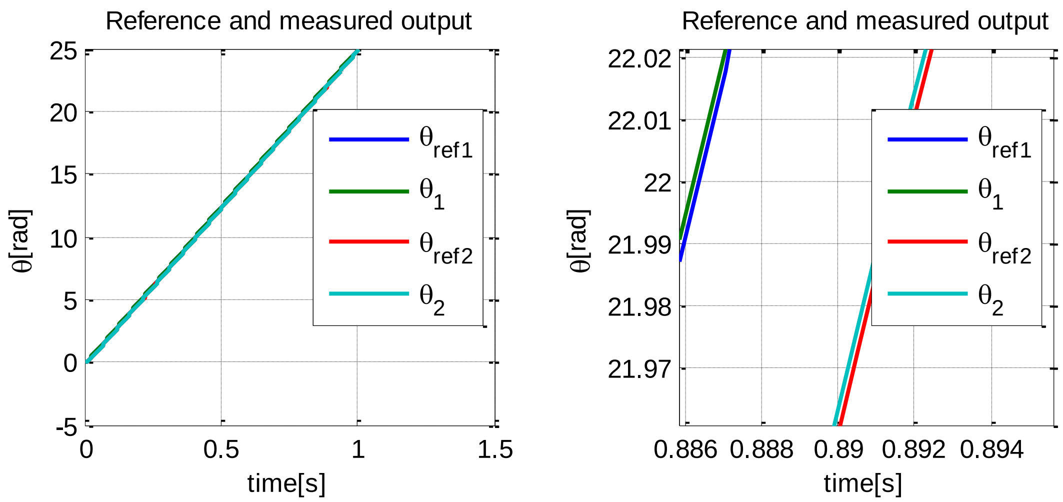

Figure 27 System output of controlled system (Right: Zoomed in)

Servo error:

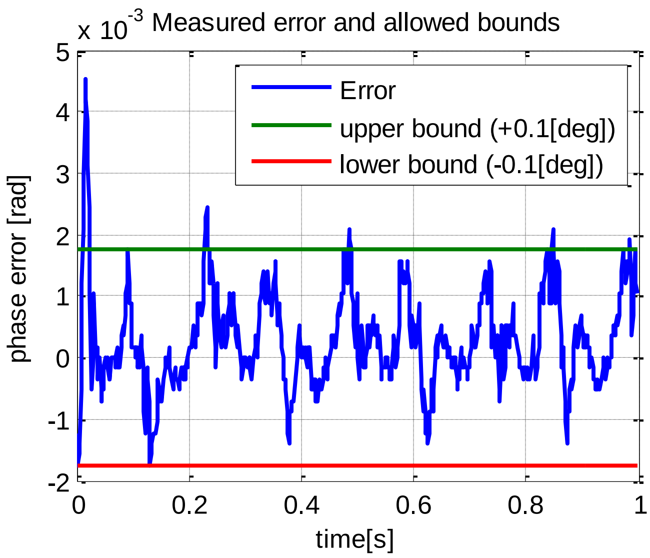

Figure 28 Servo error of controlled system

Phase shift:

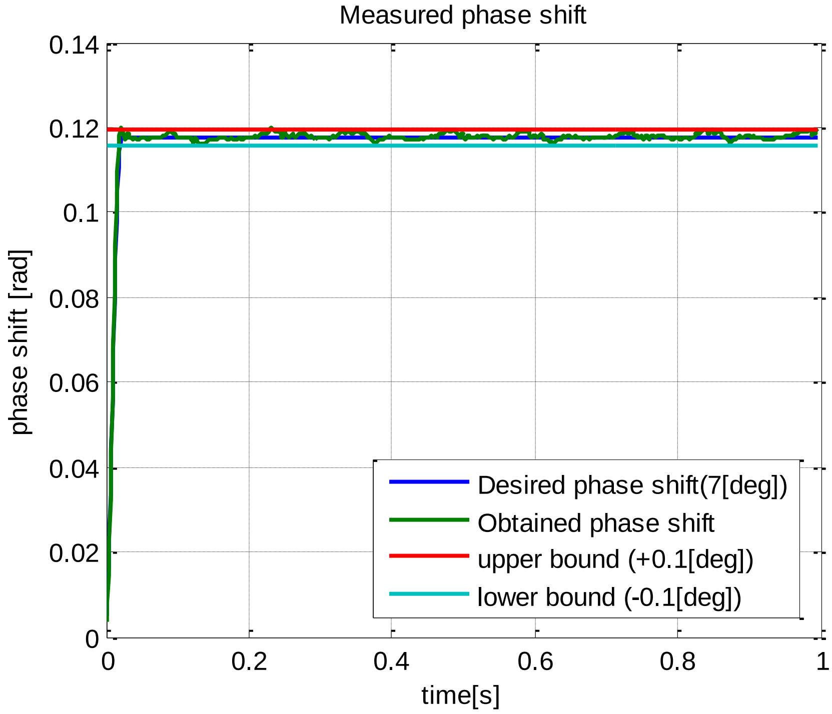

Figure 29 Phase shift of controlled system

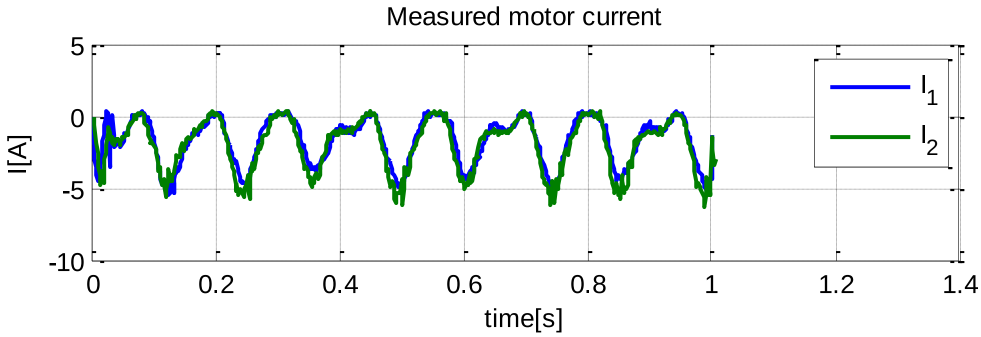

Figure 30 Required motor current

Comparison to simulation

In the following a comparison is conducted between the simulations and experiments of the PIP controlled system. From the error plot of Figure 31 it is clear that, given the same control parameters, even though the measured and simulated current agree rather well in shape (see Figure 32), the measured error is significantly larger than the simulated one. This may be caused by possible occurring loads that are not accounted for in the model.

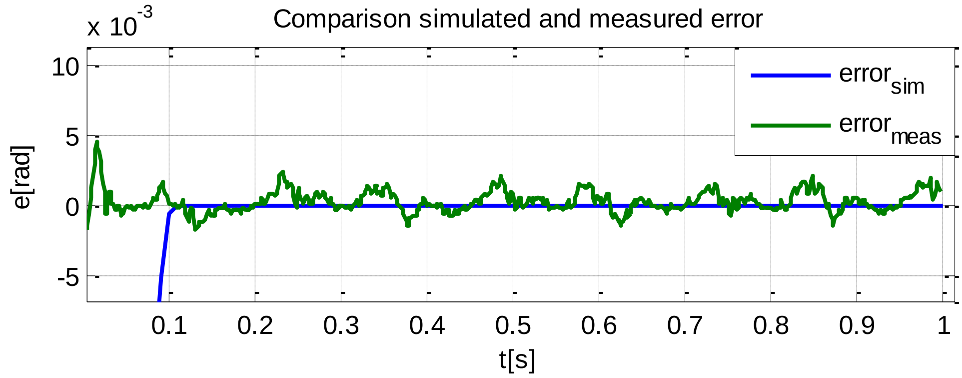

Figure 31 Comparing servo error of the PIP controlled system between simulation and measurements

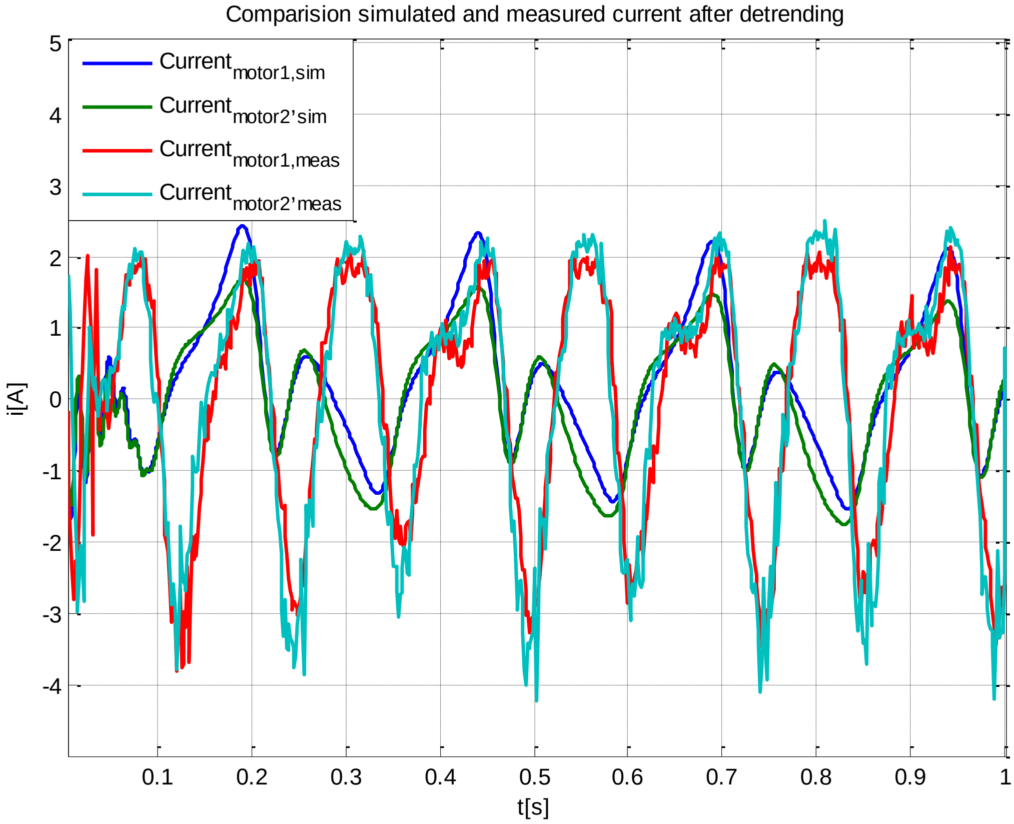

Figure 32 Comparing required motor current (after detrending) between simulation and measurements

Variable phase shift online

The following figures illustrate that online modification of the desired phase shift is possible very well. However these results do not illustrate complete settling of the response due to limited measurement points provided by the used Composer software, i.e. run time is taken small. In Figure 33 to Figure 36 a varying phase shift phs from 0 [°] to 10 [°] in steps of 2.5 [°] is given for references corresponding to 1 to 4 [Hz] respectively.

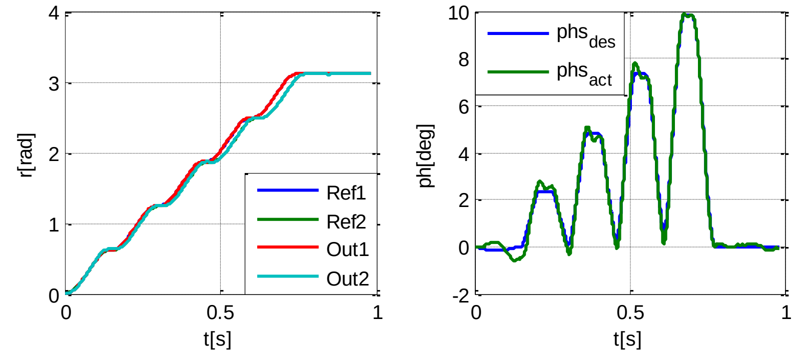

Figure 33 Online phase shift modification: Left: Reference (1 [Hz]); Right: Phase shift

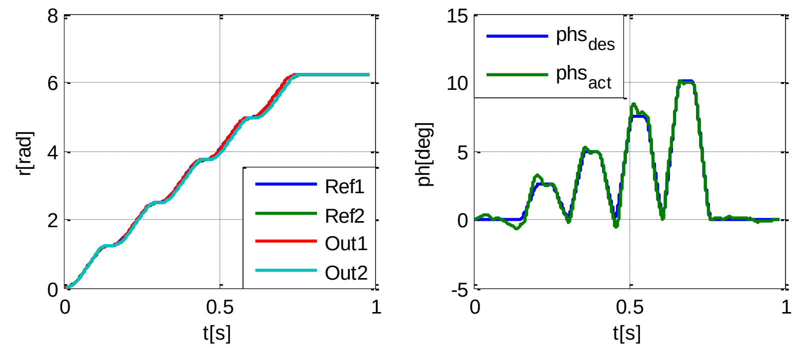

Figure 34 Online phase shift modification: Left: Reference (2 [Hz]); Right: Phase shift

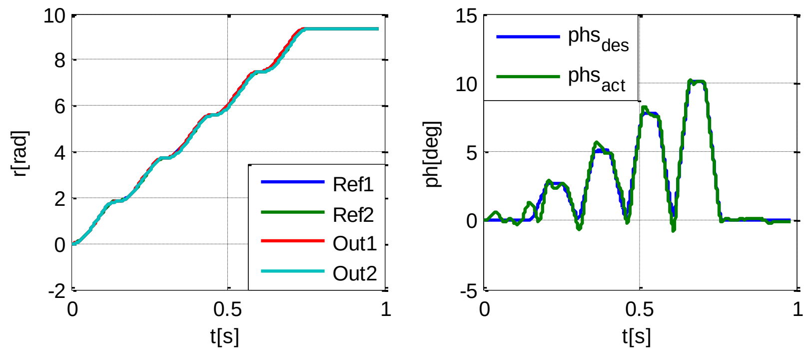

Figure 35 Online phase shift modification: Left: Reference (3 [Hz]); Right: Phase shift

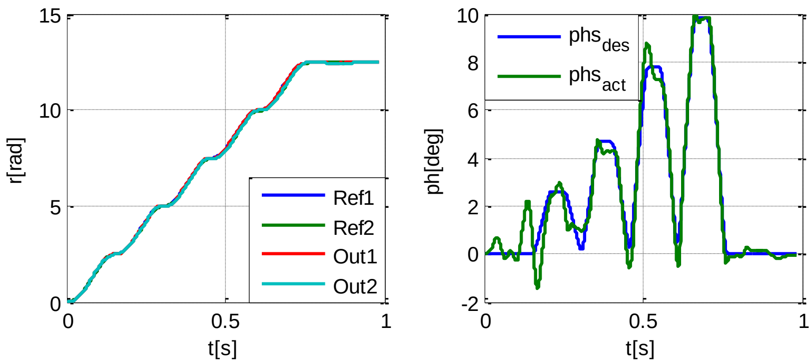

Figure 36 Online phase shift modification: Left: Reference (4 [Hz]); Right: Phase shift

7 Measurement aerodynamic loads

As one of the purposes of the developed and designed test setup is to gain understanding in the aerodynamics of Robird and ultimately of actual birds, there is aimed at measuring aerodynamic loads on Robird (and its wings) for gathering empirical and validation data for analytical and numerical studies on (Ro) bird aerodynamics.

In order to measure these forces, the setup is mounted on a 6 – DOF force sensor which measures reaction forces and torques in all directions. The measured reaction loads $f_{meas}^{(o)}$ result from the contribution of inertial forces $M^{(o)}\ddot{x}$, stress resultants $D_{,x^{(o)}}^{T}\sigma$, velocity dependent inertia $h^{(o)}$ and aerodynamic loads $f_{aero}^{(o)}$, see equation59.

59 $$f_{meas}^{(o)} = D_{,x^{(o)}}^{T}\sigma + h^{(o)} + M^{(o)}\ddot{x} + f_{aero}^{(o)}(x, \dot{x}, \ddot{x})$$

In order to distinguish $f_{aero}^{(o)}$ from $f_{meas}^{(o)}$, $D_{,x^{(o)}}^{T}\sigma$, $h^{(o)}$ & $M^{(o)}\ddot{x}$ need to be known and subtracted. This is feasible, as the three latter terms are known from simulation with the developed model (with zero aerodynamic load), i.e.:

60 $$f_{sim}^{(o)} = D_{,x^{(o)}}^{T}\sigma + h^{(o)} + M^{(o)}\ddot{x}$$

With regard to this, the following applies for the contribution of aerodynamic loads to the reaction forces $f_{aero}^{(o)}$:

61 $$f_{aero}^{(o)} = f_{meas}^{(o)} - f_{sim}^{(o)}$$

Subsequently, using a transformation matrix B, the aerodynamic loads transformed on the body $f_{aero}^{(b)}$ can be determined:

62 $$f_{aero}^{(b)} = B^{-1} f_{aero}^{(o)}$$

With:

$$B = \begin{bmatrix} 1 & 0 & 0 & 0 & 0 & 0 \\ 0 & 1 & 0 & 0 & 0 & 0 \\ 0 & 0 & 1 & 0 & 0 & 0 \\ 0 & -z & y & 1 & 0 & 0 \\ z & 0 & -x & 0 & 1 & 0 \\ -y & x & 0 & 0 & 0 & 1 \end{bmatrix}$$

(x, y, z) = coordinate body center

Alternatively, the aerodynamic loads transformed on the Robird wing can be determined:

63 $$f_{aero}^{(b)} = B^{-1} f_{aero}^{(o)}$$

With, in this case:

$(x, y, z) = \big(x(t), y(t), z(t)\big)$ = time/movement dependent wing center coordinate, distractible from simulation.

Determination of aerodynamic loads from measured reaction forces
In the following, aerodynamic loads are determined through the measurement of reaction forces in the origin of the 6-DOF force sensor. These are compared to simulation results followed by the distinction of aerodynamic loads. The loads are then transposed to the center of the body and alternatively to the center of the wing. In the following, this is described in more detail:

1. Measurement of reaction forces: Reaction forces are measured for various frequencies. And for each frequency, the phase shift phs is varied online:

   - Free stream velocity: $U_\infty = 0\ [\frac{\mathrm{m}}{\mathrm{s}}]$
   - Frequencies: $f = 1{,}2{,}3\ \&\ 4\ [\mathrm{Hz}]$ for $25\ [\mathrm{s}]$ per constant f
   - Phase shift: $phs = 0, 2.5, 5, 7.5\ \&\ 10\ [°]$ for $5\ [\mathrm{s}]$ per constant phs

2. Processing measurements: The measured reaction forces are processed according to the following procedure:

   - Calibration: The initial load (weight of the setup) is measured and subtracted from subsequent measurements.
   - Data processing: After calibration, the measured data is filtered, sectioned and averaged:
     - Filtering: the raw data is filtered for a frequency range f_r of: $0.1f \leq f_r \leq 8f$
     - Sectioning: $1\ [\mathrm{s}]$ sections are taken of the $5\ [\mathrm{s}]$ measurements
     - Averaging: the first and last sections are discarded and middle sections are averaged

3. Calculation of aerodynamic loads: Aerodynamic loads are separated from the measurements as follows: $f_{aero}^{(o)} = f_{meas}^{(o)} - f_{sim}^{(o)}$ (see equation61).

4. Transposing loads to center of body: The loads are transposed to the center of the body as follows: $f_{aero;body}^{(o)} = B^{-1} f_{aero}^{(o)}$ with $x = 0[\mathrm{m}],\ y = 0[\mathrm{m}]\ \&\ z = 0.13[\mathrm{m}]$ (see equation62).

5. Transposing loads to center of wing: The loads are transposed to the center of the wing as follows: $f_{aero;wing}^{(o)} = B^{-1} f_{aero}^{(o)}$ with $x = 0[\mathrm{m}],\ y = 0.2\sin(\theta) + 0.025\ [\mathrm{m}]\ \&\ z = 0.2\sin(\theta) + 0.13[\mathrm{m}] + 0.012[\mathrm{m}]$ (see equation63).

Results
In Appendix 8.2, the above procedure is illustrated for $f = 1[\mathrm{Hz}]$ and $phs = 7.5[°]$. In Figure 37 to Figure 40 only the averaged $1[\mathrm{s}]$ sections of the measured and simulated reaction forces are plotted for $f = 1[\mathrm{Hz}]$ to $f = 4[\mathrm{Hz}]$ respectively.

These plots indicate good agreement between measurements and simulations for low frequencies, i.e. frequencies up to $1[\mathrm{Hz}]$. For higher frequencies, i.e. above $1[\mathrm{Hz}]$, the measured forces exceed the simulated ones. This is as expected, because the developed model only captures inertia forces and stress resultants whereas the measurements in addition also capture aerodynamic loads.

Dependency on phase shift phs and frequency f
Results of the averaged aerodynamic loads (see Figure 41) illustrate clear dependency on the frequency f, but not yet on the phase shift phs**.** The frequency dependency is obvious forFx, Fy and Mz which correspond well to thrust, lift and moment aerodynamic loads.

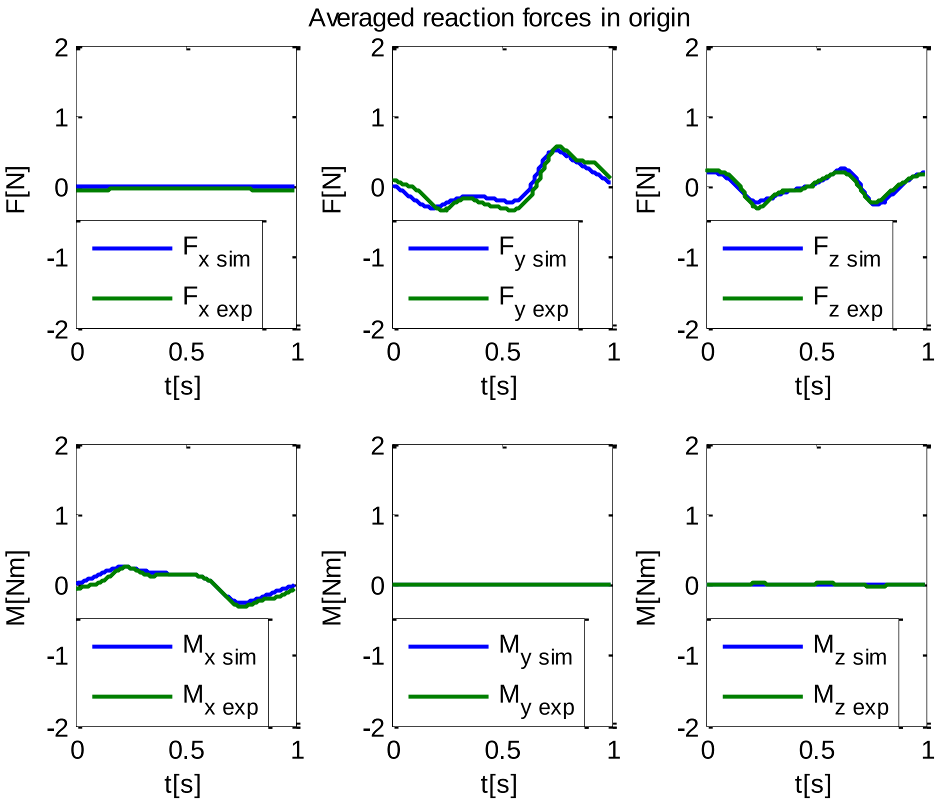

Figure 37 Averaged reaction forces in origin; $f = 1[\mathrm{Hz}]$ and $phs = 7.5[°]$

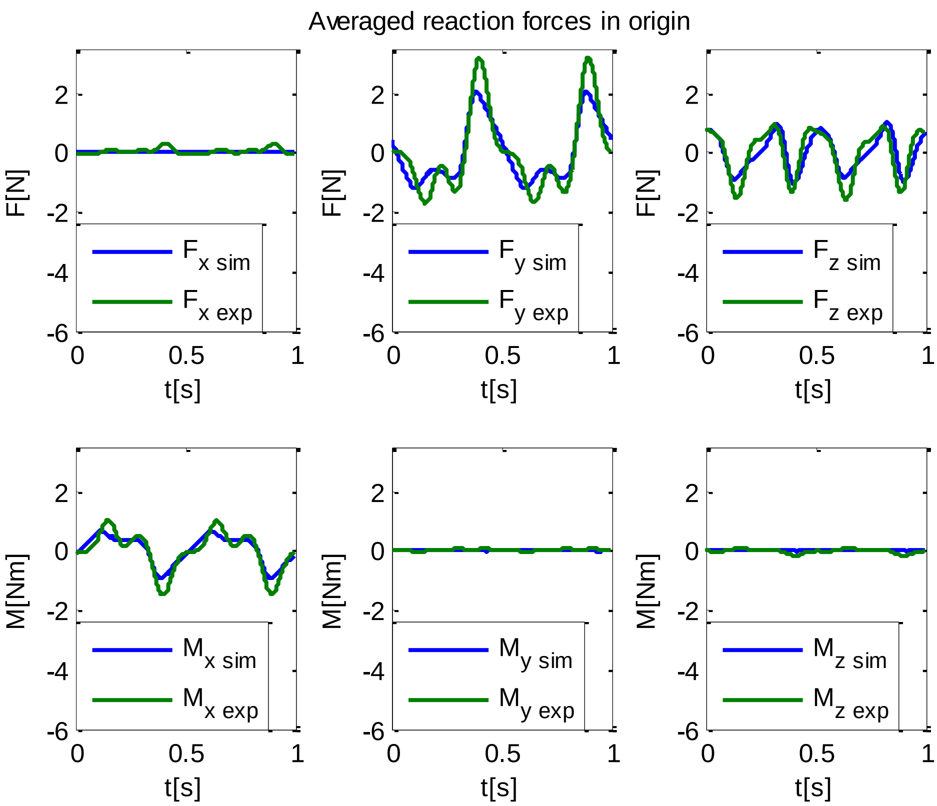

Figure 38 Averaged reaction forces in origin; $f = 2[\mathrm{Hz}]$ and $phs = 7.5[°]$

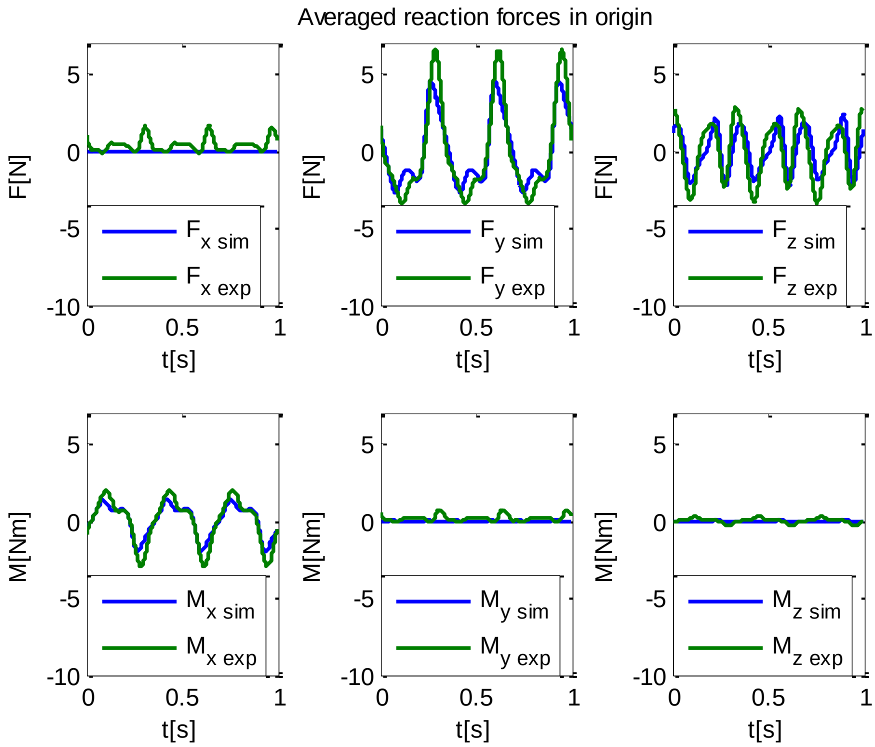

Figure 39 Averaged reaction forces in origin; $f = 3[\mathrm{Hz}]$ and $phs = 7.5[°]$

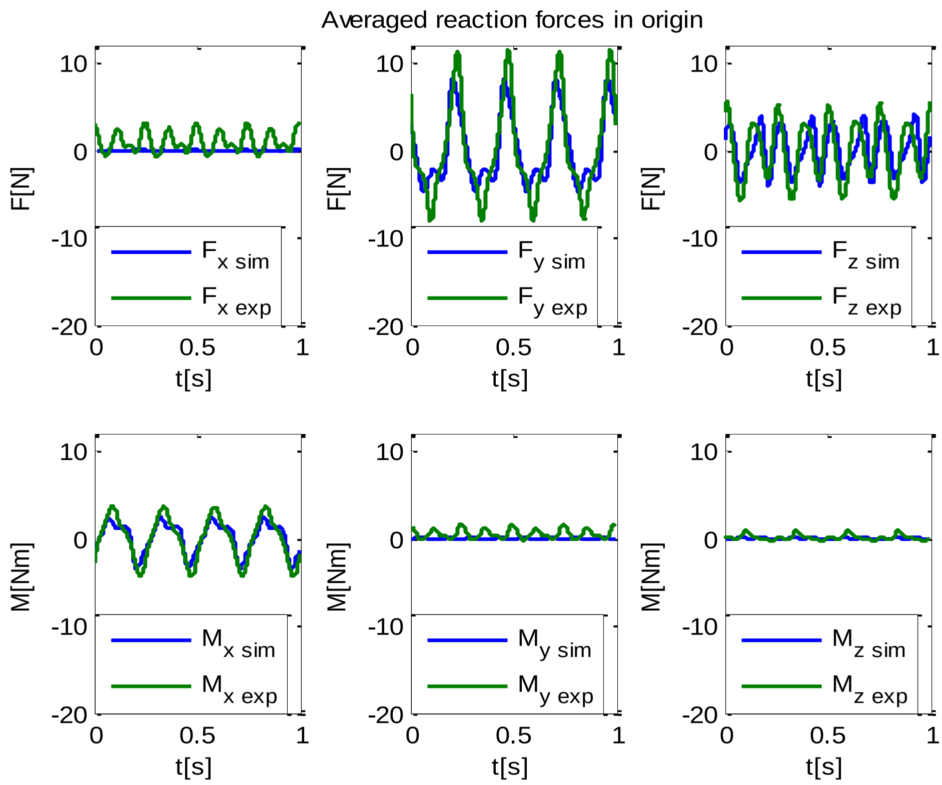

Figure 40 Averaged reaction forces in origin; $f = 1[\mathrm{Hz}]$ and $phs = 7.5[°]$

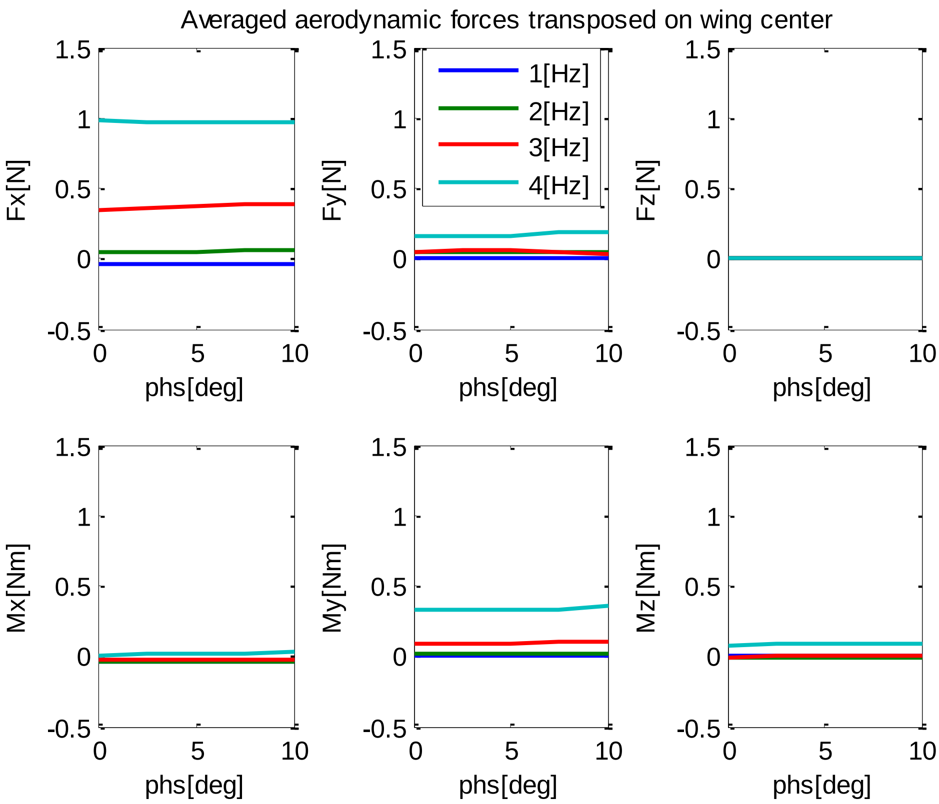

Figure 41 Averaged aerodynamic loads on wing center; $f = [1\ \ 4][\mathrm{Hz}]$ and $phs = [0\ \ 10][°]$

Wind tunnel experiments

The measurements as described in the section above have been conducted in the wind tunnel (see Figure 42) for a number of frequencies $f = [0 - 4]\ [\mathrm{Hz}]$. Per frequency f, the experiments have been conducted for various free stream velocities $U_\infty = [0 - 12]\ [\mathrm{m/s}]$. And per free stream velocity U_∞, experiments have been conducted for a number of phase shifts $phs = [0 - 15]\ [°]$ (varied online). This whole procedure has been repeated for various pitch angles $pitch = [0 - 10]\ [°]$. For purposes of illustration, in Figure 43 the results are depicted for $f = 3\ [\mathrm{Hz}]$ & $pitch = 0\ [°]$ and in Figure 44 the results for $f = 3\ [\mathrm{Hz}]$ & $pitch = 5\ [°]$ are depicted. Only Fx, Fy and Mz which correspond well to thrust, lift and moment aerodynamic loads are plotted. Due to symmetry of the setup other loads, i.e. Fz Mx and My cancel out in the actual Robird.

Figure 42 Wind tunnel measurements

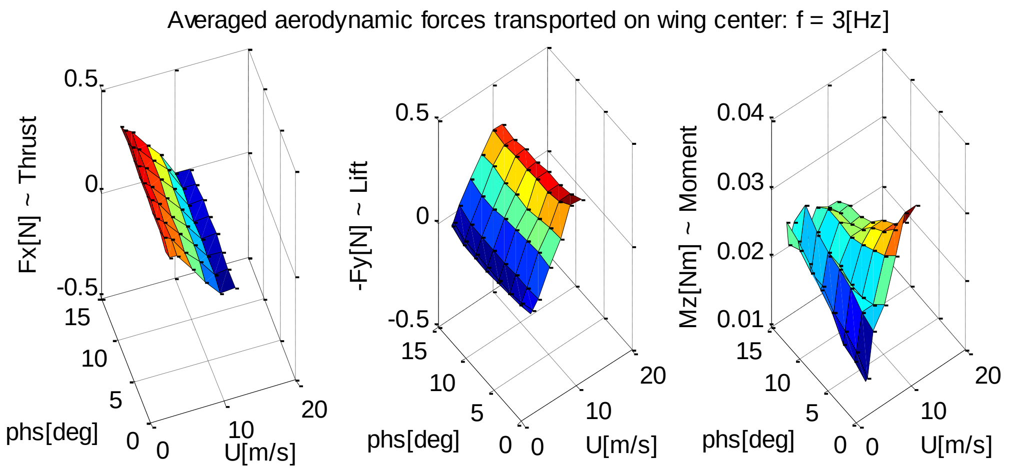

Figure 43 Averaged aerodynamic loads transported on wing center: $f = 3$ [Hz] & $pitch = 0$ [°]

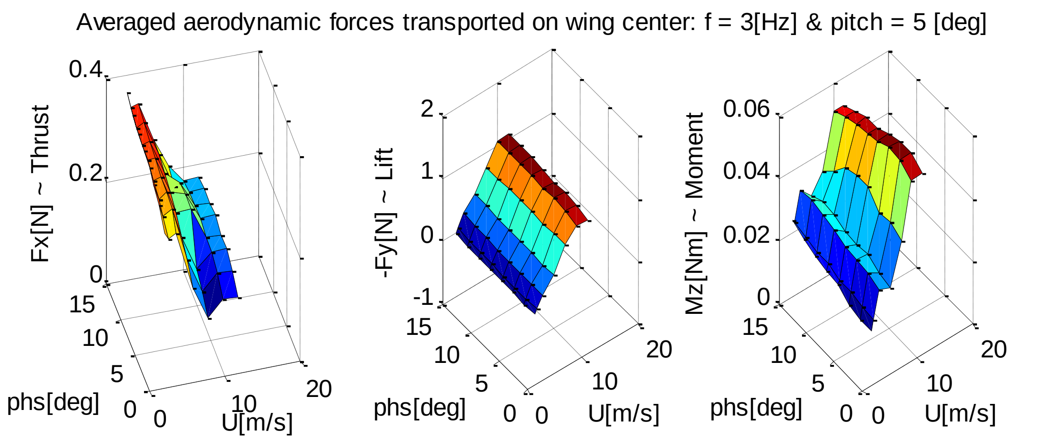

Figure 44 Averaged aerodynamic loads transported on wing center: $f = 3$ [Hz] & $pitch = 5$ [°]

Conclusions

The goal of this project has been to design a wind tunnel test setup for the peregrine falcon Robird. Robird mimics flapping motion by two con rod mechanisms per wing which transform the motor rotational motion into flapping, i.e. plunging and pitching. The latter caused by introducing a phase shift phs between the motion of the two con rod mechanisms.

For freedom in experiments the setup was required to allow for an adjustable phase shift phs typically between 6° and 7° with an accuracy of $e_{max} = 0.1°$ for flapping frequencies up to $f = 7\,[\mathrm{Hz}]$. For this requirement, a control and a mechanical solution have been combined. In the mechanical solution, the desired phase shift is fixed passively/mechanically through a frictional disc connection. In the control solution the desired phase shift phs is fixed actively through the use of two motors. For this solution an optimal PID controller is designed based on a one parameter approach. Simulations with a nonlinear model of the setup mechanism developed in Spacar (including rough estimates of aerodynamic loads introduced as disturbance) have shown that with the designed PID controller a phase shift of $phs = 7\,°$ is obtained with a deviation of below $e_{max} = 0.1°$ for a flapping frequency of $f = 7\,[\mathrm{Hz}]$.

After the realization of the actual setup, state space system identification and parameter estimation is conducted using ident (Matlab). From the singular value plot, the model order was estimated to be four which is in good agreement with the developed model. All main resonances were captured well by the estimated plant. The estimation was proven correct as the model residuals were located within the confidence bounds. The results indicate that the developed model, which is a symmetric half of the Robird mechanism, forms a good basis for identifying the body dynamics of Robird.

Due to limitations of the applied ELMO controllers on the actual setup, cascaded position (P) velocity (PI) control is applied instead of PID control. To prevent the wing from breaking, a flapping frequency of 4 [Hz] is applied during the tests. After tweaking and implementation of the PIP controller, the results show that the desired phase shift phs is obtained within $\pm 0.1°$. From comparison with simulations, using a PIP controller with the same parameters as in the implementation, it follows that the current profiles do agree well qualitatively. However, in the simulation a much higher accuracy is obtained. This rises the suspicion of higher loads and disturbances in the actual setup, possibly caused by e.g. frictional losses and/or higher aerodynamic loads than estimated.

The setup was required to allow for measurement of reaction forces and torques in all directions in order to measure aerodynamic loads. To this end a 6-DOF sensor is mounted at the base of the setup. Initial reaction force measurements have indicated good agreement with reaction force simulations for low frequencies, i.e. frequencies up to $1[\mathrm{Hz}]$. For higher frequencies, i.e. above $1[\mathrm{Hz}]$, the measured forces exceed the simulated ones. This is as expected, because the developed model only captures inertia forces and stress resultants whereas the measurements in addition also capture aerodynamic loads. In this way, for wind tunnel experiments to be followed, aerodynamic loads can be distinguished by subtracting the measurements with the simulations.

Recommendations

1. **Identify causes of discrepancies between results and expectations**
    a. *Measure aerodynamic forces*: As is discussed already, based on the applied PIP controller, the simulated error is significantly smaller than the measured one. This suggests higher loads than expected. Because through identification confidence is gained in the model and thus the modeled loads (due to inertia, stiffness, damping and gravity), there is suspected that the aerodynamic loads are more probable to be higher than estimated. Measuring these loads would clarify this.
    b. *Identify backlash and frictional losses*: Other possible causes for higher loads than expected which are entitled of investigation are backlash and frictional losses.
    c. *Use more appropriate software (e.g. 20-sim or xPC) to apply the designed controller directly and for synchronization of all measurements*: Another possible cause for not meeting the performance target is application of a PIP controller instead of the designed PID controller. Also, in order to prevent synchronization problems it is useful to use one software platform for all measurements, e.g. either xPC target (Matlab) or 20-sim 4C (20-sim).

2. **Conduct further research with the designed setup**
    a. *Understanding aerodynamics*: The test setup has been designed with the general purpose to provide understanding in the dynamics of Robird, especially the aerodynamics behind its far from fully understood flapping flight. A starting point is studying the influence of flapping frequency and the angle of attack on the flight of Robird.
    b. *Further model development*: As was one of the objectives of the design, the setup represents a symmetric half of the flapping wing mechanism of Robird. Identification data retrieved from this setup can then be used as validation data for dynamic models describing the complete flapping wing mechanism of Robird. The developed model can then be used for various purposes such as providing understanding in the dynamics of Robird and for controller design.
    c. *Lift off*: The current version of Robird cannot establish lift off on its own. Typically it is thrown into the air while already flapping in cruising mode. A lift off mode is absent. This will most likely require more advanced wing kinematics, i.e. presumably at least one more degree of freedom in the wing is required. This can be tested using the designed setup.
    d. *Energy saving*: Currently Robird is assisted with a battery providing it with power to fly only as long as up to ten minutes. Keeping Robird in the air longer is a challenge. Possibilities to save energy such as adding spring elements to store and recover energy can be studied using the designed setup.
    e. *Variable phase shift during flight*: Up till now the flight of Robird has been carried out with only a fixed phase shift phs. The influence of varying the phase shift phs during flight can be studied using the test setup, as it does allow this degree of freedom.
    a. *Energy generation*: The setup may be used for energy generation exploration. One way of studying this is by imposing fluid flow (air flow/wind or water flow) onto the unactuated wing and convert wing flapping, i.e. plunging and pitching, into rotary motion/force through the unique dual con rod mechanism (rocker – connecting rod – crank) to possibly generate electric power through an electricity generator. Additionally, in a more advanced stadium, for optimal operation, intelligent control could be applied to enable the system to automatically adjust to different conditions, e.g. flow velocity and direction.

Bibliography

[1] Mulder, „Towards the Understanding of Flapping Wing Propulsion," University of Twente, Enschede, 2013.

[2] Jonker, Aarts en Meijaard, Flexible multibody dynamics for (control) design purposes, Enschede: Universiteit Twente, 2013.

[3] R. G. K. M. Aarts, J. P. Meijaard en J. B. Jonker, „SPACAR User Manual," University of Twente, Enschede, 2011.

[4] C. Kevin, „Modeling, Analysis, & Control of Compliantly coupled systems," Rensselaer Polytechnic Institute, NY, 2007.

[5] T. M, „MULTIVARIABLE CONTROL," University of Newcastle upon Tyne, Newcastle, 1999.

[6] J. van Dijk en R. Aarts, „Analytical one parameter method for PID motion controller settings," *IFAC Conference on Advances in PID Control,* p. WeC2.4, 2012.

[7] E. Grassi, K. S. Tsakalis, S. Dash, S. V. Gaikwad, W. MacArthur en G. Stein, „Integrated System Identification and PID Controller Tuning by Frequency Loop-Shaping," *IEEE TRANSACTIONS ON CONTROL SYSTEMS TECHNOLOGY,* vol. 9, nr. 2, pp. 285-294, 2001.

[8] J. van Dijk, MOTION AND VIBRATION CONTROL, ENSCHEDE: University of Twente, 2013.

[9] i. NORTHWEST foam products, „NORTHWEST foam products, inc.," [Online]. Available: http://northwestfoam.com/fact-specs.htm.

[10] Hofstede, Meewis, Stolk en Kros, Machineonderdelen constructie elementen uit de werktuigbouw, Dordrecht: Morks drukkerij en uitgeverij N.V., 1972.

[11] R. L. Mott, Machineonderdelen, Amsterdam: Pearson Education Benelux, 2010.

[12] MAXON, *Maxon Complete Catalog,* 2010.

[13] K. Craig, *Optical Encoders,* Rensselaer: Rensselaer Polytechnic Institute, 2007.

[14] J. P. Khatait, D. M. Brouwer, H. M. Soemers, R. M. Aarts en J. L. Herder, „Design of an Experimental Set-Up to Study the Behavior of a Flexible Surgical Instrument Inside an Endoscope," *Journal of Medical Devices,* vol. 7, pp. 1-12, 2013.

[15] R. G. K. M. Aarts, SYSTEM IDENTIFICATION AND PARAMETER ESTIMATION, Enschede: University of Twente, 2013.

[16] Elmo, *Composer User Manual for SimplIQ Servo Drives,* Westford: Elmo Motion Control Inc., 2007.

[17] Elmo, *DC Whistle Digital Servo Drive Installation Guide,* VS-Villingen: Elmo Motion Control Ltd, 2014.

[18] Elmo, *SimplIQ Command Reference Manual,* Villingen-Schwenningen: ELmo Motion Control, 2010.

[19] Elmo, *SimplIQ Software Manual,* Elmo Motion Control Ltd.: Villingen-Schwenningen, 2011.

[20] 20-minitune-Tune-up, „Cascaded position-velocity loops," *PT Design,* 2000.

Appendix 1 Model Development

1.1 Kinematic and dynamic analysis for a simplified 2D mechanism of the setup

For illustration of the theory discussed in section 2.1, in the following, a simple 2D model of the wing mechanism is developed considering the wing to be rigid.

Simplified mechanism with rigid wing

As Figure 45 illustrates, the actual mechanism is represented by three rigid beams (1, 2 and 3) and the wing is also represented by a rigid beam (4). The mechanism is supported in nodes $\vec{1}$ and $\vec{4}$ in both the x- and y-direction. The mechanism is actuated through the rotational node ϕ_1 of beam 1. The beams are connected to each other in the translational coordinates (x and y) but not in the rotational coordinates (ϕ) except for beam 3 and beam 4 (wing) which share the same rotational coordinate ϕ_6 in node $\vec{4}$.

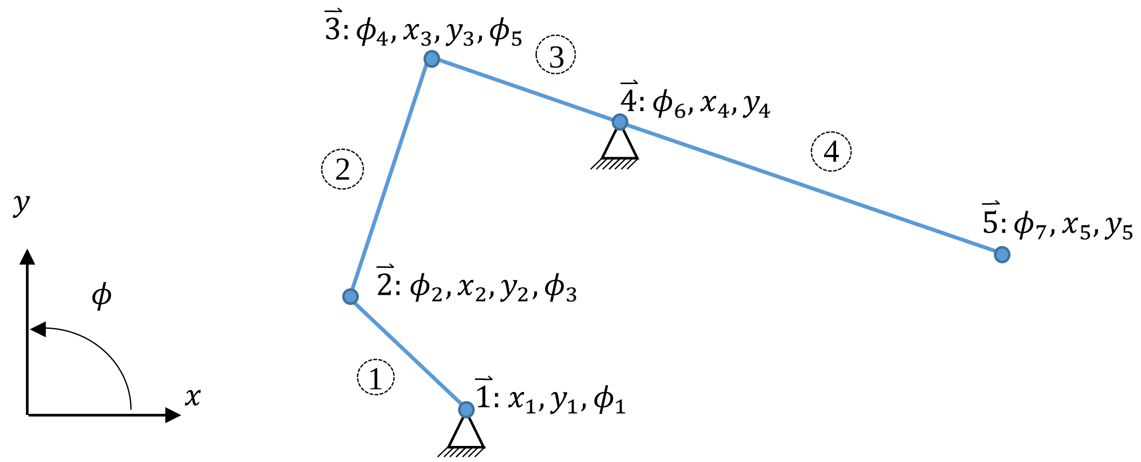

Figure 45 simplified mechanism with rigid wing

From this configuration the following applies:
For the nodal coordinates applies:

64

$$x = \left[\left[x^{(o)}\right]^T \quad \left[x^{(c)}\right]^T \quad \left[x^{(m)}\right]^T\right] =$$
$$[[x_1 \quad y_1 \quad x_4 \quad y_4]^T \quad [x_2 \quad y_2 \quad \phi_2 \quad \phi_3 \quad x_3 \quad y_3 \quad \phi_4 \quad \phi_5 \quad \phi_6 \quad x_5 \quad y_5 \quad \phi_7]^T \quad [\phi_1]^T]$$

For the deformation coordinates applies:

65 $$\varepsilon = \begin{bmatrix} \left[\varepsilon^{(o)}\right] \\ \left[\varepsilon^{(m)}\right] \\ \left[\varepsilon^{(c)}\right] \end{bmatrix} = \begin{bmatrix} \left[D(x)^{(o)}\right] \\ \left[D(x)^{(m)}\right] \\ \left[D(x)^{(c)}\right] \end{bmatrix} = \begin{bmatrix} \begin{bmatrix} \varepsilon_{1e} \\ \varepsilon_{1b1} \\ \varepsilon_{1b2} \\ \varepsilon_{2e} \\ \varepsilon_{2b1} \\ \varepsilon_{2b2} \\ \varepsilon_{3e} \\ \varepsilon_{3b1} \\ \varepsilon_{3b2} \\ \varepsilon_{4e} \\ \varepsilon_{4b1} \\ \varepsilon_{4b2} \end{bmatrix} \\ [\emptyset] \\ [\emptyset] \end{bmatrix} = \begin{bmatrix} \begin{bmatrix} \sqrt{((x_2 - x_1)^2 + (y_2 - y_1)^2)} - lo_1 \\ (sin(\phi_1))(x_2 - x_1) - (cos(\phi_1))(y_2 - y_1) \\ -(sin(\phi_2))(x_2 - x_1) + (cos(\phi_2))(y_2 - y_1) \\ \sqrt{((x_3 - x_2)^2 + (y_3 - y_2)^2)} - lo_2 \\ (sin(\phi_3))(x_3 - x_2) - (cos(\phi_3))(y_3 - y_2) \\ -(sin(\phi_4))(x_3 - x_2) + (cos(\phi_4))(y_3 - y_2) \\ \sqrt{((x_4 - x_3)^2 + (y_4 - y_3)^2)} - lo_3 \\ (sin(\phi_5))(x_4 - x_3) - (cos(\phi_5))(y_4 - y_3) \\ -(sin(\phi_6))(x_4 - x_3) + (cos(\phi_6))(y_4 - y_3) \\ \sqrt{((x_5 - x_4)^2 + (y_5 - y_4)^2)} - lo_4 \\ (sin(\phi_6))(x_5 - x_4) - (cos(\phi_6))(y_5 - y_4) \\ -(sin(\phi_7))(x_5 - x_4) + (cos(\phi_7))(y_5 - y_4) \end{bmatrix} \\ [\emptyset] \\ [\emptyset] \end{bmatrix}$$

With lo_1, lo_2, lo_3 and lo_4 the lengths of beam 1, 2, 3 and 4 respectively.

By applying eq. 17 it follows that there are 12 unknowns and 12 equations, hence the system is kinematically determinate. The system has one degree of freedom, namely ϕ_1.

Then, from eq. 10 the first order geometric transfer functions are derived:

$$F_{,q} = \begin{bmatrix} 0 \\ 0 \\ 0 \\ 0 \\ y_1 - y_2 \\ x_2 - x_1 \\ 1 \\ 1 - \frac{x_1y_3 - x_3y_1 - x_1y_4 + x_4y_1 + x_3y_4 - x_4y_3}{x_2y_3 - x_3y_2 - x_2y_4 + x_4y_2 + x_3y_4 - x_4y_3} \\ -\frac{(y_3 - y_4)(x_1y_2 - x_2y_1 - x_1y_3 + x_3y_1 + x_2y_3 - x_3y_2)}{x_2y_3 - x_3y_2 - x_2y_4 + x_4y_2 + x_3y_4 - x_4y_3} \\ \frac{(x_3 - x_4)(x_1y_2 - x_2y_1 - x_1y_3 + x_3y_1 + x_2y_3 - x_3y_2)}{x_2y_3 - x_3y_2 - x_2y_4 + x_4y_2 + x_3y_4 - x_4y_3} \\ 1 - \frac{x_1y_3 - x_3y_1 - x_1y_4 + x_4y_1 + x_3y_4 - x_4y_3}{x_2y_3 - x_3y_2 - x_2y_4 + x_4y_2 + x_3y_4 - x_4y_3} \\ \frac{x_1y_2 - x_2y_1 - x_1y_3 + x_3y_1 + x_2y_3 - x_3y_2}{x_2y_3 - x_3y_2 - x_2y_4 + x_4y_2 + x_3y_4 - x_4y_3} \\ \frac{x_1y_2 - x_2y_1 - x_1y_3 + x_3y_1 + x_2y_3 - x_3y_2}{x_2y_3 - x_3y_2 - x_2y_4 + x_4y_2 + x_3y_4 - x_4y_3} \\ \frac{(y_4 - y_5)(x_1y_2 - x_2y_1 - x_1y_3 + x_3y_1 + x_2y_3 - x_3y_2)}{x_2y_3 - x_3y_2 - x_2y_4 + x_4y_2 + x_3y_4 - x_4y_3} \\ -\frac{(x_4 - x_5)(x_1y_2 - x_2y_1 - x_1y_3 + x_3y_1 + x_2y_3 - x_3y_2)}{x_2y_3 - x_3y_2 - x_2y_4 + x_4y_2 + x_3y_4 - x_4y_3} \\ \frac{x_1y_2 - x_2y_1 - x_1y_3 + x_3y_1 + x_2y_3 - x_3y_2}{x_2y_3 - x_3y_2 - x_2y_4 + x_4y_2 + x_3y_4 - x_4y_3} \\ 1 \end{bmatrix} \tag{66}$$

$$E_{,q} = [0 \quad 0 \quad 0 \quad 0 \quad 0 \quad 0 \quad 0 \quad 0 \quad 0 \quad 0 \quad 0 \quad 0]^T \tag{67}$$

From eq. 13 the second order geometric transfer functions are derived:

68 $$F_{,qq} =$$

$$\begin{bmatrix} 0 \\ 0 \\ 0 \\ 0 \\ -dx_1 \\ -dy_1 \\ 0 \\ \frac{dx_1dx_3+dy_1dy_3}{dx_2dy_3-dx_3dy_2}+\frac{lo_3^2(dx_1dy_2-dx_2dy_1)^2}{(dx_2dy_3-dx_3dy_2)^3}+\frac{(dx_2dx_3+dy_2dy_3)(dx_1dy_3-dx_3dy_1)^2}{(dx_2dy_3-dx_3dy_2)^3} \\ \frac{-dy_3(dx_1dx_2+dy_1dy_2)}{dx_2dy_3-dx_3dy_2}-\frac{lo_3^2dy_2(dx_1dy_2-dx_2dy_1)^2}{(dx_2dy_3-dx_3dy_2)^3}-\frac{lo_2^2dy_3(dx_1dy_3-dx_3dy_1)^2}{(dx_2dy_3-dx_3dy_2)^3} \\ \frac{dy_3(dx_1dx_2+dy_1dy_2)}{dx_2dy_3-dx_3dy_2}+\frac{lo_3^2dy_2(dx_1dy_2-dx_2dy_1)^2}{(dx_2dy_3-dx_3dy_2)^3}+\frac{lo_2^2dy_3(dx_1dy_3-dx_3dy_1)^2}{(dx_2dy_3-dx_3dy_2)^3} \\ \frac{dx_1dx_3+dy_1dy_3}{dx_2dy_3-dx_3dy_2}+\frac{lo_3^2(dx_1dy_2-dx_2dy_1)^2}{(dx_2dy_3-dx_3dy_2)^3}+\frac{(dx_2dx_3+dy_2dy_3)(dx_1dy_3-dx_3dy_1)^2}{(dx_2dy_3-dx_3dy_2)^3} \\ -\frac{dx_1dx_2+dy_1dy_2}{dx_2dy_3-dx_3dy_2}-\frac{lo_2^2(dx_1dy_3-dx_3dy_1)^2}{(dx_2dy_3-dx_3dy_2)^3}-\frac{(dx_1dy_2-dx_2dy_1)^2(dx_2dx_3+dy_2dy_3)}{(dx_2dy_3-dx_3dy_2)^3} \\ -\frac{dx_1dx_2+dy_1dy_2}{dx_2dy_3-dx_3dy_2}-\frac{lo_2^2(dx_1dy_3-dx_3dy_1)^2}{(dx_2dy_3-dx_3dy_2)^3}-\frac{(dx_1dy_2-dx_2dy_1)^2(dx_2dx_3+dy_2dy_3)}{(dx_2dy_3-dx_3dy_2)^3} \\ \frac{-lo_4^2dx_3(dx_1dy_2-dx_2dy_1)^2}{(dx_2dy_3-dx_3dy_2)^2(dx_3dx_4+dy_3dy_4)}+\frac{dy_4(dx_1dy_2-dx_2dy_1)^2(dx_2dx_3+dy_2dy_3)}{(dx_2dy_3-dx_3dy_2)^3}+\frac{lo_2dy_4(dx_1dy_3-dx_3dy_1)^2}{(dx_2dy_3-dx_3dy_2)^3}+\frac{dy_4(dx_1dx_2+dy_1dy_2)}{dx_2dy_3-dx_3dy_2}+\frac{dy_4(dx_1dy_2-dx_2dy_1)^2(-dx_4dy_3+dx_3dy_4)}{(dx_2dy_3-dx_3dy_2)^2(dx_3dx_4+dy_3dy_4)} \\ -\frac{dx_4(dx_1dx_2+dy_1dy_2)}{dx_2dy_3-dx_3dy_2}-\frac{dx_4(dx_1dy_2-dx_2dy_1)^2(dx_2dx_3+dy_2dy_3)}{(dx_2dy_3-dx_3dy_2)^3}-\frac{lo_2^2dx_4(dx_1dy_3-dx_3dy_1)^2}{(dx_2dy_3-dx_3dy_2)^3}-\frac{lo_4^2dy_3(dx_1dy_2-dx_2dy_1)^2}{(dx_2dy_3-dx_3dy_2)^2(dx_3dx_4+dy_3dy_4)}-\frac{dx_4(dx_1dy_2-dx_2dy_1)^2(-dx_4dy_3+dx_3dy_4)}{(dx_2dy_3-dx_3dy_2)^2*(dx_3dx_4+dy_3dy_4)} \\ -\frac{dx_1dx_2+dy_1dy_2}{dx_2dy_3-dx_3dy_2}-\frac{lo_2^2(dx_1dy_3-dx_3dy_1)^2}{(dx_2dy_3-dx_3dy_2)^3}-\frac{(dx_1dy_2-dx_2dy_1)^2(dx_2dx_3+dy_2dy_3)}{(dx_2dy_3-dx_3dy_2)^3} \\ 0 \end{bmatrix}$$

69 $E_{,qq} = [0 \quad 0 \quad 0 \quad 0 \quad 0 \quad 0 \quad 0 \quad 0 \quad 0 \quad 0 \quad 0 \quad 0]^T$

Whereby:
$dx_1 = x_2 - x_1$
$dy_1 = y_2 - y_1$
$dx_2 = x_3 - x_2$
$dy_2 = y_3 - y_2$
$dx_3 = x_4 - x_3$
$dy_3 = y_4 - y_3$
$dx_4 = x_5 - x_4$
$dy_4 = y_5 - y_4$

Now the velocities and accelerations can be determined through equations 6 and 7 and the position can be determined iteratively (see eq.14). Also, either forward or inverse dynamic analysis could be applied using the equations of motion (eq.15).

Simplified mechanism with flexible wing
For the mechanism with flexible wing, the same configuration as presented in Figure 45 applies. Hence for the nodal coordinates the same applies:

70

$$x = \left[\left[x^{(o)}\right]^T \quad \left[x^{(c)}\right]^T \quad \left[x^{(m)}\right]^T\right] =$$
$$[[x_1 \quad y_1 \quad x_4 \quad y_4]^T \quad [x_2 \quad y_2 \quad \phi_2 \quad \phi_3 \quad x_3 \quad y_3 \quad \phi_4 \quad \phi_5 \quad \phi_6 \quad x_5 \quad y_5 \quad \phi_7]^T \quad [\phi_1]^T]$$

However, now the deformation of the wing is not negligible. Hence for the deformation coordinates now applies:

71 $$\varepsilon = \begin{bmatrix} \left[\varepsilon^{(o)}\right] \\ \left[\varepsilon^{(m)}\right] \\ \left[\varepsilon^{(c)}\right] \end{bmatrix} = \begin{bmatrix} \left[D(x)^{(o)}\right] \\ \left[D(x)^{(m)}\right] \\ \left[D(x)^{(c)}\right] \end{bmatrix} =$$
$$[[\varepsilon_{1e} \quad \varepsilon_{1b1} \quad \varepsilon_{1b2} \quad \varepsilon_{2e} \quad \varepsilon_{2b1} \quad \varepsilon_{2b2} \quad \varepsilon_{3e} \quad \varepsilon_{3b1} \quad \varepsilon_{3b2}]^T \quad [\varepsilon_{4e} \quad \varepsilon_{4b1} \quad \varepsilon_{4b2}]^T \quad [\emptyset]^T]$$

By applying eq. 17 it follows that there are 12 unknowns and 12 equations, hence the system is kinematically determinate. The system has four degrees of freedom, namely ϕ_1, ε_{4e}, ε_{4b1} and ε_{4b2}. With this regard, the equations for the geometric transfer functions are omitted as these would lead to too bulky equations.

Extension to 3D configuration
Here, the model is extended to a 2DOF 3D configuration. The degrees of freedom are indicated in the figure by the red arrows. Wing stiffness is modeled through a torsional spring (see the red colored element in Figure 46). In contrast to the 2D configuration, in the 3D configuration system/element orientation is described by means of Euler parameters instead of angles. For more detail on this see [3] and [2].

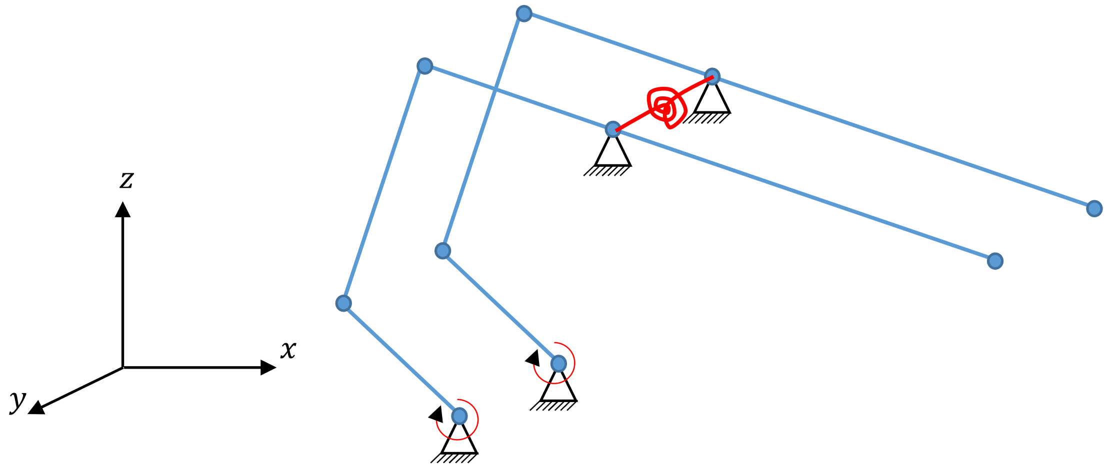

Figure 46 3D configuration of the mechanism

1.2 Mass and equivalent mass calculation

Mass

The system mass is calculated in Spacar:

Mass of the mechanism: $m_m = 0.0183$ [kg]
Mass of the wing: $m_w = 0.07$ [kg]
Mass experienced by one servo-motor (in decoupled configuration): $m = \frac{1}{2}m_m + \frac{1}{2}m_w = 0.0441[\text{kg}]$

Equivalent mass

As illustrated in [6], instead of using equation45, the equivalent mass m_{eq} can be estimated from the high frequency (high order) part of the plant for a closer approximation with the more elaborate Spacar model:

72 $$G_{HF} = \frac{1}{m_{eq}s^2}$$

And therefor, from the linearized Spacar model, the following applies for m_{eq}:

73 $$m_{eq} = \frac{1}{G_{HF} \cdot \omega^2} = 0.0026[\frac{s^2}{rad^2}]$$

1.3 Wing stiffness estimation and measurement

Objective

For a reliable approximation of the coupling between the two (servo) motors, presumably caused by the torsional stiffness between the pins of the wing when in phase shift, the torsional stiffness k_t between the pins is estimated (in SolidWorks) and measured. Also, the longitudinal stiffness k (used for the simplified model) is determined from the low frequency natural frequency ω_n obtained from the linearized Spacar model.

1.3.1 Estimation

Wing stiffness

The wing material is EPS (Expanded polystyrene) Foam and has the following properties [9]:

Elastic Modulus: $2.21\ [\mathrm{MPa}]$
Shear Modulus: $3.17\ [\mathrm{MPa}]$
Mass Density: $21.6\ [\frac{\mathrm{kg}}{\mathrm{m}^3}]$
Tensile Strength: $0.12\ [\mathrm{MPa}]$
Compressive Strength: $0.1\ [\mathrm{MPa}]$
Yield Strength: $0.18\ [\mathrm{Mpa}]$

The wing stiffness is estimated in SolidWorks:

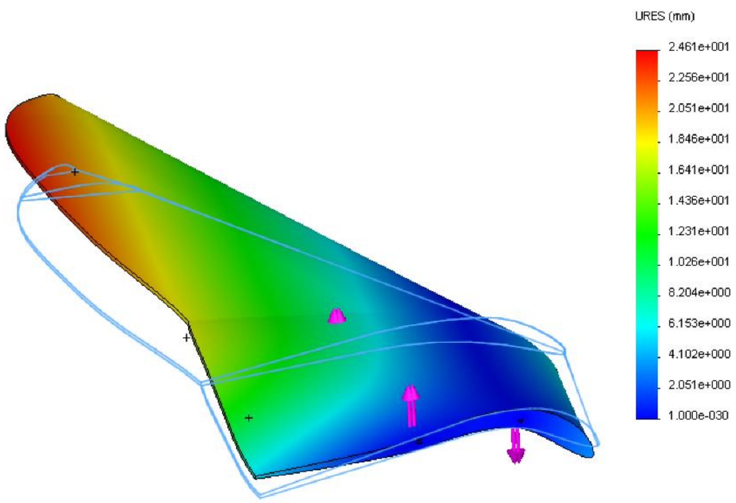

Figure 47Wing stiffness estimation

On each pin an average force $F = 1\ [\mathrm{N}]$ is applied at a distance of $0.07\ [\mathrm{m}]$ causing a total torque of $T = 2 \cdot 1[\mathrm{N}] \cdot 0.07[\mathrm{m}] = 0.14[\mathrm{Nm}]$. This load caused a deflection of $\alpha = 0.06\ [\mathrm{rad}] = 3.34°$. This is estimated as follows:
Pin displacement measured at approximately COM (center of mass: $d_x = 0.2\ [\mathrm{m}]$):

For pin1: $d_{y1} = 0.002[\mathrm{m}]$
For pin2: $d_{y2} = 0.010[\mathrm{m}]$
Between the two pins: $d_y = d_{y1} + d_{y2} = 0.0120[\mathrm{m}]$

Pin deflection determined at approximately COM:

For pin1: $\alpha_1 \ = \ 2 \cdot \text{atan}\left(\frac{d_{y1}}{2 \cdot d_x}\right) = 0.01 \ [\text{rad}]$
For pin2: $\alpha_2 \ = \ 2 \cdot \text{atan}\left(\frac{d_{y2}}{2 \cdot dx}\right) = 0.05[\text{rad}]$
Between the two pins: $\alpha \ = \alpha_1 + \alpha_2 = 0.06 \ [\text{rad}]$

Hence the stiffness between the pins is estimated as follows:

Torsional stiffness:

74 $$k_t = \frac{T}{\alpha} = 2.33[\text{Nm/rad}]$$

1.3.2 Measurement

Measuring area

Previous to doing the measurements there is investigated in what range the (torque causing) phase shift between the pins varies. With a phase shift of 0.1222[rad] (7°) between the motors, the connecting rod mechanism establishes a varying phase shift between the wing pins as illustrated in Figure 48 (simulation retrieved from the Spacar model). From this can be deduced that the maximum occurring phase shift between the wing pins is 0.0826 [rad] (4.73°). Hence, the measurements are focused around this value, i.e. measurements are done between 0° and 7.3°.

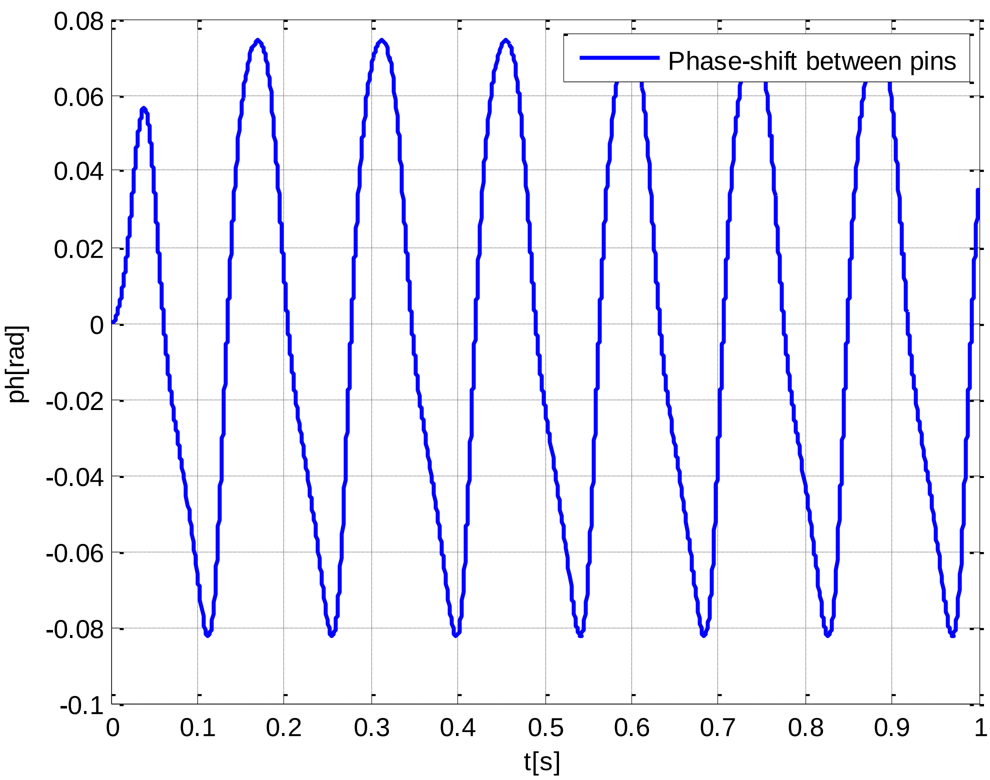

Figure 48 Phase shift between the pins of the wing

Measurement method

As the schematic of the test setup illustrates (Figure 49), in order to determine the torsional stiffness k_t, one pin is fixed completely and the other is left free to rotate. The free pin is loaded with a mass m which is measured by means of a spring balance and its displacement x is measured through a dial indicator. In this way, the torsional stiffness is determined as follows:

First the torque T and deflection α are determined through measurement of m and x respectively:

75 $\quad T = \cos(\alpha) \cdot m \cdot g \cdot r = m \cdot g \cdot r$ (Considering $\cos(\alpha) \approx 1\ for\ 0° \leq \alpha \leq 7.3°$)

76 $\quad \alpha = \text{atan}\left(\frac{x}{l}\right)$

With:

$g = 9.87 \left[\frac{\mathrm{m}}{\mathrm{s}^2}\right]$ = Gravitational acceleration
r = moment arm (see Figure 49)
l = distance where x is measured

Finally k_t is determined as follows:

77 $\quad k_t = \frac{T}{\alpha}$

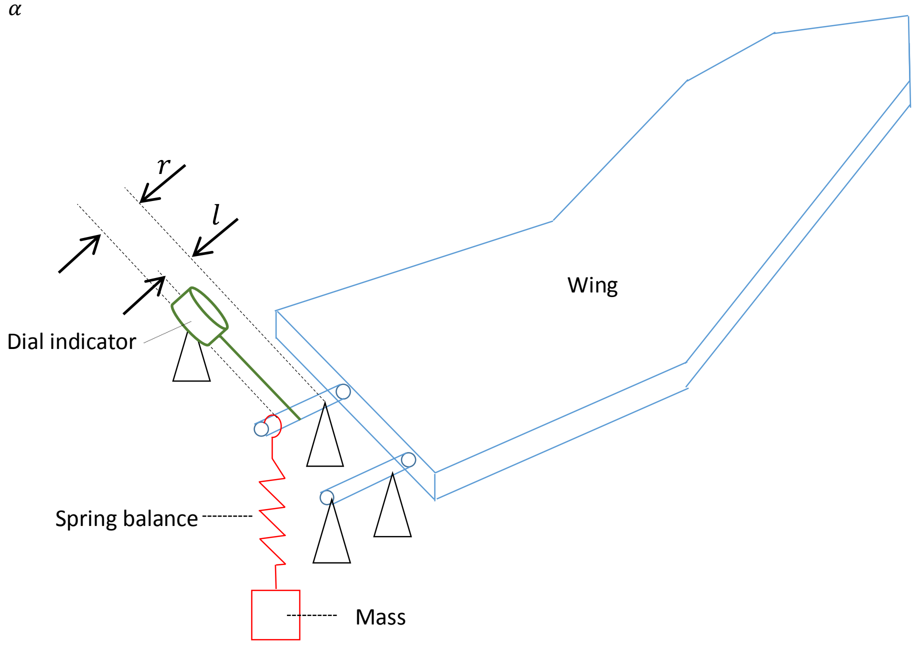

Figure 49 Schematic of the test setup

Error calculations
The error transmitted to the calculated torsional stiffness k_t due to the measurements is calculated as presented in the following:

First the transmitted error dT to the torque is calculated as follows:

78 $\quad dT = \left(\left(\frac{\delta T}{\delta m} dm\right)^2 + \left(\frac{\delta T}{\delta r} dr\right)^2\right)^{\frac{1}{2}} = ((g \cdot r \cdot dm)^2 + (m \cdot g \cdot dr)^2)^{\frac{1}{2}}$

With:

dm = the measurement error of m
dr = the measurement error of r

Next the transmitted error $d\alpha$ to the deflection if calculated as follows:

79 $$d\alpha = \left(\left(\frac{\delta\alpha}{\delta x}dx\right)^2 + \left(\frac{\delta\alpha}{\delta l}dl\right)^2\right)^{\frac{1}{2}} = \left(\left(\frac{1}{l\left(1+\left(\frac{x}{l}\right)^2\right)}dx\right)^2 + \left(\frac{-x}{l^2\left(1+\left(\frac{x}{l}\right)^2\right)}dl\right)^2\right)^{\frac{1}{2}}$$

With:

dx = the measurement error of x
dl = the measurement error of l

Finally the transmitted error to the torsional stiffness is calculated as follows:

80 $$dk_t = \left(\left(\frac{\delta k_t}{\delta T}dT\right)^2 + \left(\frac{\delta k_t}{\delta\alpha}d\alpha\right)^2\right)^{\frac{1}{2}} = \left(\left(\frac{1}{\alpha}dT\right)^2 + \left(-\frac{T}{\alpha^2}d\alpha\right)^2\right)^{\frac{1}{2}}$$

Test setup
The accuracy of the measurements depends on the equipment used in the actual setup, see Figure 50:

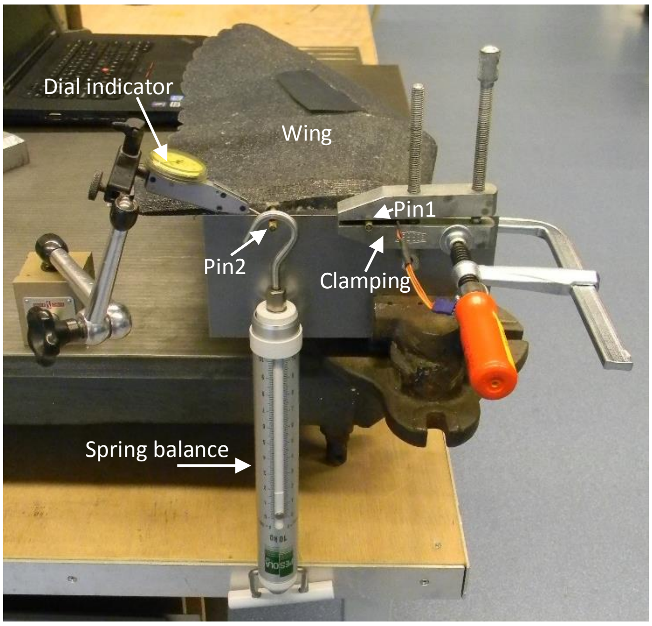

Figure 50 Actual test setup for measurement of the torsional stiffness k_t between the wing pins

Equipment
The following equipment is used:

1. *Dial indicator*: for measurement of the displacement x a dial indicator with a range of 1[mm] and a scaling of 0.01 [mm]. The reading accuracy is taken to be half the scaling, i.e. $\frac{1}{2}\cdot 0.01[\mathrm{mm}]$. For the measurement error in x there is taken half of the reading accuracy, i.e. $dx = \frac{1}{2}\cdot\frac{1}{2}\cdot 0.01[\mathrm{mm}] = \frac{1}{2}\cdot\frac{1}{2}\cdot 10^{-5}[\mathrm{m}] = 2.5\cdot 10^{-6}[\mathrm{m}]$.
2. *Spring balance*: for measurement of the load mass m a spring balance with a range of 10[kg] and a scaling of 0.1 [kg]. The reading accuracy is taken to be a quarter of the scaling, i.e. $\frac{1}{4}\cdot$

$0.1[\mathrm{kg}]$. Hence for the measurement error in m there is taken half of the reading accuracy, i.e. $dm = \frac{1}{2} \cdot \frac{1}{4} \cdot 0.1[\mathrm{kg}] = 1.25 \cdot 10^{-2}[\mathrm{kg}]$.

3. *Caliper*: for measurement of the distances l and r a caliper with a scaling of 0.05 [mm]. The reading accuracy is taken to be half the scaling, i.e. $\frac{1}{2} \cdot 0.05[\mathrm{mm}]$. Hence for the measurement error in l and r there is taken half of the reading accuracy, i.e. $dl = dr = \frac{1}{2} \cdot \frac{1}{2} \cdot 0.05[\mathrm{mm}] = \frac{1}{2} \cdot \frac{1}{2} \cdot 5 \cdot 10^{-5}[\mathrm{m}] = 1.25 \cdot 10^{-5}[\mathrm{m}]$.

Results

Various loads m are applied on a constant arm $r = 0.01465$ [m] and the respective displacements x are measured at the constant distance $l = 0.0072[\mathrm{m}]$. With equations75, 76 and 77 the torque T, deflection α and torsional stiffness k_t are calculated respectively and with equations78, 79 and 80 their corresponding transmitted errors are calculated respectively using the measurement errors mentioned above (see the section on equipment). The results are presented in Figure 51 by plotting the torque T against the deflection α and including their error bars. The average torsional stiffness is calculated to be $k_t = 3.11 \pm 0.05$ [Nm/rad]. However, assuming a linear relation between T and α, the torsional stiffness is estimated in excel, through a least square approximation, to be $k_t = 3.35[\mathrm{Nm/rad}]$ (see the equation on the plot).

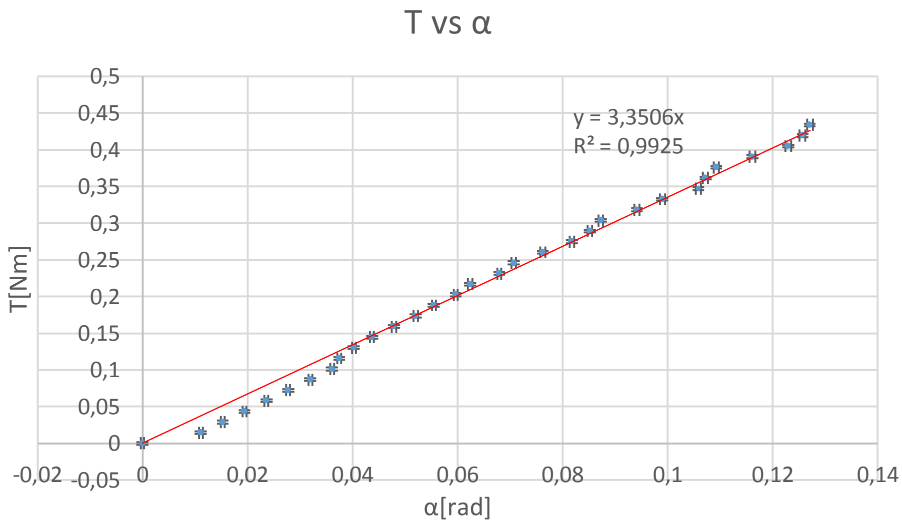

Figure 51 Results: Torque vs deflection including error bars

Comparing the estimated torsional stiffness $k_t = 2.33$ [Nm/rad] with the measured one $k_t = 3.35$ [Nm/rad], they differ by 30%. This is most likely caused by glue and reinforcements on the actual wing which caused the increase in stiffness. For further calculations the measured torsional stiffness of $k_t = 3.35$ [Nm/rad] is used.

1.3.3 Longitudinal stiffness k for simplified model

The longitudinal stiffness used in the simplified model is calculated from the low frequency resonance (also see Appendix 6):

81 $$k = \omega_n^2 \cdot m$$

With $\omega_n = \omega_{R_{\text{low}}} = 0.95\ [\text{Hz}] = 6[\text{rad/s}]$ (see Figure 5) and $m = 0.0441[\text{kg}]$ (see section 1.2) this yields the following value for the longitudinal stiffness:

$k = 1.6\ [\text{N/m}]$

Appendix 2 PID control on linearized plant

The PID controlled linearized system gives results depicted below. From these results (especially Figure 54) it is clear that for the controlled linearized system the phase shift of $phs = 7° = 0.1222[\text{rad}]$ is reached with an accuracy of $e_{max} = \pm 0.1° = \pm 0.0017[\text{rad}]$ for a flapping frequency of $f = 7\ [\text{Hz}]$.

System output:

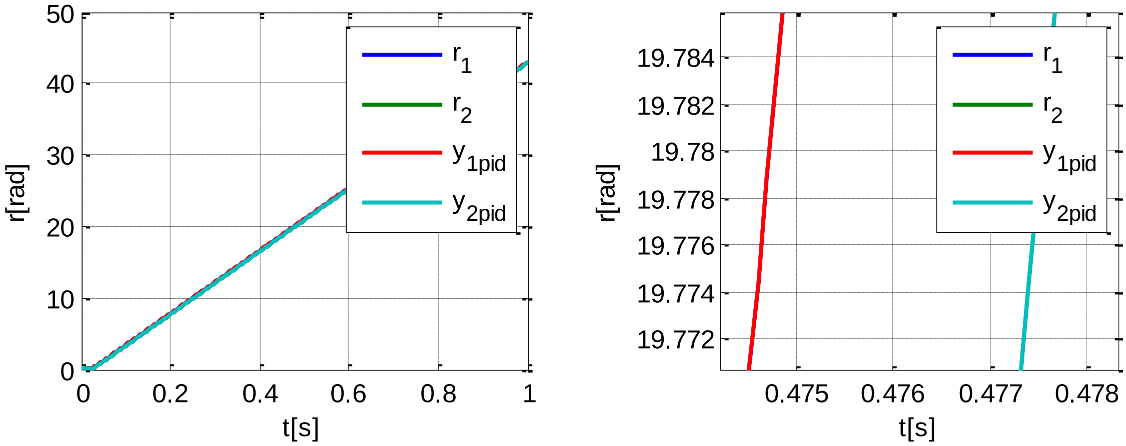

Figure 52 System output of controlled linearized system; Right: Zoomed in

Servo error:

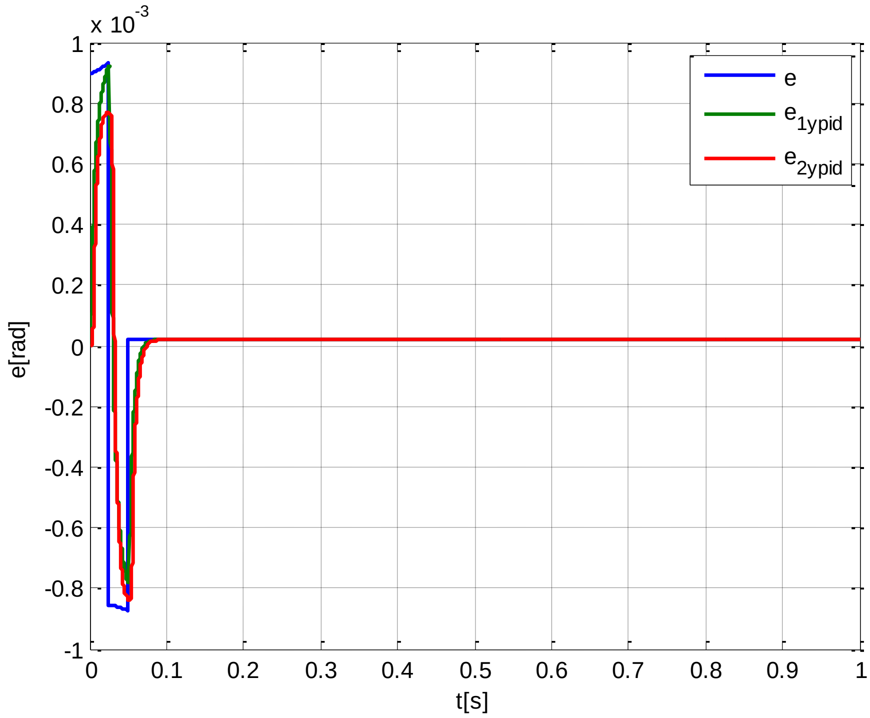

Figure 53 Servo error of controlled linearized system

Phase shift:

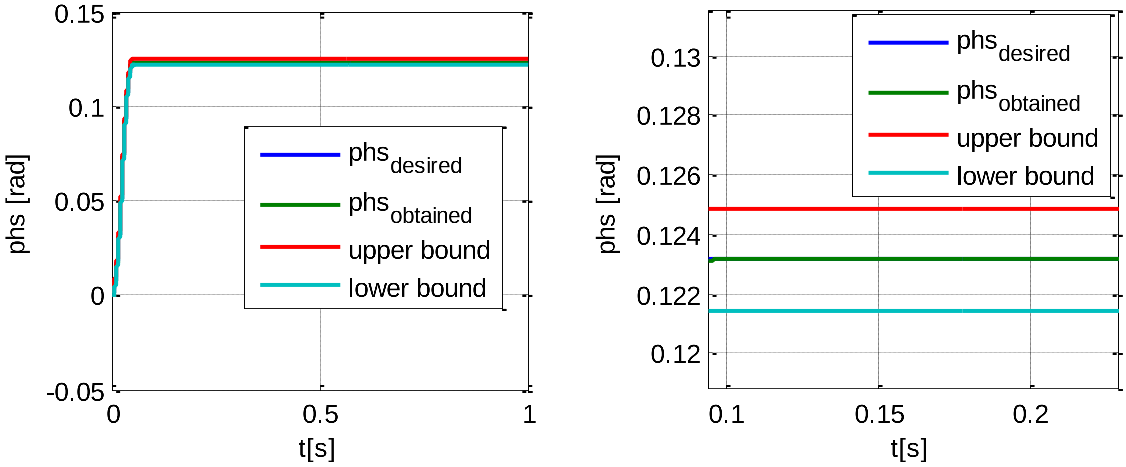

Figure 54 Phase shift of controlled linearized system; Right: Zoomed in

Appendix 3 Approximation of aerodynamic forces on Robird

3.1 Flapping wing kinematics

Taking a single two dimensional (2D) wing section, the flapping wing kinematics of a bird are described by two motions occurring simultaneously, namely plunging and pitching see equations 82 and 83 respectively (see Figure 55). This combined motion is determinative for the wing angle of attack.

82 $h(t) = h_0 c sin(\omega t)$
83 $\theta(t) = \theta_0 \sin(\omega t + \varphi)$

Whereby:
$h(t)$ = the vertical position at time t
h_0 = the plunging amplitude non-dimensionalised by the airfoil chord length c
$\theta(t)$ = is the pitching angle with respect to the horizon at time t
θ_0 = the pitching amplitude of the motion
$\omega = 2\pi f$ = the radial frequency of the motion
f = the flapping frequency
φ = the phase difference between the plunging and pitching motion. In most cases the pitch is leading the plunge with 90°.

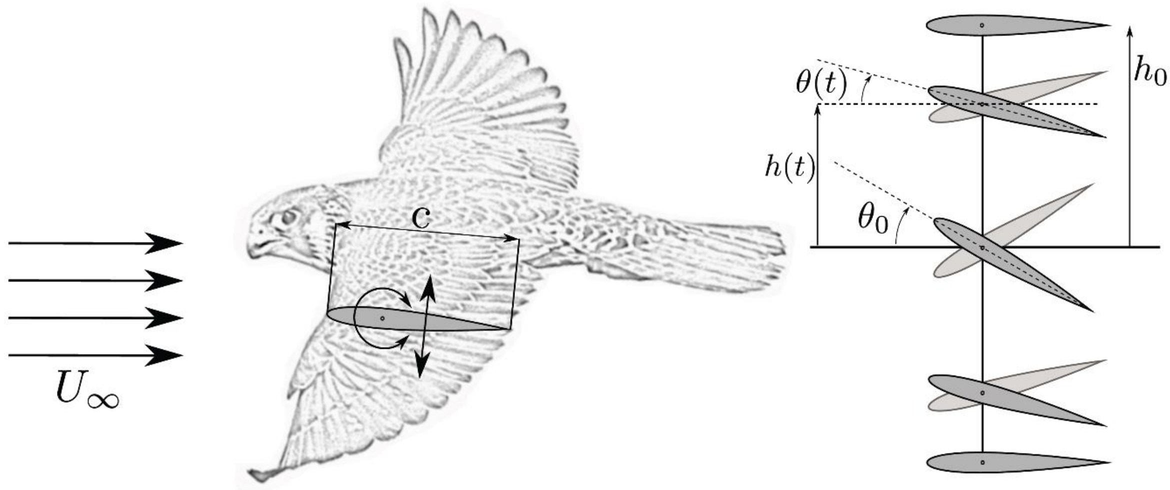

Figure 55 Left: Flapping wing motion of a bird; Right: 2D pitching and plunging rigid airfoil section [1]

3.2 Flapping propulsion

Below there is attempted to describe flapping propulsion (relevant for Robird wing aerodynamics) in four steps:

- **Formation of a reverse von Karman street**: When the flapping wing motion brings about a large enough Strouhal number there occurs a formation of a reverse von Karman vortex street.
- **Formation of leading edge vortices**: This occurs in combination with the formation of leading edge vortices (LEV's) due to dynamic stall. Strong LEV's contribute to a strong reverse von Karman street in the wake of the airfoil. The development and strength of the LEV's is strongly influenced by the maximum effective angle of attack during the motion.
- **Thrust production**: The reverse von Karman street in the wake causes thrust-production.

- **Formation of a jet-like stream wise velocity profile**: In the thrust-producing wake, the air is accelerated in between the vortices, which yields time-averaged a jet-like stream wise velocity profile. The strength of this jet is a measure for the thrust produced.

The influence of the Strouhal number on flapping propulsion
The Strouhal number is defined as follows:

84 $$St = \frac{fA}{U_\infty}$$

Whereby:

$A = 2h_0c$ = wake width
$f = \frac{\omega}{2\pi}$ = flapping frequency
U_∞ = free stream velocity

With:

c = cord length
h_0 = plunging amplitude
ω = radial frequency of the motion

The Strouhal number has the following influence on flapping propulsion:

- an increase in the Strouhal number causes
- an increase of the maximum effective angle of attack which causes
- stronger LEV's and therewith creating a
- stronger reverse von Karman street in the wake which then produces
- larger forces and
- a more pronounced stream wise jet profile behind the airfoil however with
- a lower thrust producing efficiency

The influence of the pitching angle
The pitching angle has the following influence on flapping propulsion:

- an increase in the pitching angle causes
- a decrease in the effective angle of attack causing
- milder LEV's which cause
- higher thrust producing efficiency (peak at $0.1 < St < 0.3$ which is close to the optimum Strouhal regime found in nature) but a
- lower cruise velocity

The maximum efficiency occurs every time for an effective angle of attack of around 11 degrees.

3.3 Robird wing aerodynamics
Robird wing aerodynamics:

- The root of the wing mainly provides lift
- The tip of the wing mainly provides thrust
- The mid-wing section creates a balances of thrust and lift production

From [1], it follows that the aerodynamic forces, thrust force F_t, lift force F_l and moment M, depend on the aerodynamic coefficients, thrust coefficient C_t, lift coefficient C_l and moment coefficient C_m respectively, and free stream velocity U_∞, free stream density ρ_∞ , the cord length c and the wing span b as follows:

85 $F_t \;= \frac{C_t U_\infty^2 S \rho_\infty}{2}$

86 $F_l \;= \frac{C_l U_\infty^2 S \rho_\infty}{2}$

87 $M \;= \frac{C_m U_\infty^2 S.\bar{c} \rho_\infty}{2}$

With:

88 $S = \bar{c} \cdot b$ = wing surface area

With:

89 $\bar{c} = \frac{(c_r + c_m + c_t)}{3}$

Whereby:

$c_r = 0.215$ [m] = cord length at the root
$c_m = 0.18$ [m] = cord length at the mid-section
$c_t = 0.14$ [m] = cord length at the tip

The following values are taken for the remaining parameters:

$\rho_\infty = 1.25\ [\frac{\mathrm{kg}}{\mathrm{m}^3}]$
$U_\infty = 10[\mathrm{m/s}]$
$b = \frac{1}{2} \cdot 1.1[\mathrm{m}]$ (Considering only one wing)

With the main focus on capturing the order of magnitude and the periodicity, the aerodynamic coefficients are extremely roughly approximated as follows:

90 $Ct = \overline{Ct} + A_{Ct} \cdot sin(\omega t)$

91 $Cl = \overline{Cl} + A_{Cl} \cdot sin(\omega t)$

92 $Cm = \overline{Cm} + A_{Cm} \cdot sin(\omega t)$

With:

$\omega = 44 \left[\frac{\mathrm{rad}}{\mathrm{s}}\right]$ the flapping frequency

The following parameters are estimated out of data from [1]:

$\overline{Ct} = 0.03$ = time-averaged drag for the mid-wing section near $U_\infty = 10[\mathrm{m/s}]$
$\overline{Cl} = 0.725$ = time-averaged lift for the mid-wing section near $U_\infty = 10[\mathrm{m/s}]$
$\overline{Cm} = 0.0625$ = time-averaged moment for the mid-wing section near $U_\infty = 10[\mathrm{m/s}]$
$A_{Ct} = 0.29$ = maximum amplitude w.r.t $\overline{Ct}$
$A_{Cl} = 0.425$ = maximum amplitude w.r.t $\overline{Cl}$
$A_{Cm} = 0.2875$ = maximum amplitude w.r.t $\overline{Cm}$

Then, after substituting equations $90, 91$ and 92 into 85, 86 and 87 respectively, the aerodynamic forces are supplied as disturbances with which the controller needs to cope.

Appendix 4 Mechanical design

In this section the mechanical design of the disc connection, gear connection and bearing is done.

4.1 Disc and bolt sizing

For the preload Q between the discs applies [10]:

93 $$Q = \frac{M}{f \cdot r}$$

With:
M = No slip torque
f = friction coefficient
r = disc radius

The following design choices are made:

- From the reaction torques (see Figure 64) it is clear that the torque does not exceed $M_{react} = 9$ [Nm], hence in order to prevent slipping of the mechanical connection, M is taken a factor $k = 1.5$ larger than M_{react} i.e.:

94 $$M = k \cdot M_{react}$$

  Hence in this case: $M = 1.5 \cdot 9 = 13.5[\text{Nm}]$

- The disc is chosen to be an aluminum disc ($f = 0.15$ for worst case; lubricated and greasy surfaces; see [11]) with a radius of $r = 0.015$ [m].

Applying this information to Eq 93 results into a required preload $Q = 6000[\text{N}] = 6$ [kN].

This preload is brought to by a bolt loaded axially. Then for this bolt applies [10]:

95 $$\sigma \geq k_a \frac{Q}{A} \Leftrightarrow A \geq k_a \frac{Q}{\sigma} \Leftrightarrow \pi r_b^2 \geq k_a \frac{Q}{\sigma} \Leftrightarrow r_b \geq \sqrt{\frac{k_a Q}{\sigma \pi}}$$

With:

$k_a = \frac{1}{0.75}$ = typical safety factor (see [11])
σ = allowable yield stress
A = bolt cross-sectional area
r_b = bolt radius

Considering a 6061-T6 aluminum bolt with $\sigma = 241[\text{Mpa}]$ a bolt radius of at least $r_b = 4[\text{mm}]$ is required. Hence, a M8 – 1.25 bolt with diameter $d = 8[\text{mm}]$ and thread pitch $p = 1.25$ [mm] is sufficient.

4.2 Gear sizing

In order to keep the motors outside the wind tunnel, the mechanism is elevated through extra gears (with a gear reduction $i = 1$). The gear design is based on gear tooth side damage as this is determinative for the gear dimensions (see [10]). Given a tooth width b and a pitch diameter d, first the modulus m is determined through a thumb rule and thereafter from that, the number of teeth z is determined. Finally checking calculations are done on the chosen gear.

The thumb rule used here is (see [10]):

96 $$m = \frac{b}{\lambda}$$

Hereby λ is a constant which constrains the extra forces which appear as a consequence of change in direction of the axis (see [10]).

Subsequently the number of teeth is calculated as follows:

97 $$z = \frac{d}{m}$$

Finally checking calculations are executed. First the maximum load per unit of the tooth width q_{max} is calculated (see [10]):

98 $$q_{max} = C_s q + q_D + q_R$$

With:

$C_s = 1$ = shock factor (a value of 1 is common for electro motors driving relatively small loads; see [10])
$q = \frac{M}{r \cdot b}$ = nominal circumferential force per unit of the tooth width
$q_D = \frac{F_D}{b}$ = dynamic circumferential force per unit of the tooth width
$F_D \approx C_s F \frac{v}{10}$ = dynamic circumferential force for $v \leq 6 \left[\frac{\mathrm{m}}{\mathrm{s}}\right]$
$q_R \approx 3\sqrt{b}$ = extra load due to direction errors (misalignment)
M = torsional moment
$r = \frac{d}{2}$ = pitch radius
$F = \frac{M}{r}$ = load
$v = \omega \cdot r$ = circumferential velocity on pitch circle
ω = angular velocity

With b and r in [mm], M in [N.mm] and v in [m/s] this results in a q_{max} in [N/mm] defined as:

99 $$q_{max} = C_s \left(\frac{M}{r \cdot b}\right)\left(1 + \frac{v}{10}\right) + 3\sqrt{b}$$

With m in [mm] the shear stress in the tooth feet $\sigma_{i_{max}}$ in [$\frac{\mathrm{N}}{\mathrm{mm}^2}$] is calculated as:

100 $$\sigma_{i_{max}} = C_\epsilon \cdot \mu \cdot \frac{q_{max}}{m}$$

With:

$C_\epsilon \approx 0.7$ (See [10])
$\mu \approx 2.3$ (See [10])

Finally this is compared to the allowable stress σ_s. I.e. the following must hold:

101 $$\sigma_s > \sigma_{i_{max}}$$

Disregarding λ and choosing a gear with $d = 36\,[\mathrm{mm}]$, $m = 1$, $z = 36$ and $b = 10\,[\mathrm{mm}]$, and with $M = 3000\,[\mathrm{Nmm}]$ (see Figure 59) and $\omega = 44\,[\mathrm{rad/s}]$ the following applies for the shear stress in a tooth feet $\sigma_{i_{max}}$:

$$\sigma_{i_{max}} = 44.23\,[\frac{\mathrm{N}}{\mathrm{mm}^2}]$$

Then for unhardened steel with an allowable stress of 160 $[\frac{\mathrm{N}}{\mathrm{mm}^2}]$ the gear tooth is strong enough against shear:

$$\sigma_s = 160\,[\frac{\mathrm{N}}{\mathrm{mm}^2}] \;> \sigma_{i_{max}} = 44.23\,[\frac{\mathrm{N}}{\mathrm{mm}^2}]$$

4.3 Bearing sizing

In choosing a sufficient bearing the setup dimensions have played the dominant role, nevertheless attention is also paid to the lifetime of the bearing. The setup required a bearing inner diameter of $d = 25\,[\mathrm{mm}]$ an outer diameter $D = 32\,[\mathrm{mm}]$ and a bearing width of $B = 4\,[\mathrm{mm}]$. D is chosen as small as possible in order to maintain an aerodynamic body. These dimensions led to a bearing of *type 6705 2 RS*, with the following properties:

$Cr = 110\,[\mathrm{kg}]$ = dynamic load rate
$Cor = 85\,[\mathrm{kg}]$ = static load rate
$\omega_{max} = 10200\,[rpm]$ = Maximum revolutions per minute

The bearing lifetime is calculated as follows [10]:

102 $\quad L = \left(\frac{C}{F}\right)^P$ = total number of revolutions in millions

Whereby:

$P = 3$, for ball bearings
$P = \frac{10}{3}$, for roller bearings
C = load rating

103 $\quad F = X \cdot F_r + Y \cdot F_a$ = force load

F_r = radial force load
F_a = axial force load
X and Y depend on the values of F_r, F_a and C, see [10].

The bearing lifetime expressed in term of hours is determined as follows:

104 $\quad L_h = \frac{L}{(n \cdot 60 \cdot 10^{-6})}$

With:

$n = 420\,[\mathrm{rpm}]$ = the angular velocity in [rpm]

F_r and F_a are determined from the reaction forces. For the reaction forces applies (see Figure 63):

$F_x = F_{z1} = \pm 21.5[\mathrm{N}]$
$F_y = F_{y1} = \pm 1.6\ [\mathrm{N}]$
$F_z = F_{x1} = \pm 14[\mathrm{N}]$

First the total radial force load F_R and the total axial force F_A are determined as follows:

105 $$F_R = \sqrt{F_x^2 + F_z^2}$$
106 $$F_A = F_y$$

As the translational reaction forces are transmitted by four bearings, the following applies for the load per bearing:

107 $$F_r = \frac{F_R}{4}$$
108 $$F_a = F_A$$

Considering F_r is much larger than F_a, X is taken 1 and Y is taken 0. Then with $C = Cr$, the chosen bearing has a lifetime of $L_h = 3.5 \cdot 10^{12}[\mathrm{hours}]$.

4.4 Procedure for development aerodynamic shield

In order to reduce flow disturbances, the Robird wind tunnel test setup is provided with an aerodynamic shield (see Figure 56). This shield is fabricated through the process of vacuum forming. First a CAD (SolidWorks) design is made of the desired form/shape, thereafter a CAD (SolidWorks) design of the mold is developed. Next, the mold is fabricated and finally with it, the shield is vacuum formed. In the following, these steps are explained in somewhat more detail:

- **CAD (SolidWorks) Design (see** Figure 56 **and** Figure 57**)**:
    - **Form/shape**: The shape of the shield is dictated by the mechanism it should cover and by a symmetric requirement it needs to abide by in order to obtain interpretable aerodynamic measurements with the setup. This desired shape is designed in SolidWorks, see Figure 56.
    - **Mold**: The mold is designed based on the inner dimensions of the desired shield. For it, a frame is developed, consisting of various profile plates in order to capture the form of the shield, see Figure 57. The mold body is to be fabricated from clay, using these profiles as guidance for the shape of the shield.
- **Fabrication** (see Figure 58):
    - **Fabrication of the mold**:
        - **Frame**: The frame for the mold, consisting of various profiles to describe the form of the shield, is manufactured from delrin plates, through laser cutting.
        - **Body**: The mold body is created by filling the frame with a mixture of two components of polyurethane clay. The clay is given time to dry (one day) and afterwards it I finished through sanding.

- **Base**: The mold is completed with a wooden base plate manufactured through laser cutting and consisting of holes to allow air to escape in the vacuum forming process such that the form is captured well.

- **Fabrication of the form/shape**:

  - **Basic form/shape**: The completed mold is now used for vacuum forming the shield out of plastic polystyrene sheet. In an oven, a plastic plate is heated and subsequently sucked onto the mold, allowing it to capture the desired shape.
  - **Finishing**: Finally the shield is finished by cutting out the desired contour and holes.

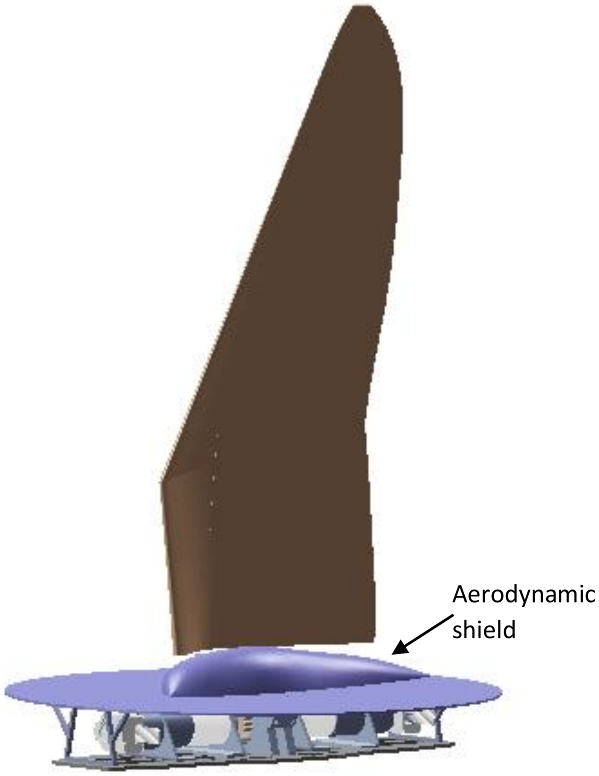

Figure 56 Robird wind tunnel test setup

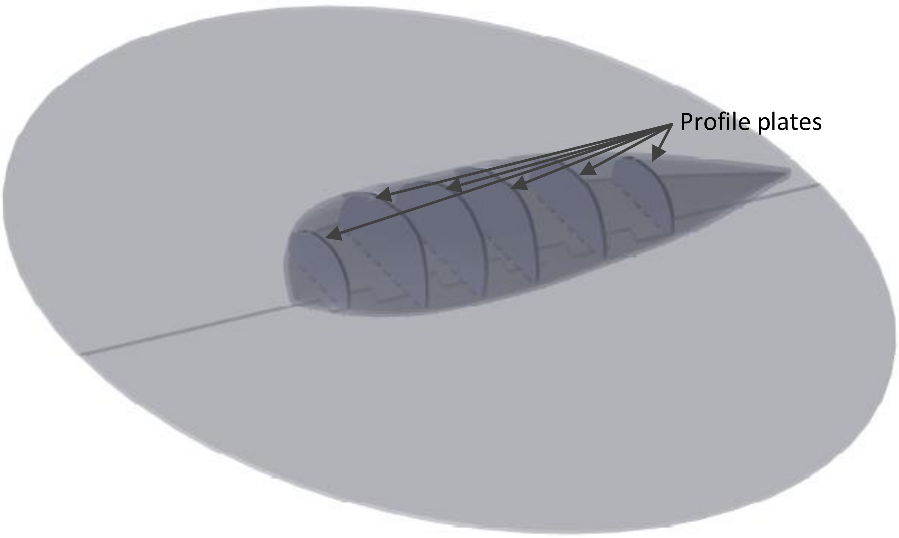

Figure 57 Mold for the aerodynamic shield

Delrin frame:

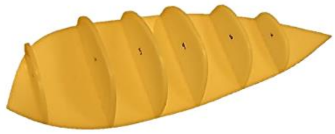

Clay components:

Un-sanded body:

Sanded body:

Completed mold:

Finished shield:

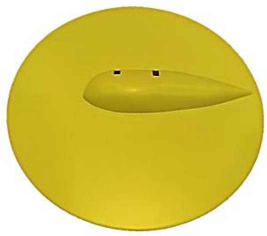

Figure 58 Vacuum forming procedure for development of aerodynamic shield

Appendix 5 Equipment selection

5.1 Gearbox, motor, encoder and control unit selection

After determining the required motor power, first a proper gearbox is chosen then the speed and torque conversed to the motor axis are used to select the proper motor type with the proper winding. Finally a suitable sensor and controller are chosen based on the required resolution and type of control applied respectively. A procedure as discussed in [12] is followed.

5.1.1 Motor power

There is chosen for a brushless DC motor, i.e. an electronically commutated (block commutation) EC motor, over a brushed DC motor because they are applicable at higher speed, leaving more freedom for choosing a larger gearbox for reducing the motor input current and they are not only applicable for continuous operation, but also for highly dynamic servo drives.

The power balance of the motor is described as follows:

109 $$P_{el} = P_{mech} + P_J$$

With:

$P_{el} = U \cdot I$ = the electrical power
$P_{mech} = \frac{\pi}{30000} \cdot n \cdot M$ = the mechanical power, with n in [rpm] and M in [mNm]
$P_J = R \cdot I^2$ = the power losses of the winding
U = voltage
I = current
$\frac{1}{k_n \cdot k_M} = \frac{\pi}{30000}$
k_n = speed constant
k_M = torque constant
R = Resistance
$n = k_n \cdot U_{ind}$ = motor speed
$M = k_M \cdot I$ = motor torque
i = gear reduction
$U_{ind} = EMF$ = voltage induced in the winding

Prior to selecting the motor and gearbox, first the required motor-gearbox output torque M (see Figure 59) and speed n (see the slope of Figure 60) are investigated:

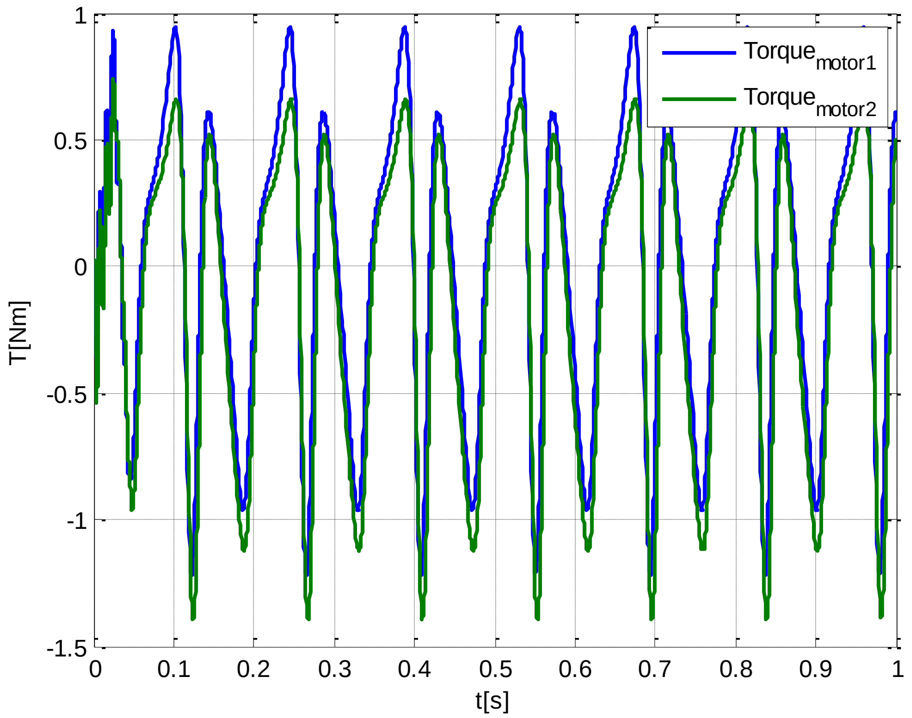

Figure 59 Required motor torque output

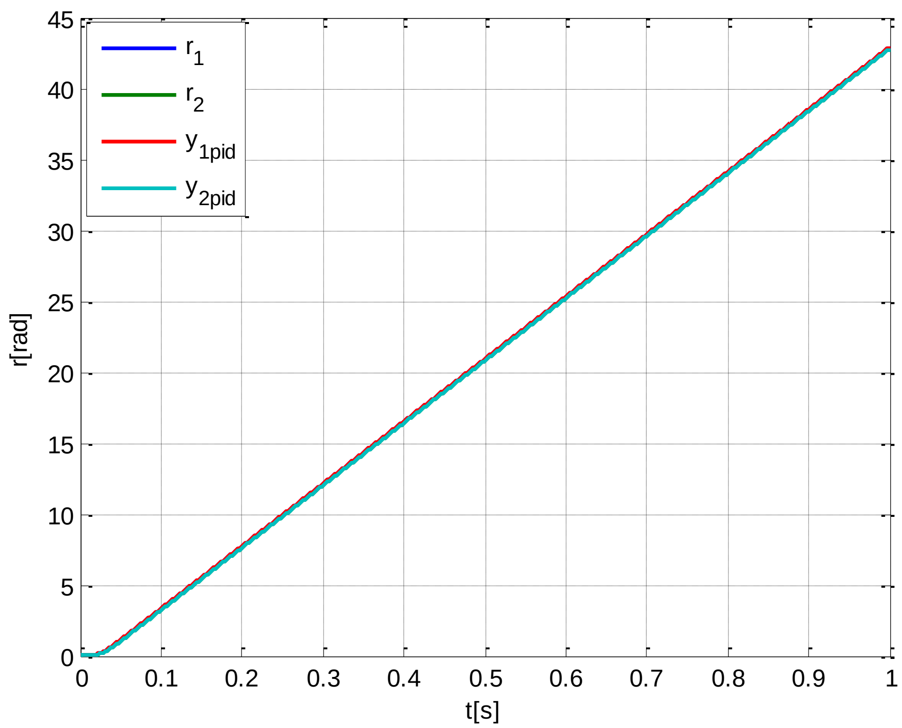

Figure 60 Required motor angle position

Maximum loaded configuration (n_{max}, M_{max})

From the motor output angle it follows that the maximum speed is 44 [rad/s] (7 [Hz]), i.e. $n_{max} = 420\ [\mathrm{rpm}]$, it further follows that the maximum required torque output (absolute value) is 1.4 [Nm], i.e. $M_{max} = 1400\ [\mathrm{mNm}]$. I.e. the operating condition under maximum load is (n_{max} ,M_{max}):

- $n_{max} = 420\ [\mathrm{rpm}]$
- $M_{max} = 1400\ [\mathrm{mNm}]$

Motor power requirement

Then the required maximum mechanical power the motor should be able to supply is:

110 $$P_{mech}[\mathrm{W}] > \left(\frac{\pi}{30000}\left[\frac{\mathrm{W}}{\mathrm{rpm}\cdot\mathrm{mNm}}\right]\cdot n[\mathrm{rpm}]\cdot M[\mathrm{mNm}] = \frac{\pi}{30000}\cdot 420\cdot 1400 = 62\ [\mathrm{W}]\right)$$

Before a motor, able to deliver this mechanical power, is chosen, first a suitable gearbox is chosen.

5.1.2 Gearbox selection

The conversion between gear output and motor shaft is described as follows:

111 $$n_{mot} = i\cdot n_B$$
112 $$M_{mot} = \frac{M_B}{i\cdot\eta_G}$$

Where:

n_{mot} = motor speed
n_B = gear output speed
M_{mot}= motor torque
M_B= gear output torque
η_G = gear efficiency

Gearbox requirements

For an EC motor with a power delivery close to 80 [W] a typical range for motor nominal speed $\mathrm{n_{mot}}$ is 9500 [rpm] to 15000 [rpm] (see [12]). Applying this to equation 111 yields the following requirement for the gear reduction i:

113 $$\frac{9500}{n_B} \leq i \leq \frac{14000}{n_B}$$

This means:

$$\left(\frac{9500}{420} = 23\right) \leq i \leq \left(\frac{14000}{n_B} = 34\right)$$

Further requirements to be met by the gearbox are *(see also* [12]*):*

114 $$M_B < M_{H,G}$$
115 $$M_B < 2\cdot M_{N.G}$$

With:

$M_{H,G}$ = intermittently permissible torque at gear output
$M_{N,G}$ = gearbox maximum continuous output torque

Chosen gearbox
With:

$n_B = n_{max} = 420[\text{rpm}]$
$M_B = M_{max} = 3000[\text{mNm}]$

A planetary gearhead is chosen over a spur gearhead as the former is more suitable for the transfer of relatively high torques. A **Maxon Planetary Gearhead GP 32 C** Ø $32\ \text{mm}$**, 1.0 – 6.0 Nm** is chosen with:

- $i = 23$
- $\eta_G = 0.75$
- $M_{N,G} = 3\ [\text{Nm}]$
- $M_{H,G} = 3.75\ [\text{Nm}]$

With the chosen gearbox, the above requirements are met:

$(M_B = M_{max} = 1400[\text{mNm}]) < \left(M_{H,G} = 3750[\text{mNm}]\right)$
$(M_B = M_{max} = 1400[\text{mNm}]) < (2 \cdot M_{N.G} = 2 \cdot 3000[\text{mNm}] = 6000[\text{mNm}])$
$\left(\frac{9500}{420} = 23\right) \leq (i = 23) \leq \left(\frac{14000}{n_B} = 34\right)$

5.1.3 Motor type selection

New maximum loaded configuration $(\boldsymbol{n_{mot,max}}, \boldsymbol{M_{mot,max}})$
Applying $n_B = n_{max} = 420\ [\text{rpm}]$ and $i = 23$ to equation 111 yields a maximum motor speed of $n_{mot,max} = 9660[\text{rpm}]$.

Applying $M_B = M_{max} = 1400\ [\text{mNm}]$, $i = 23$ and $\eta_G = 0.75$ to equation 112 yields a maximum motor torque of $M_{mot,max} = 81.2[\text{mNm}]$.

Hence with the gearbox applied, the new operating condition for the motor under maximum load is $(n_{mot,max}\ , M_{mot,max})$:

- $n_{mot,max} = 9660\ [\text{rpm}]$
- $M_{mot,max} = 82\ [\text{mNm}]$

Motor torque requirement
The requirements to be met here are (see also [12]):

$116 \quad M_{mot,max} < M_H$
$117 \quad M_{mot,max} < 2 \cdot M_N$

With:
M_H = stall torque
M_N = nominal torque (max. continuous torque)

Electric requirement (selecting the winding)
When selecting the winding, care must be taken that the voltage applied directly to the motor is sufficient for attaining the required speed in all operating points. Then, when regulated with a servo drive, this means that in work cycles, all operating points must lie beneath the speed-torque line at maximum voltage U_{max}. This means that the following requirements need to be met by all operating points $(n_{mot}\ , M_{mot})$ (see [13]):

118 $k_n \cdot \eta_{eff} \cdot U_{max} = n_0 > n_{mot} + \frac{\Delta n}{\Delta M} M_{mot}$

With:

$\frac{\Delta n}{\Delta M}$ = the speed torque gradient
$\eta_{eff} = 0.8$ = efficiency for obtaining the effective motor input voltage ($\eta_{eff} \cdot U_{max}$) after among other things voltage drop across the servo (10% to 20% of the source voltage; see [12]).
U_{max} = nominal voltage

Motor current requirement
Finally, the current is checked. Analog to the torque, the requirements to be met here are:

119 $I_{mot,max} < I_H$
120 $I_{mot,max} < 2 \cdot I_N$

With:
$I_{mot,max}$ = actual peak current for motor input = 6 [A] (see Figure 61)
I_H = starting current
I_N = nominal current (max. continuous current)

Motor choice
The motor which meets the above requirements is the **Maxon EC 32 Ø32, brushless, 80 Watt, CE approved** with:

- $k_m = 0.013$ [Nm/A]
- $R = 0.573[\Omega]$
- $M_N = 41.2[\text{mNm}]$
- $M_H = 407[\text{mNm}]$
- $I_H = 31.4[\text{A}]$
- $\frac{\Delta n}{\Delta M} = 6.82\ [\frac{\text{rpm}}{\text{mNm}}]$
- $\text{k}_\text{n} = 737\ \left[\frac{\text{rpm}}{\text{V}}\right]$
- $\text{U}_\text{max} = 18\ [\text{V}]$
- $I_N = 3.61[\text{A}]$

With the chosen motor, these requirements are met as follows:

$(P_{mech}[\text{W}] = 80[\text{W}]) > \left(\frac{\pi}{30000} \cdot n \cdot M = \frac{\pi}{30000} \cdot 420 \cdot 1400 = 62\ [\text{W}]\right)$
$\left(M_{mot,max} = 82[\text{mNm}]\right) < (M_H = 1670[\text{mNm}])$
$\left(M_{mot,max} = 82[\text{mNm}]\right) < (2 \cdot M_N = 2 \cdot 41.2[\text{mNm}] = 82.4[\text{mNm}])$
$\left(k_n \cdot \eta_{eff} \cdot U_{max} = 737 \cdot 0.8 \cdot 18 = 10613[\text{rpm}]\right) > \left(n_{mot,max} + \frac{\Delta n}{\Delta M} M_{mot,max} = 9660 + 6.82 \cdot 82 = 10219[\text{rpm}]\right)$
$\left(I_{mot,max} = 6[\text{A}]\right) < (I_H = 31.4[\text{A}])$
$\left(I_{mot,max} = 6[\text{A}]\right) < (2 \cdot I_N = 2 \cdot 3.61[\text{A}] = 7.22[\text{A}])$

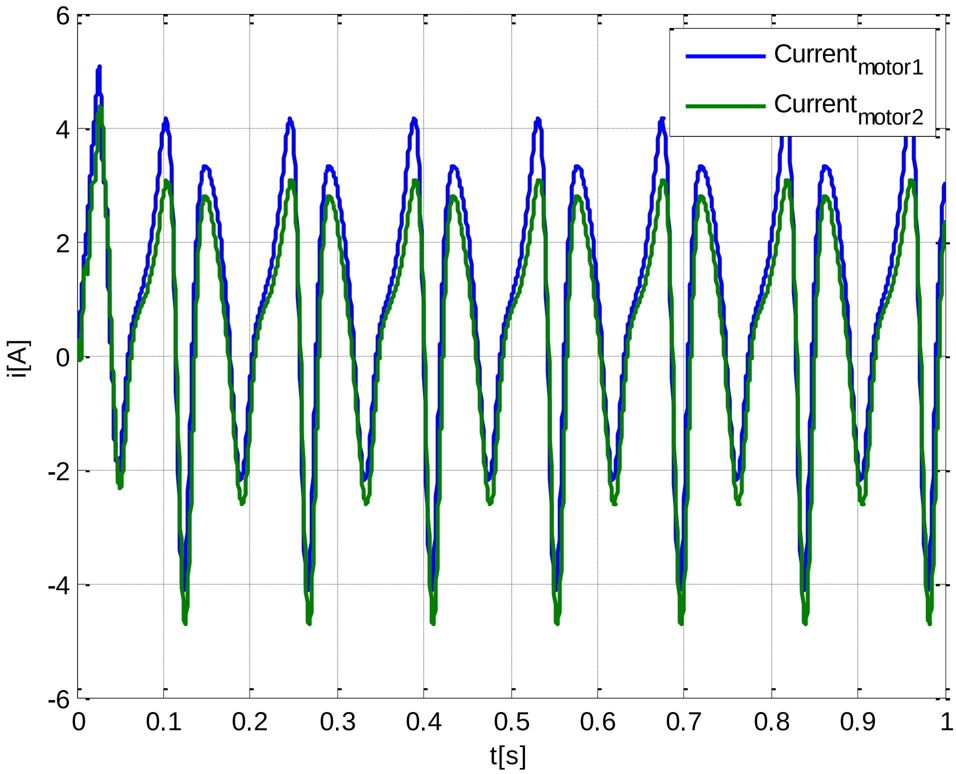

Figure 61 motor current input

5.1.4 Sensor selection

A digital incremental encoder is chosen over both a tachometer and a resolver because it is the most suitable for control tasks.

Sensor requirement

Considering the control target is to obtain an accuracy of 0.1° the resolution res_i requirement is set to:

121 $$res_i < \left(\frac{0.1°}{10} = 0.01°\right)$$

Chosen sensor

The chosen encoder is the **Encoder HED_5540** with 500 CPT (counts per turn) and 3 channels. Hence with four counts made per encoder cycle, i.e. both pulse signals (quadrature signals) are available and both rising and falling edges of the pulses are detected, the physical resolution res in degrees becomes (see [13]):

122 $$res = \frac{360°}{4N} = \frac{360°}{4 \cdot 500} = 0.18°$$

With the encoder placed before the gearbox, the physical resolution after the gearbox res_i becomes:

123 $$res_i = \frac{360°}{4Ni} = \frac{360°}{4 \cdot 500 \cdot 23} = 0.0078°$$

Hence according to equation121, a $res_i = 0.0078°$ is considered sufficient.

5.1.5 Controller selection

As the goal here is to obtain a fixed phase shift between two motors operating at the same speed, these motors are controlled via position control rather than speed control or current (torque) control.

Controller requirements

Here, the requirements aimed to be met are:

124 $V_{out,max} > 0.8 \cdot V_{cc}$: The voltage drop across the servo should be smaller than 20%, as only this is accounted for (see equation 118).

125 $I_{cont} > \frac{1}{2} I_{mot,max}$

126 $I_{\max(<1s)} > I_{mot,max}$

With:

I_{cont} = continuous output current
$I_{\max(<1s)}$ = maximum output current
$V_{out,max}$ =maximum output voltage
V_{cc} = operating voltage

To this end, there is chosen for an **ELMO Whistle 5/60 control unit** with the following characteristics:

- $V_{cc} = 7.5 - 59$ [VDC]
- $V_{out,max} = 0.95 \cdot V_{cc}$
- $I_{\max(<1s)} = 10$ [A]
- $I_{cont} = 5$ [A]

With this chosen control unit, the requirements are met as follows:

$$\left(V_{out,max} = 0.95 \cdot V_{cc}\right) > (0.8 \cdot V_{cc})$$
$$(I_{cont} = 5\,[\mathrm{A}]) > \left(\frac{1}{2} I_{mot,max} = \frac{1}{2} 6[\mathrm{A}] = 3[\mathrm{A}]\right)$$
$$(I_{\max(<1s)} = 10[\mathrm{A}]) > \left(I_{mot,max} = 6[\mathrm{A}]\right)$$

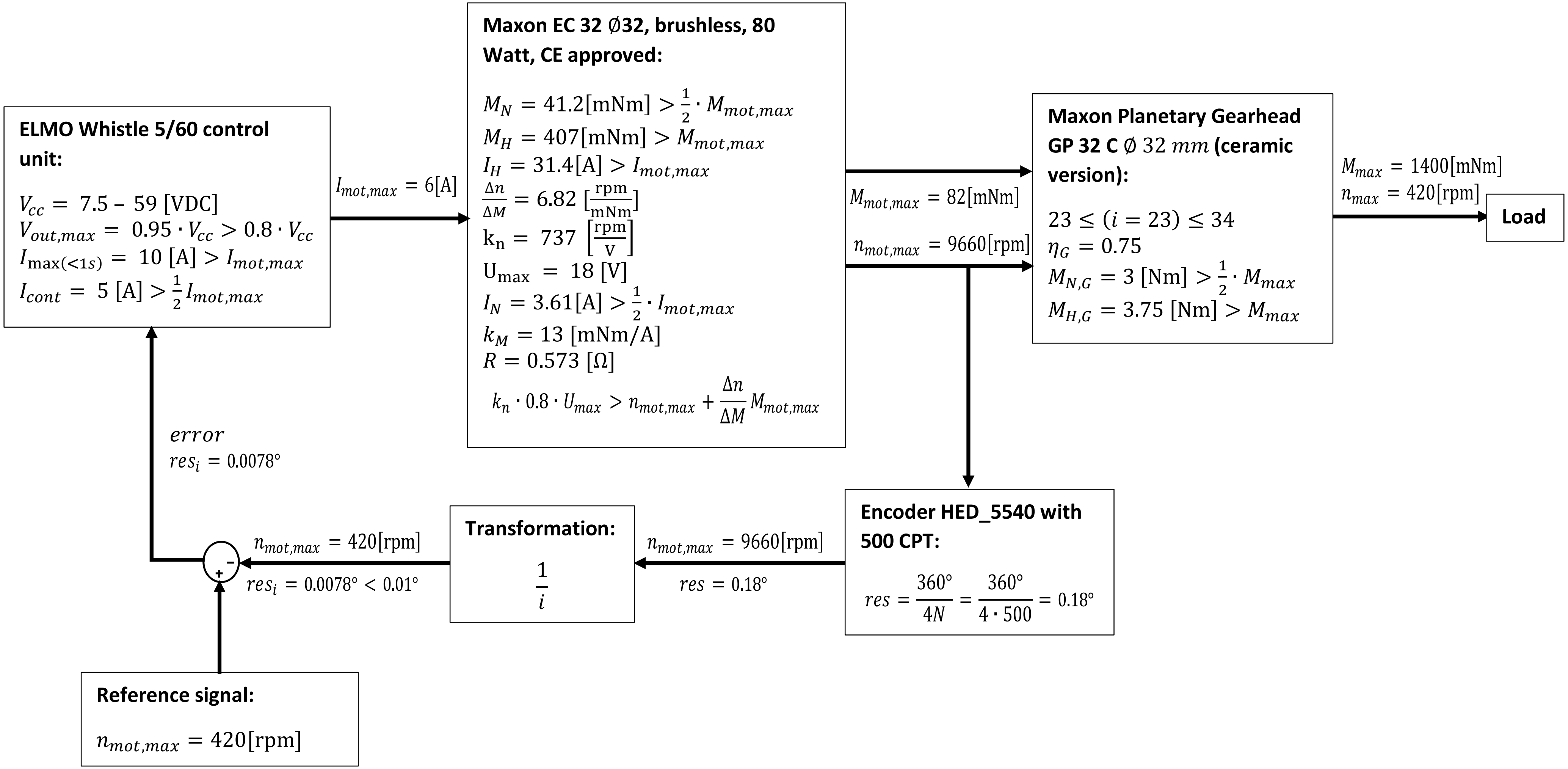

Figure 62 Complete overview of the chosen equipment and the achieved requirements

5.2 Remaining equipment selection

5.2.1 Force sensor selection

After including aerodynamic loads, from Spacar the following is obtained for the reaction forces and torques:

The reaction forces calculated by Spacar are:

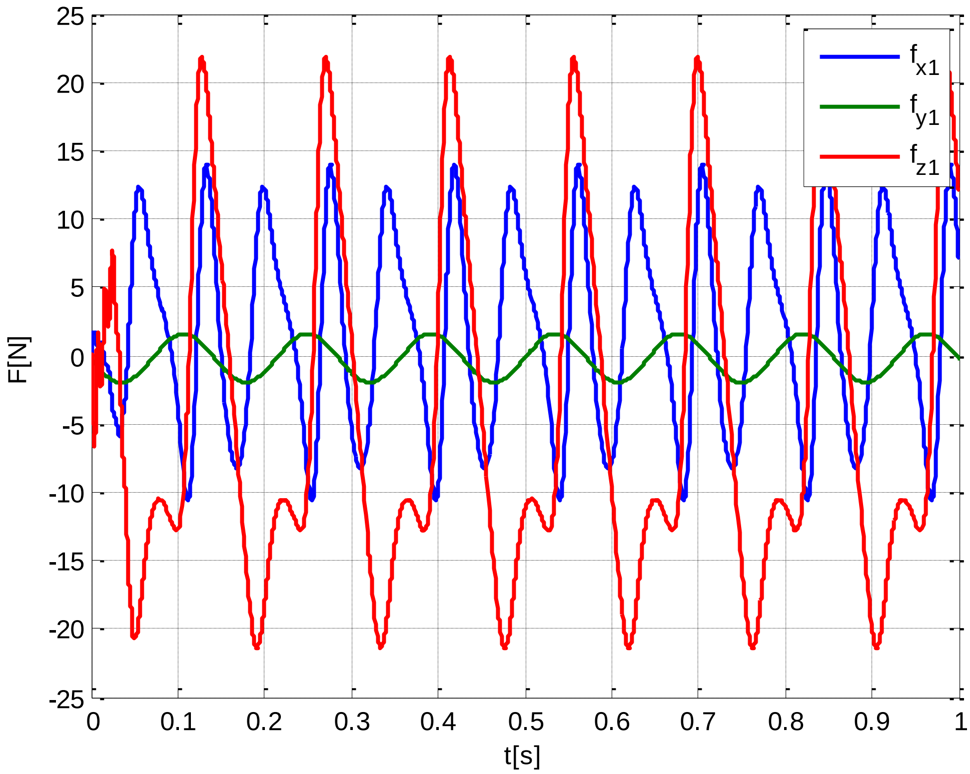

Figure 63 Reaction forces (after including aerodynamic loads)

Spacar calculates the torques t dual to the Euler parameters. However, it is not straightforward to understand their physical significance, hence a transformation to the more familiar equilibrium torques T is required. Hereby the principle of virtual work is used as illustrated in [2]:

127 $$t = A^T T$$

With:

128 $$A = diag[I, 2\Lambda]$$

With:

$\Lambda =$ Function of the Euler parameters λ_0, λ_1, λ_2 and λ_3

Then, with $\lambda_0 = \lambda_1 = \lambda_2 = \lambda_3 = 1$ (as is the case here), the following applies for the torque:

129 $T = \frac{1}{2}t$

After applying equation129, the following is obtained for the reaction torques:

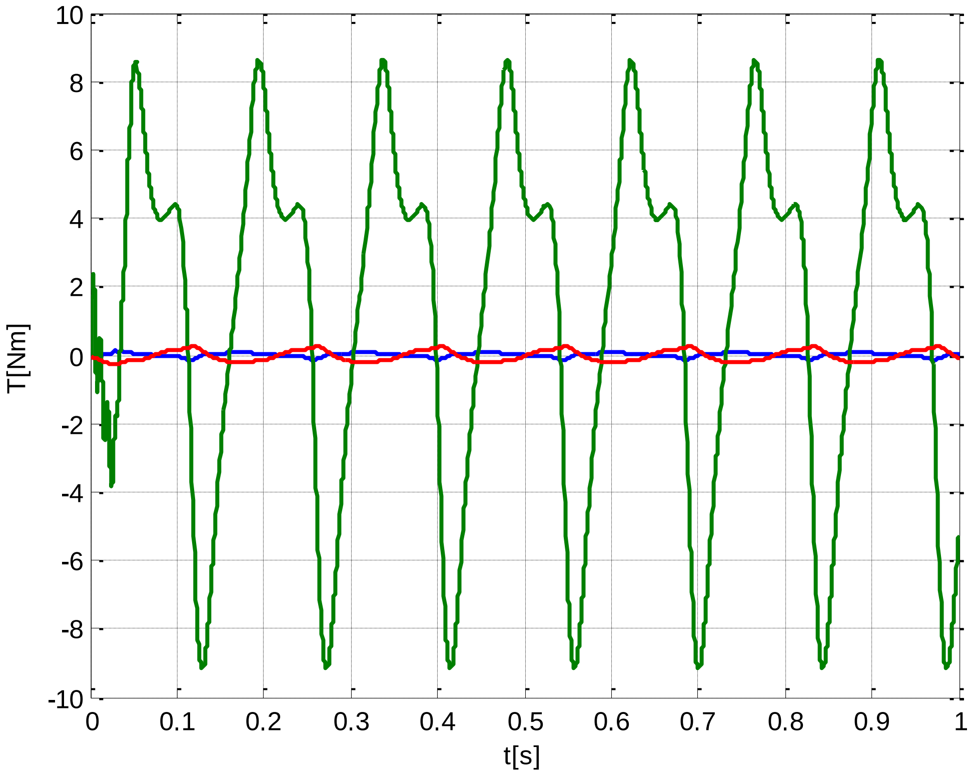

Figure 64 Actual reaction torques (after including aerodynamic loads)

From the figures applies:

$F_x = F_{z1} = \pm 21.5[\mathrm{N}]$
$F_y = F_{y1} = \pm 1.6\ [\mathrm{N}]$
$F_z = F_{x1} = \pm 14[\mathrm{N}]$
$T_x = \pm 0.15\ [\mathrm{Nm}]$
$T_y = \pm 9\ [\mathrm{Nm}]$
$T_z = \pm 0.25\ [\mathrm{Nm}]$

Based on these results, a 6-DOF sensor developed at the department of Mechanical Automation of the University of Twente could be applied with the following ranges [14]:

Forces in xyz-direction:

- Range: $\pm 50[\mathrm{N}]$
- Resolution: $\pm 0.009[\mathrm{N}]$
- Error: 0.8%

Torque in xyz-direction:

- Range: $\pm 8[\mathrm{Nm}]$
- Resolution: $\pm 0.0015[\mathrm{Nm}]$
- Error: 2.5%

As discussed in the following section, the placement of the sensor can be optimized by appropriately adjusting its distance in z-direction (x1-direction).

5.2.1.1 Optimal placement force sensor

In this section a simplified mechanism of the wind tunnel test setup is considered (see Figure 65) in order to justify the optimal placement of the force sensor with the aim at utilizing its measurement range to the fullest in order to obtain an as small as possible relative error. The force sensor is placed in node 6 and thus measures the reaction forces f_{x_6}, f_{y_6} and f_{ϕ_8}.

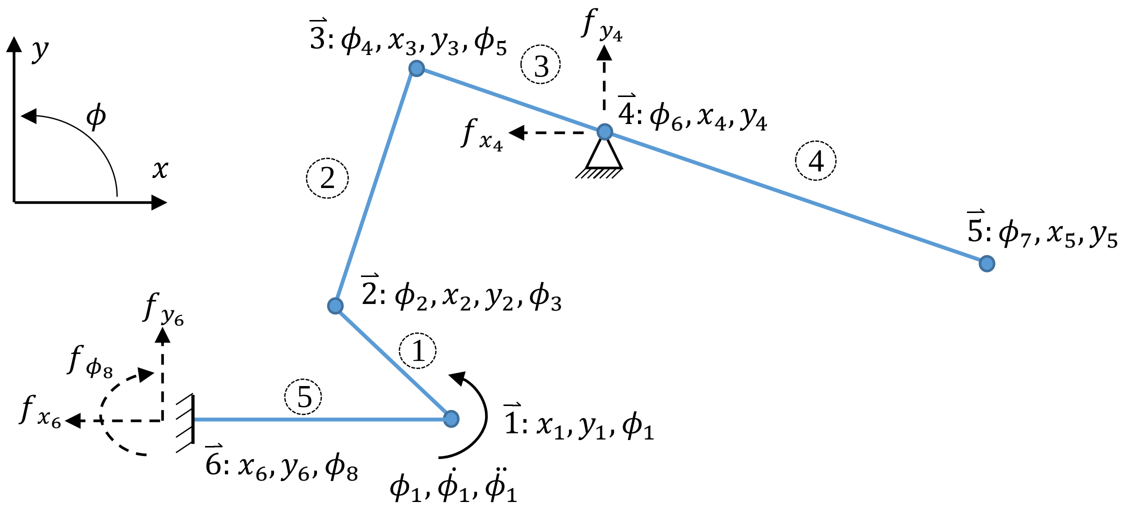

Figure 65 simplified mechanism of the wind tunnel test setup for Robird

From this configuration the following applies:

For the nodal coordinates applies:

130

$$x = \left[\left[x^{(o)}\right]^T \quad \left[x^{(c)}\right]^T \quad \left[x^{(m)}\right]^T\right] =$$
$$[[x_6 \quad y_6 \quad \phi_8 \quad x_4 \quad y_4]^T \quad [x_1 \quad y_1 \quad x_2 \quad y_2 \quad \phi_2 \quad \phi_3 \quad x_3 \quad y_3 \quad \phi_4 \quad \phi_5 \quad \phi_6 \quad x_5 \quad y_5 \quad \phi_7]^T \quad [\phi_1]^T]$$

For the deformation coordinates applies:

$$\varepsilon = \begin{bmatrix} [\varepsilon^{(o)}] \\ [\varepsilon^{(m)}] \\ [\varepsilon^{(c)}] \end{bmatrix} = \begin{bmatrix} [D(x)^{(o)}] \\ [D(x)^{(m)}] \\ [D(x)^{(c)}] \end{bmatrix} = \begin{bmatrix} \begin{bmatrix} \varepsilon_{5e} \\ \varepsilon_{5b} \\ \varepsilon_{1e} \\ \varepsilon_{1b1} \\ \varepsilon_{1b2} \\ \varepsilon_{2e} \\ \varepsilon_{2b1} \\ \varepsilon_{2b2} \\ \varepsilon_{3e} \\ \varepsilon_{3b1} \\ \varepsilon_{3b2} \\ \varepsilon_{4e} \\ \varepsilon_{4b1} \\ \varepsilon_{4b2} \end{bmatrix} \\ [\emptyset] \\ [\emptyset] \end{bmatrix} = \begin{bmatrix} \begin{bmatrix} \sqrt{((x_1 - x_6)^2 + (y_1 - y_6)^2)} - lo_5 \\ (sin(\phi_8))(x_1 - x_6) - (cos(\phi_8))(y_1 - y_6) \\ \sqrt{((x_2 - x_1)^2 + (y_2 - y_1)^2)} - lo_1 \\ (sin(\phi_1))(x_2 - x_1) - (cos(\phi_1))(y_2 - y_1) \\ -(sin(\phi_2))(x_2 - x_1) + (cos(\phi_2))(y_2 - y_1) \\ \sqrt{((x_3 - x_2)^2 + (y_3 - y_2)^2)} - lo_2 \\ (sin(\phi_3))(x_3 - x_2) - (cos(\phi_3))(y_3 - y_2) \\ -(sin(\phi_4))(x_3 - x_2) + (cos(\phi_4))(y_3 - y_2) \\ \sqrt{((x_4 - x_3)^2 + (y_4 - y_3)^2)} - lo_3 \\ (sin(\phi_5))(x_4 - x_3) - (cos(\phi_5))(y_4 - y_3) \\ -(sin(\phi_6))(x_4 - x_3) + (cos(\phi_6))(y_4 - y_3) \\ \sqrt{((x_5 - x_4)^2 + (y_5 - y_4)^2)} - lo_4 \\ (sin(\phi_6))(x_5 - x_4) - (cos(\phi_6))(y_5 - y_4) \\ -(sin(\phi_7))(x_5 - x_4) + (cos(\phi_7))(y_5 - y_4) \end{bmatrix} \\ [\emptyset] \\ [\emptyset] \end{bmatrix} \quad (131)$$

With lo_1, lo_2, lo_3, lo_4 and lo_5 the lengths of beam 1, 2, 3, 4 and 5 respectively.

From the above it follows that there are 14 unknowns (the number of $x^{(c)}$) and 14 equations (the number of $\varepsilon^{(o)}$plus the number $\varepsilon^{(m)}$), hence the system is kinematically determinate. The system has one degree of freedom, namely ϕ_1.

After the motion of the multi-body system is known already, the external forces (including the reaction forces) can be determined as follows (this is explained very well in [2]):

$$f = D_{,x}^T \sigma + h + M\ddot{x} \quad (132)$$

Where:

$$f = \left[[f^{(o)}]^T \quad [f^{(c)}]^T \quad [f^{(m)}]^T \right] =$$
$$\left[[f_{x_6} \quad f_{y_6} \quad f_{\phi_8} \quad f_{x_4} \quad f_{y_4}]^T \quad [f_{x_1} \quad f_{y_1} \quad f_{x_2} \quad f_{y_2} \quad f_{\phi_2} \quad f_{\phi_3} \quad f_{x_3} \quad f_{y_3} \quad f_{\phi_4} \quad f_{\phi_5} \quad f_{\phi_6} \quad f_{x_5} \quad f_{y_5} \quad f_{\phi_7}]^T \quad [f_{\phi_1}]^T \right]$$

M = Mass matrix
h = Convective term of the inertia property which is a function of the position coordinates and quadratic in the velocities

$$\sigma = \left[[\sigma^{(o)}][\sigma^{(m)}][\sigma^{(c)}] \right] =$$
$$\left[[\sigma_{5e} \quad \sigma_{5b} \quad \sigma_{1b1} \quad \sigma_{1b2} \quad \sigma_{1e} \quad \sigma_{1b1} \quad \sigma_{2b1} \quad \sigma_{2e} \quad \sigma_{3b1} \quad \sigma_{3b2} \quad \sigma_{3e} \quad \sigma_{4b1} \quad \sigma_{4b2} \quad \sigma_{4e}][\emptyset][\emptyset] \right]$$
= Stress resultants; partially ($\sigma^{(c)}$) calculated from the linear constitutive Kelvin-Voigt equations (see [2]):

$$\sigma = S\varepsilon + S_d\dot{\varepsilon} \quad (133)$$

S = Stiffness matrix
S_d = Damping matrix

The forces of interest are the reaction forces f_{x_6}, f_{y_6} and f_{ϕ_8}. As the mass matrix is diagonal, node 6 is fixed and beam 5 is rigid, close observation of the system yields that these forces can be calculated as follows:

134

$$f_{x_6} = \sigma_{5e}$$
$$f_{y_6} = \sigma_{5b}$$
$$f_{\phi_8} = \sigma_{5b} \cdot lo_5$$

Hereby σ_{5e} and σ_{5b} are the internal forces in beam 5 which depend on the complete motion of the system (see [2]). To this end the reaction forces f_{x_6} and f_{y_6} will always have the same behavior as long as the motion of the system is not altered. On the other hand the reaction force f_{ϕ_8} also depends on the length of beam 5, lo_5, which is independent of the motion of the system. This can be used to the advantage of the measurements by choosing lo_5 in such a way to fully utilize the measurement range of the force sensor in order to obtain an as small as possible relative error.

The relative error depends on the absolute error ΔX and the measured quantity X as follows:

$$e_r = \frac{\Delta X}{X}$$

A decrease in absolute error (ΔX) and thus a decrease in relative error (e_r) can be obtained by choosing measuring equipment with a higher resolution. However for a chosen force sensor the relative error can be reduced even more by ensuring the measured value (X) is as close as possible to the measurement range of the sensor. In the case of measuring f_{ϕ_8}, this can be achieved by adjusting lo_5, i.e. by adjusting the placement of the force sensor.

5.2.2 Power tool selection

In this section a power tool is selected which can provide for sufficient tightening torque in case the mechanical solution is applied, i.e. the fixing of the phase shift by means of disc frictional connection whereby the discs are held together through preload supplied by a M8 bolt.

Tightening torque

The required tightening torque T required for obtaining the necessary preload $Q = 6000[\mathrm{N}] = 6\ [\mathrm{kN}]$ between the disc with friction coefficient $f = 0.15$ through a bolt with diameter $d = 8[\mathrm{mm}]$ is calculated as follows [11]:

135 $$T = f \cdot d \cdot Q$$

From this follows a required tightening torque $T = 7.2[\mathrm{Nm}]$. This tightening torque can be supplied either manually or through the use of the Bosch power tool: **GSR Mx2Drive Professional** which is able to supply a maximum torque of 12 [Nm].

Appendix 6 System identification and parameter estimation

6.1 Identification plan

System identification and parameter estimation test plan

The mechanism/ test setup is mounted in the wind tunnel with the wing arranged vertically and directed upward. This causes the un-controlled (or poorly controlled) system to behave unstable equivalent to an inverted pendulum. System identification of the open-loop plant thus becomes problematic. To solve this problem the following is done:

1. **Open-loop identification with upside-down configuration:** The first objective of system identification is to gather data for model validation. To circumvent an un-stable open-loop plant, the test setup is still mounted vertically but upside-down, i.e. with the wing directed downwards. In such a way it behaves like a (marginally) stable pendulum rather than an unstable inverted pendulum. In this configuration open-loop system identification can be conducted and the model can be validated qualitatively and also quantitatively (e.g. the coupling behavior can still be captured).

2. **Closed-loop identification with relatively weak control (only P-control):** The second objective of system identification is for control design purposes. For this, the estimation target is the low frequency behavior of the unstable open-loop plant. Hence closed loop identification of the controlled system is required. Control action is applied to keep the wing in position. The applied control is relatively weak to prevent the controller from having a dominant role on the frequency content of the plant input signal. Only proportional control is used. Subsequently, either direct identification or joint-input-output identification can be applied.

System input and output

As discussed above, open-loop identification is conducted on the upside-down configuration. As current control is to be applied through position feedback, the system input and output are taken the current and position respectively.

Frequency range input signal

In order to capture essential dynamic behavior the system should be excited appropriately. Using the elaborate model developed in Spacar as a guideline, the following essential dynamic behavior appear:

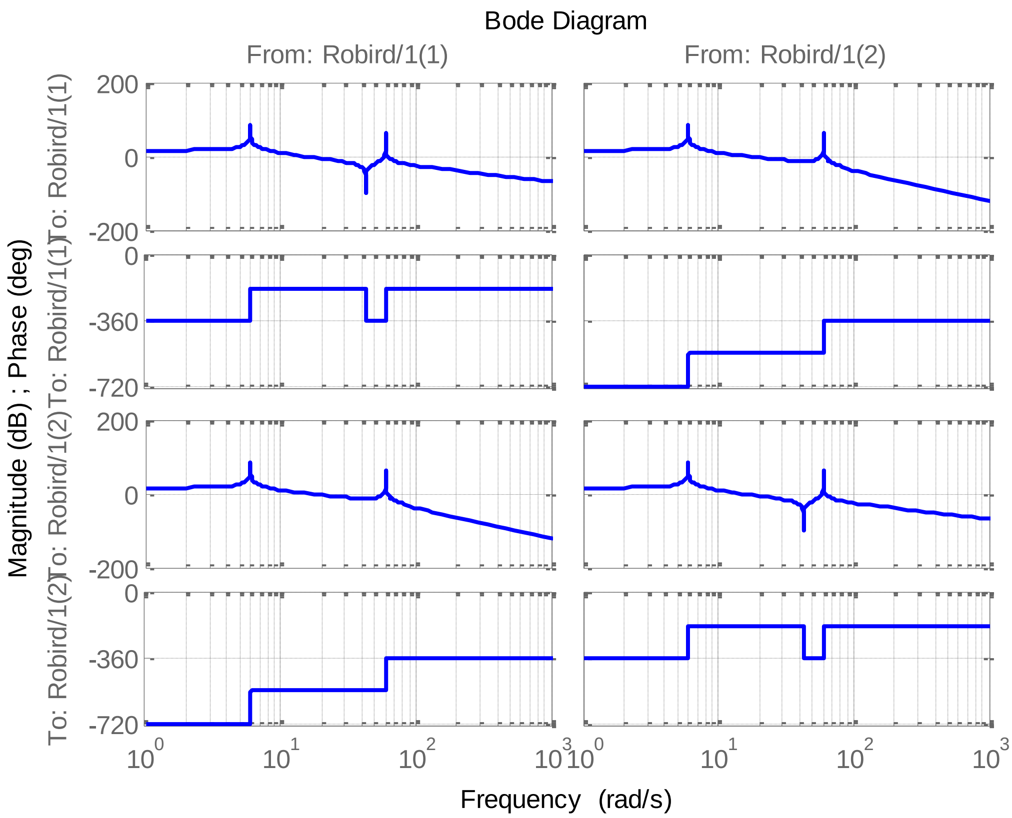

Figure 66 frequency response of the upside-down test setup

1. **Low frequency resonance:** The first occurring resonance can be interpreted as the natural frequency of the pendulum like motion of the upside down configuration:

136 $$\omega_{R_{\text{low}}} \approx \sqrt{\frac{g}{L}}$$

With:

$g = 9.8\ [\frac{\text{m}}{\text{s}^2}]$ = the gravitational acceleration
$L = 0.2\ [\text{m}]$ = approximately half the wing length (wing center of mass)

When calculated, this yields:

$$\omega_{R_{\text{low}}} \approx \sqrt{\frac{9.8}{0.2}} \approx 7[\frac{\text{rad}}{\text{s}}]$$

This agrees to some degree with the value of $6[\frac{\text{rad}}{\text{s}}]$ which is read from Figure 66.

2. **High frequency anti-resonance and resonance:** high frequency resonances and anti-resonances occur due to the mechanical compliant coupling as described in section 2.2

With $\omega_{AR,1} = \omega_{AR,2} = 42.8\ [\frac{\text{rad}}{\text{s}}]$ and $\omega_R = 60.2\ [\frac{\text{rad}}{\text{s}}]$ (see Figure 66), eq. 38 applies very well.

Thus the frequencies of importance are:

$\omega_{R_{\text{low}}} = 6\left[\frac{\text{rad}}{\text{s}}\right] = 0.95\ [\text{Hz}]$
$\omega_{AR,1} = \omega_{AR,2} = 42.8\ \left[\frac{\text{rad}}{\text{s}}\right] = 6.8\ [\text{Hz}]$
$\omega_R = 60.2\ \left[\frac{\text{rad}}{\text{s}}\right] = 9.6\ [\text{Hz}]$

Signal type and signal band
A broadband signal of type SINE (sum of harmonic signals) is chosen. Considering the relevant frequencies as mentioned above, a signal band of 6 [Hz] to 10 [Hz] is chosen for the input signal. To also excite the system at the first resonance frequency, it is given a small initial output (position/angle).

Signal amplitude/ levels
To be sure the system is able to handle the input signal, the signal amplitude/ level is restricted. It is even further restricted to obtain a sufficiently small output (angle/position) such that aerodynamics become negligible (sufficiently small flapping angle) ensuring the data becomes more profitable for model validation as the model did not account for aerodynamics which were only modeled as disturbances. To this end, 0.1 [A] is taken for the amplitude of the input signal.

Sample frequency
As a rule of thumb (see [15]), the sampling frequency ω_s should be taken such that the Nyquist frequency $\omega_N = \frac{\omega_s}{2}$ is well above the highest relevant frequency. Choosing a sampling time $t_s = 10^{-2}[\text{s}]$ a sampling frequency $\omega_s = 100\ [\text{Hz}]$ is obtained. This means a Nyquist frequency $\omega_N = 50\ [\text{Hz}]$ is obtained which is at least 5 times the largest relevant frequency $\omega_R = 9.6\ [\text{Hz}]$ and thus considered large enough.

Data processing
In order to improve the quality of identification, the data can be filtered (pass band: 10 [rad/s] 100 [rad/s]) after acquisition.

Results
Using the input signal described above, i.e. a SINE signal covering a signal band of 6 [Hz] to 10 [Hz] and an amplitude of 0.1 [A], and a sampling frequency $\omega_s = 100\ [\text{Hz}]$, output data is generated through the nonlinear model developed in Spacar. Next system identification is conducted in Ident using prior knowledge of the system, i.e. a fourth order TITO (two input two output) system. From the results it follows that both estimations (open-loop and closed-loop identification) approach the model well.

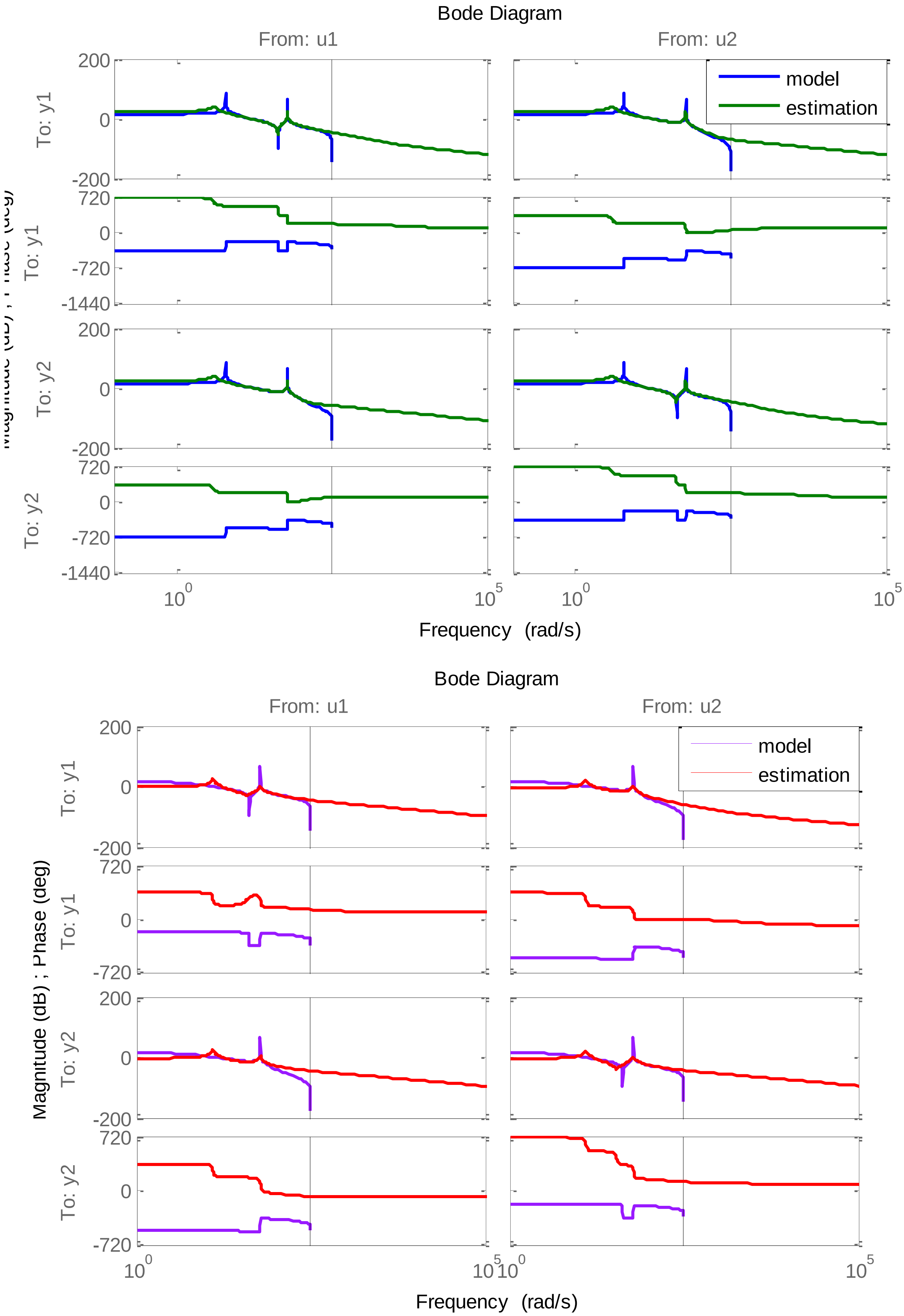

Figure 67 Upper: Results of open-loop system identification: Gzid_ol: Linearized model of the non-linear Spacar model ss1: identification; Lower: Results of closed-loop system identification: Gzid_ol: Linearized model of the non-linear Spacar model ss3: identification

Motor initialization prior to identification

Prior to system identification, initialization of the motors is conducted using the **wizard** of the composer software ([16]; also see [17], [18] and [19]):

1. Specifying motor parameters
2. User interface for absolute feedback
3. Defining system limits
4. Tuning the current loop
5. Configuring commutation
6. Tuning the velocity loop
7. Tuning the position loop
8. Tuning the dual loop

6.2 Damping estimation

Prior to model validation, first system damping is estimated through measurement. Damping d is calculated from current I_m and angular velocity ω_m measurements for quasi-static motion:

137 $$d = \frac{T}{\omega} = \frac{2000}{2 \cdot \pi} \cdot i^2 \cdot \frac{k_m \cdot I_m}{\omega_m}$$

Whereby:

d = damping in [Nms/rad]
T= torque in [Nm]
ω = angular velocity in [rad/s]
i = gear transmission = 18
k_m = torque constant
I_m = measured current in [A] = 0.0205 [Nm/A]
ω_m = measured angular velocity in [counts/turn]

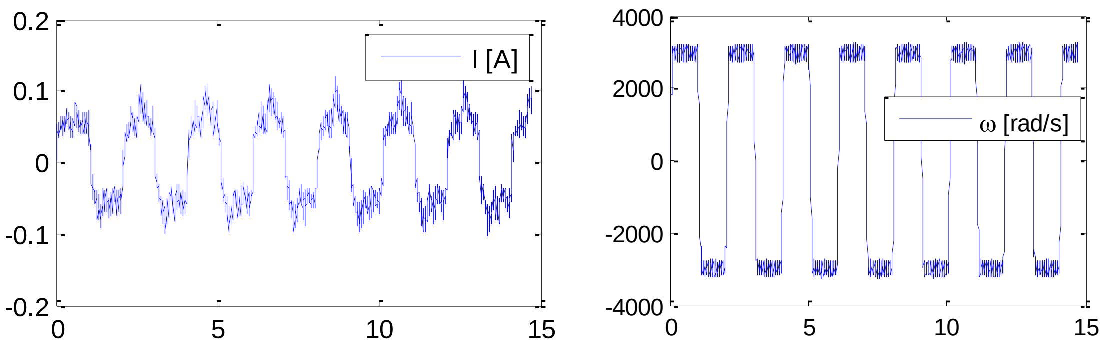

Figure 68 Left: measured current; Right: measured angular velocity

Applying this data (Figure 68) to equation 137 yields a mean damping of $d = 0.04\ [\frac{\text{Nms}}{\text{rad}}]$. This damping is added to the model in Spacar.

Appendix 7 Elmo motion control

7.1 Cascaded position velocity control

The SimplIQ ELMO Whistle controllers used in the Robird wind-tunnel test setup feature cascaded position (P) –velocity (PI) control (PIP-control) instead of the more widely used PID-control. This is depicted in Figure 69. Typically the velocity loop consists of integral (K_{VI}) and proportional control (K_{VP}) to ensure rapid reaction to changing commands and providing resistance to high-frequency load disturbances. The position loop consists of proportional control (K_P) to ensure the position is tracked well. A somewhat more detailed velocity and position loop as used in the SimplIQ ELMO Whistle controllers are presented in Figure 70 and Figure 71 respectively.

In order to obtain optimal performance, tuning is required. In [20] a procedure for tuning is given for such a cascaded position-velocity control loop. Each of the gain influences a distinct frequency region. K_{VP} typically covers the high frequency zone, between 10 and 30 [Hz]. K_{VI} covers the mid frequency region, typically between 10 and 30 [Hz] whereas K_P covers the low frequency region, 0 to 10 [Hz].

In the following a very brief discussion is given for tuning these control parameters. For a more elaborate discussion see [20]. First K_{VP} is tuned (K_{VI} is set to zero) in velocity mode. A step reference is given for the velocity, typically around 250 [rpm]. K_{VP} is chosen as high as possible while still preventing any overshoot. Next K_{VI} is increased until 15[%] overshoot is obtained. Switching to position mode, finally K_P is tuned. A trapezoidal reference is chosen and K_P is chosen as high as possible while still preventing overshoot.

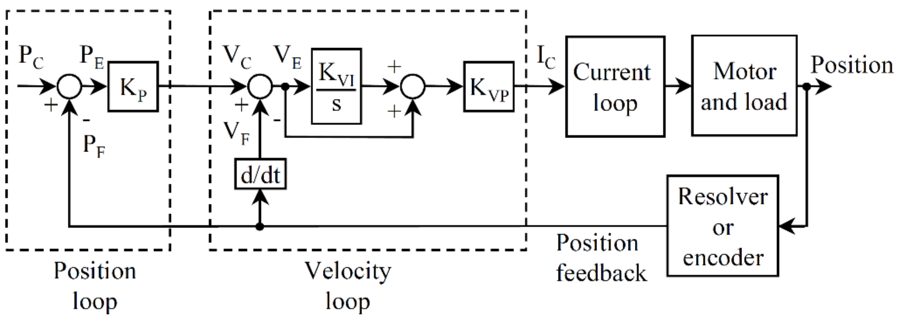

Figure 69 Block diagram of cascaded position-velocity loops [20]

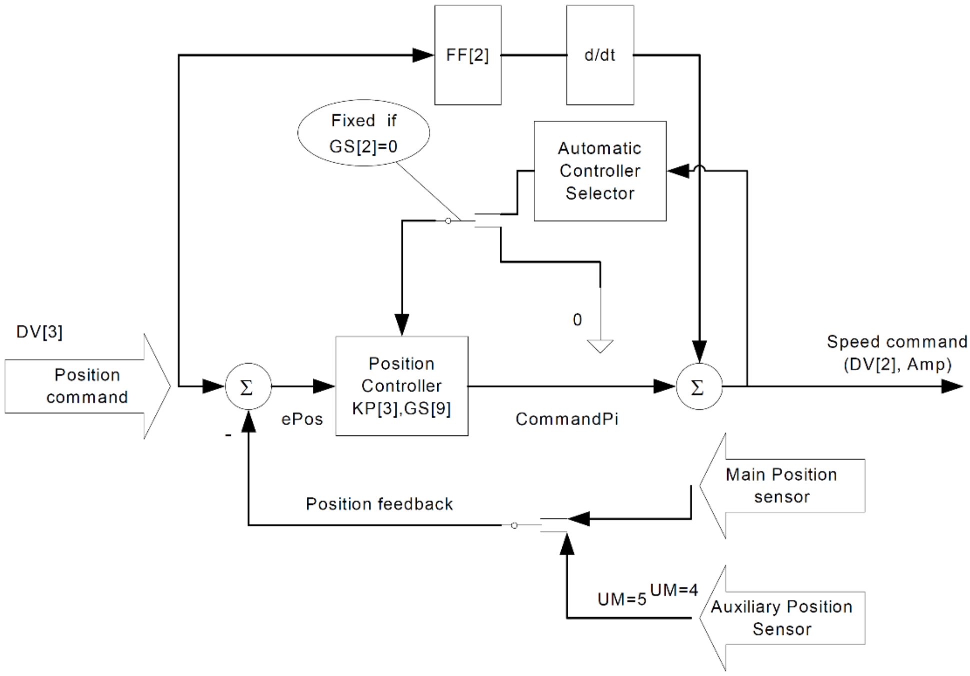

Figure 70 Speed controller block diagram [18]

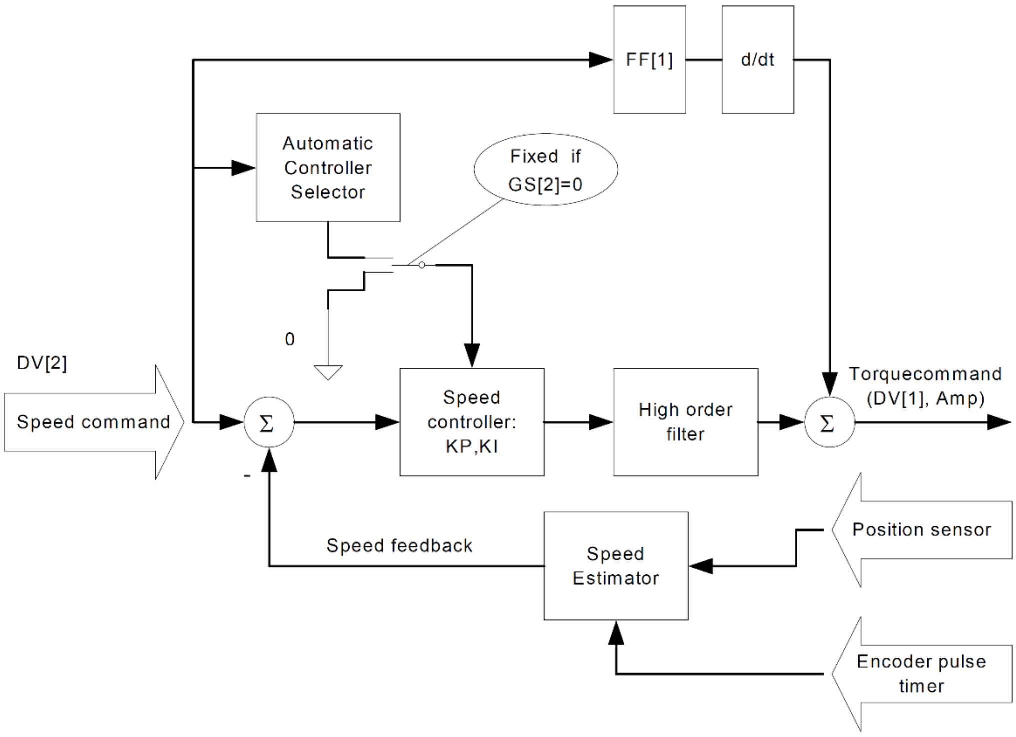

Figure 71 Position controller block diagram [18]

7.2 Code (ELMO Studio)

The following code is used for control of both motors simultaneously. Motor 1 starts on line: ##twomot1 and motor 2 starts on line: ##twomot2.

```
##twomot
int Tsaf,t, T, d,phs_0, phs,spd,f,ph_step,x,m,phs_max,w,i,pos,delta
Tsaf = 20*1e6;//55556*360; //safety time: 20 sec
if m ==1
goto ##twomot1
else
goto ##twomot2
end

##twomot1
m = 1;// motor1
if Tsaf ==0
goto ##twomot
else
goto ##specs // go and read specs
end

##twomot2
m = 2;// motor2
if Tsaf ==0
goto ##twomot
else
goto ##specs // go and read specs
end


##specs // specs
// set specs:

// motor specs:
mo = 0;
px = 0;// reset position
um=5;
ac = 10000000;
dc = 10000000;
sf = 50;

x = 0;// counter initial value
i = 0;

// test specs:
f = 2;// frequency in[Hz]

ph_step = 2.5*100;// step in phase shift
phs_0 = 0*100;// initial phs: 100[counts]=1[deg]
phs_max = 10*100; //maximum phase

d = 5*1e6;// execution time
w = 0*1e6;// wait time
t = 0.1*1e6-d-w+Tsaf;
```

```
phs = phs_0;
##updatephase
t = t+d+w; //update start time
x=x+1; //counter
phs = phs+(i*ph_step);//update phase

if phs<=phs_max
sp  = f*36000;//in [counts/sec]
else
goto ##finish
end
spd = sp;

// add phase shift to motor2
        if m==1
        t = t;// wait time motor1
        goto ##dojob
        else
        t = t +((((phs_0 + i*ph_step)*1e6)/spd));// wait time motor2: wait time motor1 + phase shift time
        goto ##dojob
        end

##dojob
T = t+1*d;// final time

mo=1

        // design controller
        gs[2]=2;
        kp[2]=150;//200;
        ki[2]=100;
        kp[3]=500;//1000;
        ff[1]=10;
        ff[2]=1;

        // give position task
        pa = -d*sp*(1e-6)*x*0.9905; // reference signal
        pos = pa;
        bt=t;
        wait((t-tm)*1e-3);

        i=1;
        phs_0 = 0;
        goto##updatephase


##finish
pa = pos;
bg;
gs[2]=64;
```

Appendix 8 Force measurement

8.1 6-DOF Force sensing module (FSM)

The force sensing module (FSM) to be used (see Appendix 5.2.1) is connected to six 1DOF load cells through six wire flexures (each constraining only one DOF, i.e. in longitudinal direction) in an exactly constraint fashion, enabling it to measure forces and torques in all directions [14]. The configuration is depicted in Figure 72 and Figure 73. The load cells measure the forces transposed to the flexures, hence the following relation exists between the forces acting on the origin $\boldsymbol{F_x}$ and the forces in the flexures $\boldsymbol{F_n}$:

138 $$\boldsymbol{F_x} = A\boldsymbol{F_n}$$

$$with\ \boldsymbol{F_x} = \begin{bmatrix} F_x \\ F_y \\ F_z \\ M_x \\ M_y \\ M_z \end{bmatrix}, \boldsymbol{F_n} = \begin{bmatrix} F_1 \\ F_2 \\ F_3 \\ F_4 \\ F_5 \\ F_6 \end{bmatrix}, A = \begin{bmatrix} 0 & 0 & 0 & -1 & -1 & 0 \\ 0 & 0 & 0 & 0 & 0 & -1 \\ 1 & 1 & 1 & 0 & 0 & 0 \\ 0 & b & -b & 0 & 0 & 0 \\ -a & a & a & 0 & 0 & 0 \\ 0 & 0 & 0 & b & -b & 0 \end{bmatrix}, a = 0.09\ [\mathrm{m}]\ and\ b = 0.08[\mathrm{m}]$$

For a physical interpretation on a and b, refer to Figure 72. For an external load on the platform (see Figure 73), the following applies:

139 $$\boldsymbol{F_x} = B\boldsymbol{F_{ext}}$$

$$with\ \boldsymbol{F_x} = \begin{bmatrix} F_x \\ F_y \\ F_z \\ M_x \\ M_y \\ M_z \end{bmatrix}, \boldsymbol{F_{ext}} = \begin{bmatrix} F_x' \\ F_y' \\ F_z' \\ M_x' \\ M_y' \\ M_z' \end{bmatrix} and\ B = \begin{bmatrix} 1 & 0 & 0 & 0 & 0 & 0 \\ 0 & 1 & 0 & 0 & 0 & 0 \\ 0 & 0 & 1 & 0 & 0 & 0 \\ 0 & -z & y & 1 & 0 & 0 \\ z & 0 & -x & 0 & 1 & 0 \\ -y & x & 0 & 0 & 0 & 1 \end{bmatrix}$$

Between the voltage output of the load cells $\boldsymbol{V_n}$ and the forces in the flexures $\boldsymbol{F_n}$, the following relation exists for this specific FSM (see [14]):

140 $$\boldsymbol{V_n} = S\boldsymbol{F_n}$$

$$with\ \boldsymbol{V_n} = \begin{bmatrix} V_1 \\ V_2 \\ V_3 \\ V_4 \\ V_5 \\ V_6 \end{bmatrix}, \boldsymbol{F_n} = \begin{bmatrix} F_1 \\ F_2 \\ F_3 \\ F_4 \\ F_5 \\ F_6 \end{bmatrix} and\ S =$$

$$\begin{bmatrix} 0.2152 & 0.0010 & -0.0006 & -0.0008 & -0.0003 & 0.0004 \\ 0.0008 & 0.2135 & 0.0009 & 0.0010 & 0.0033 & -0.0012 \\ -0.0001 & -0.0003 & 0.2162 & 0.0004 & 0.0026 & 0.0007 \\ -0.0018 & 0.0008 & 0.0010 & 0.2035 & 0.0068 & -0.0039 \\ 0.0001 & 0.0003 & -0.0036 & 0.0039 & 0.2108 & -0.0005 \\ 0.0015 & -0.0005 & 0.0017 & -0.0086 & 0.0061 & 0.2067 \end{bmatrix}$$

Combining equations138, 139 and140, the following relation applies between an external load $\boldsymbol{F_{ext}}$ and the voltage output of the load cells $\boldsymbol{V_n}$:

141 $$\boldsymbol{F_{ext}} = B^{-1}AS^{-1}\boldsymbol{V_n}$$

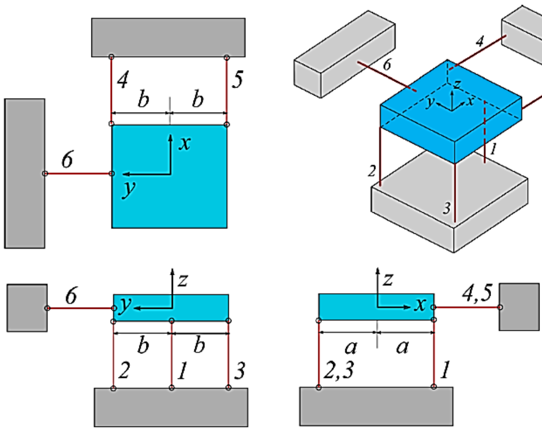

Figure 72 Exactly constrained configuration of the FSM using six wire flexures [14]

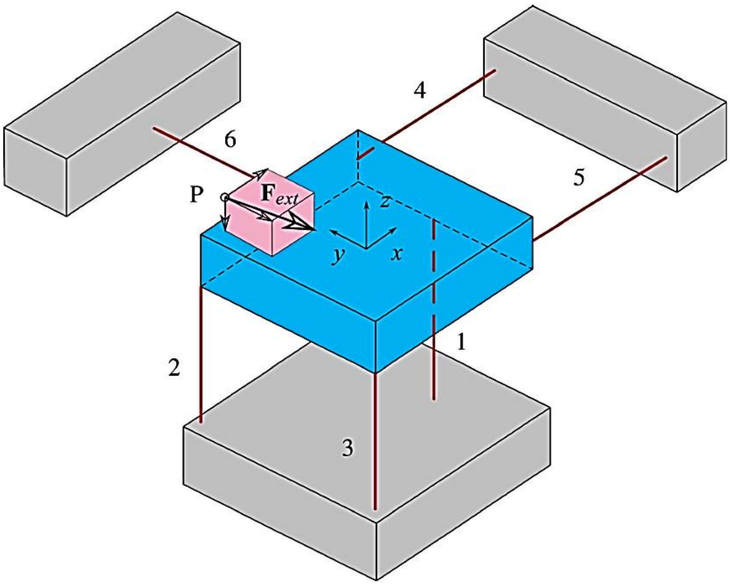

Figure 73 Loading configuration showing the external load applied on the top floating plate of the FSM at point P; F_{ext} includes the external forces and moments [14]

8.2 Determination of aerodynamic loads from measured reaction forces for $f = 1[\mathrm{Hz}]$ and $phs = 7.5[°]$

In this appendix, the procedure as discussed in section 7 is illustrated for $f = 1[\mathrm{Hz}]$ and $phs = 7.5[°]$

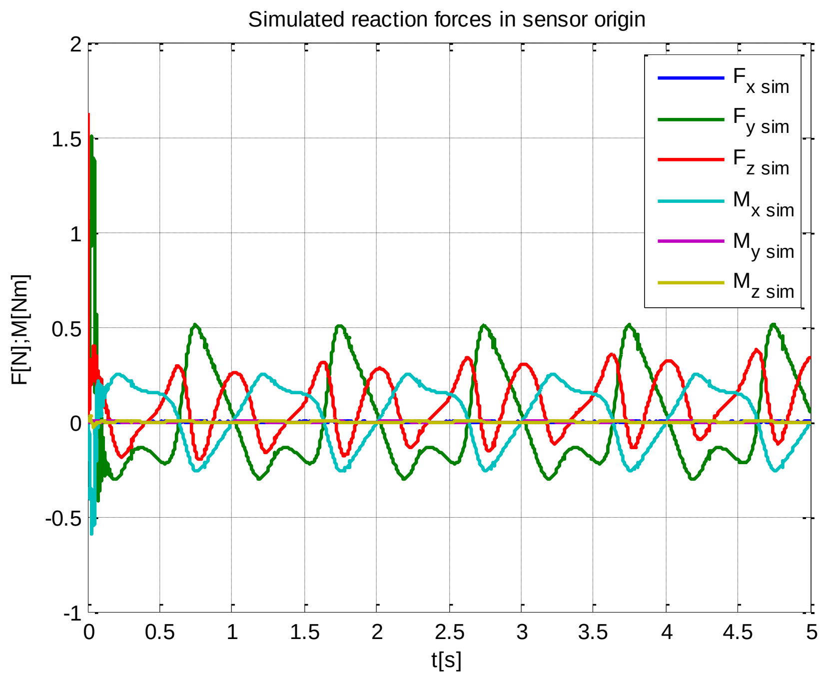

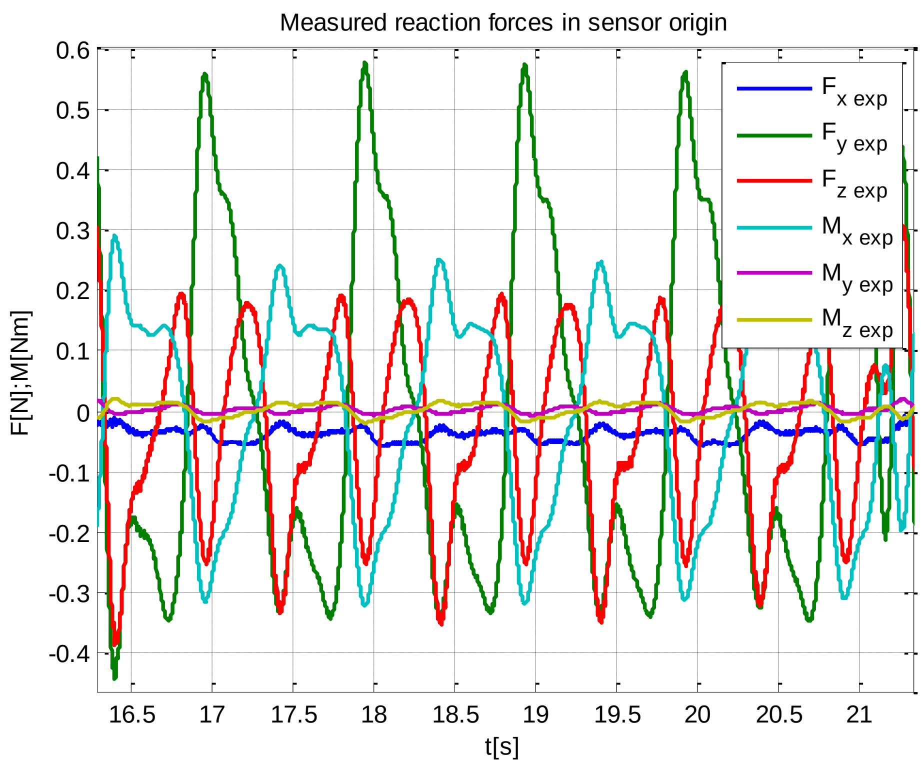

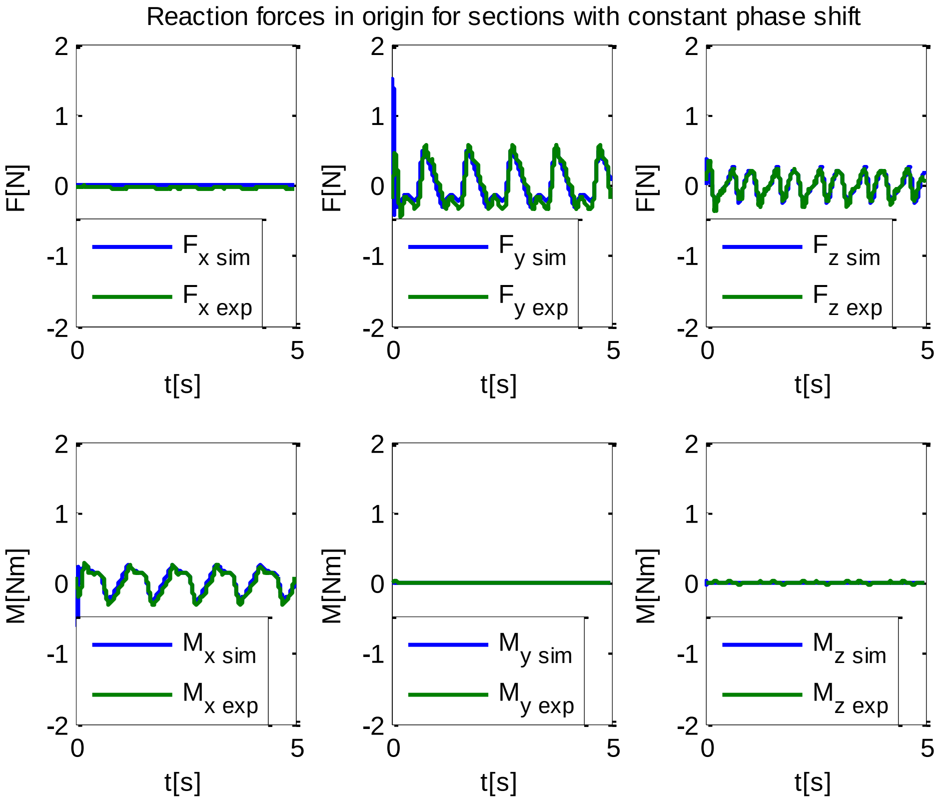
Reaction forces in origin for sections with constant phase shift
F[N]
M[Nm]
t[s]
F x sim
F x exp
F y sim
F y exp
F z sim
F z exp
M x sim
M x exp
M y sim
M y exp
M z sim
M z exp

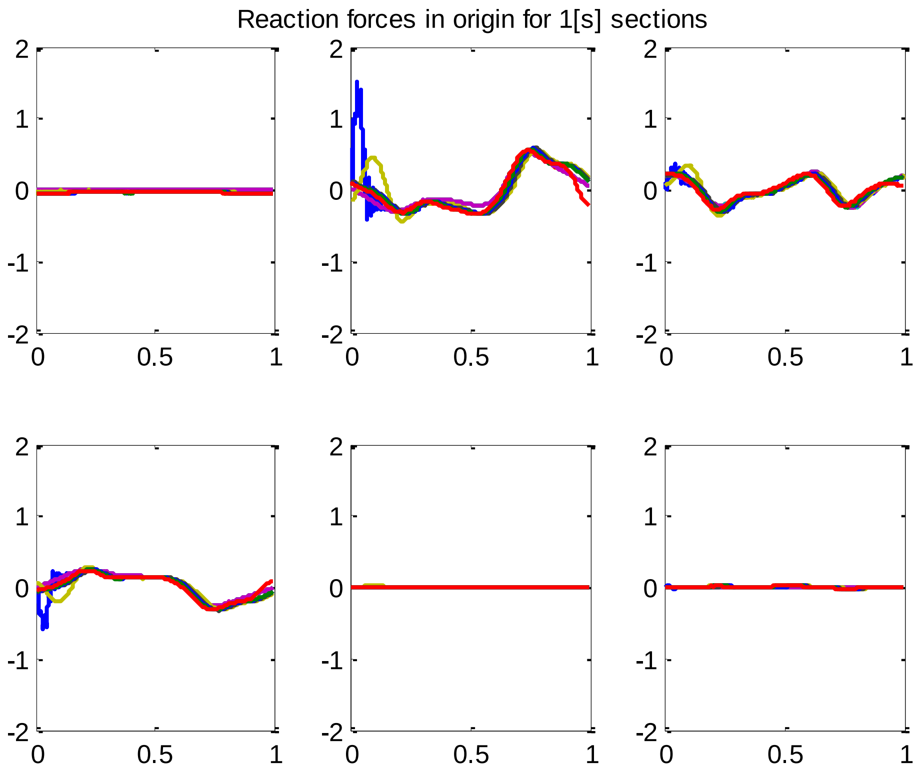
Reaction forces in origin for 1[s] sections

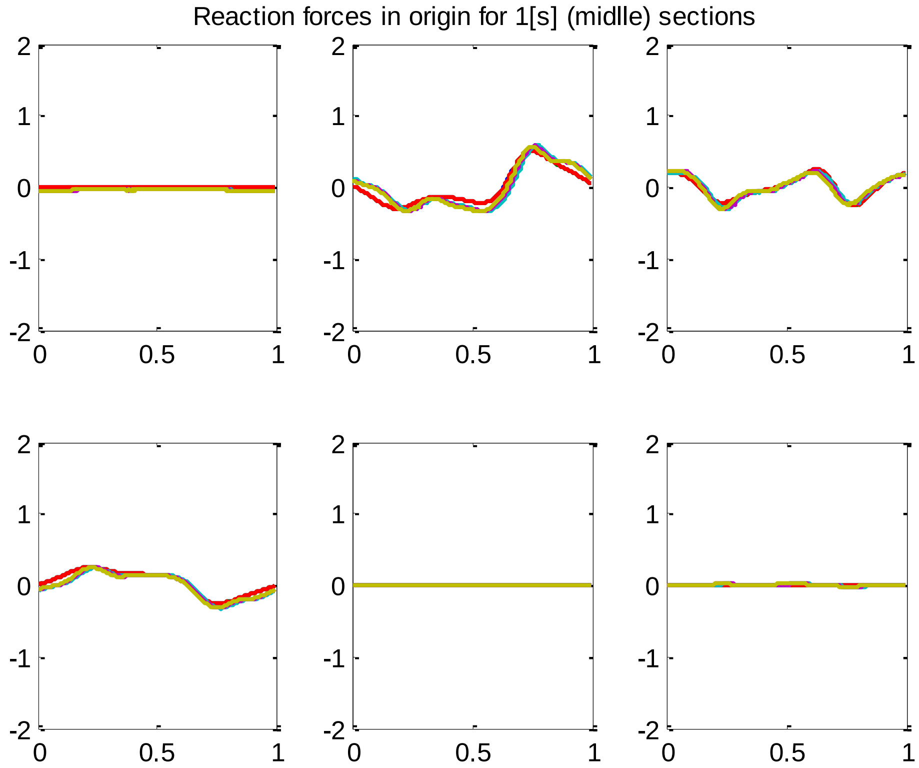
Reaction forces in origin for 1[s] (midlle) sections

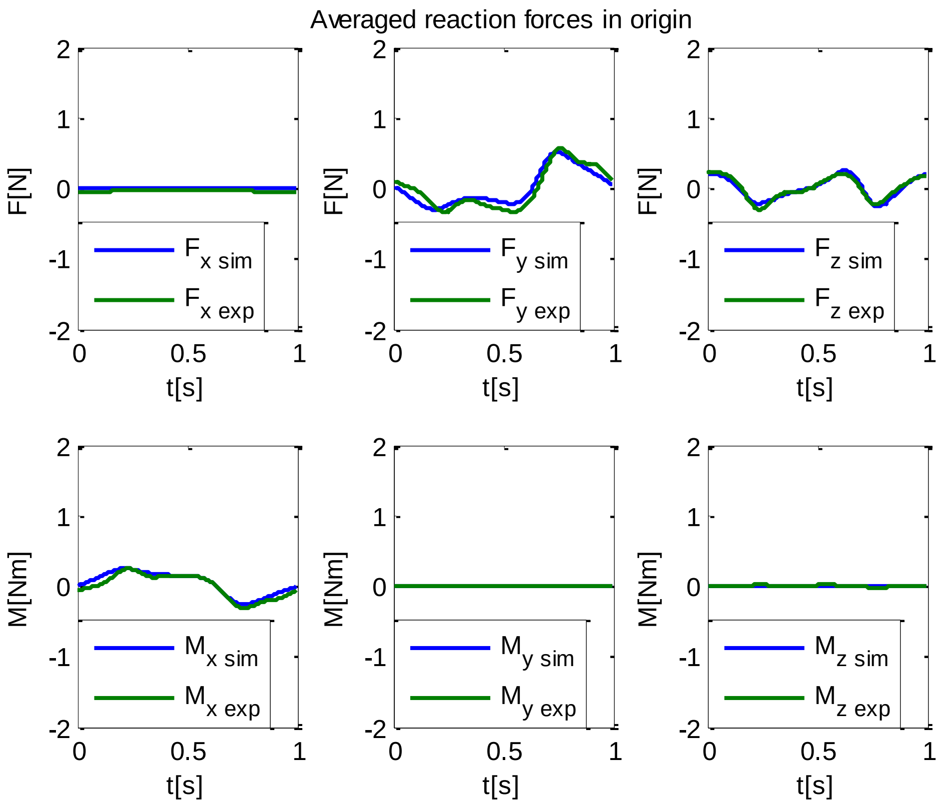
Averaged reaction forces in origin
F[N]
M[Nm]
t[s]
$F_{x\ sim}$
$F_{x\ exp}$
$F_{y\ sim}$
$F_{y\ exp}$
$F_{z\ sim}$
$F_{z\ exp}$
$M_{x\ sim}$
$M_{x\ exp}$
$M_{y\ sim}$
$M_{y\ exp}$
$M_{z\ sim}$
$M_{z\ exp}$

Aerodynamic reaction forces in origin

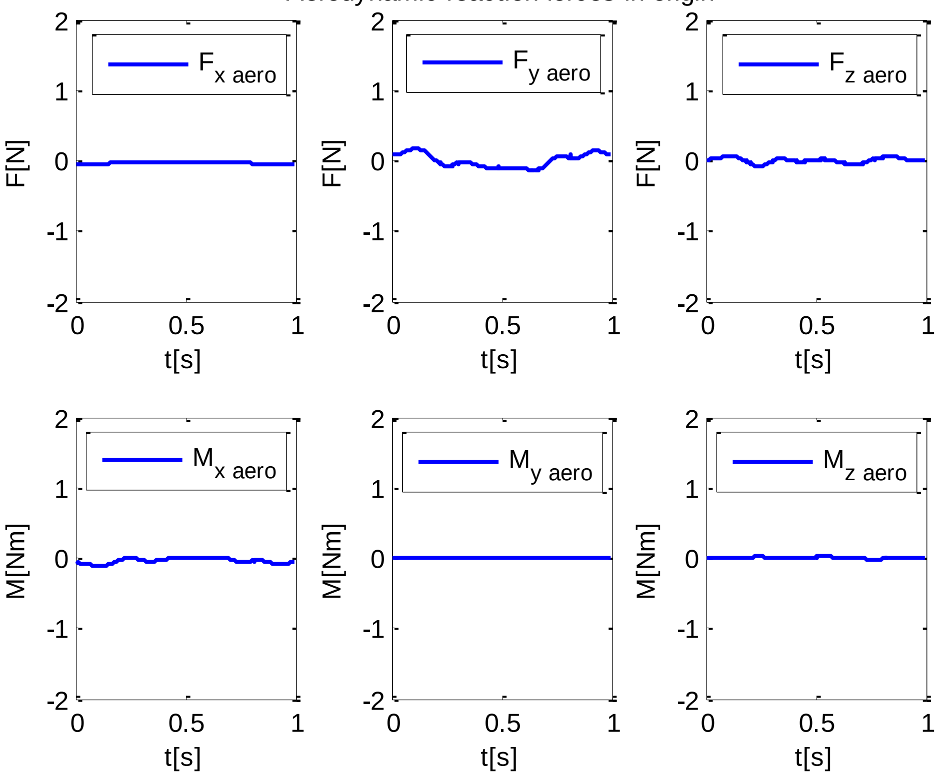

Aerodynamic forces transposed on body center

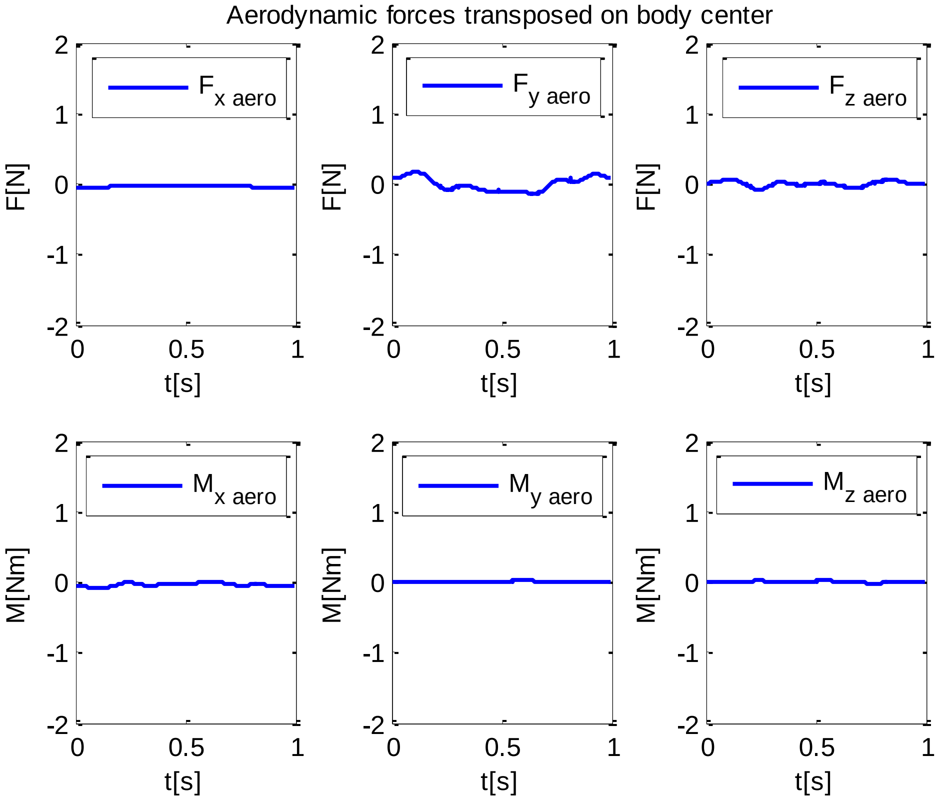

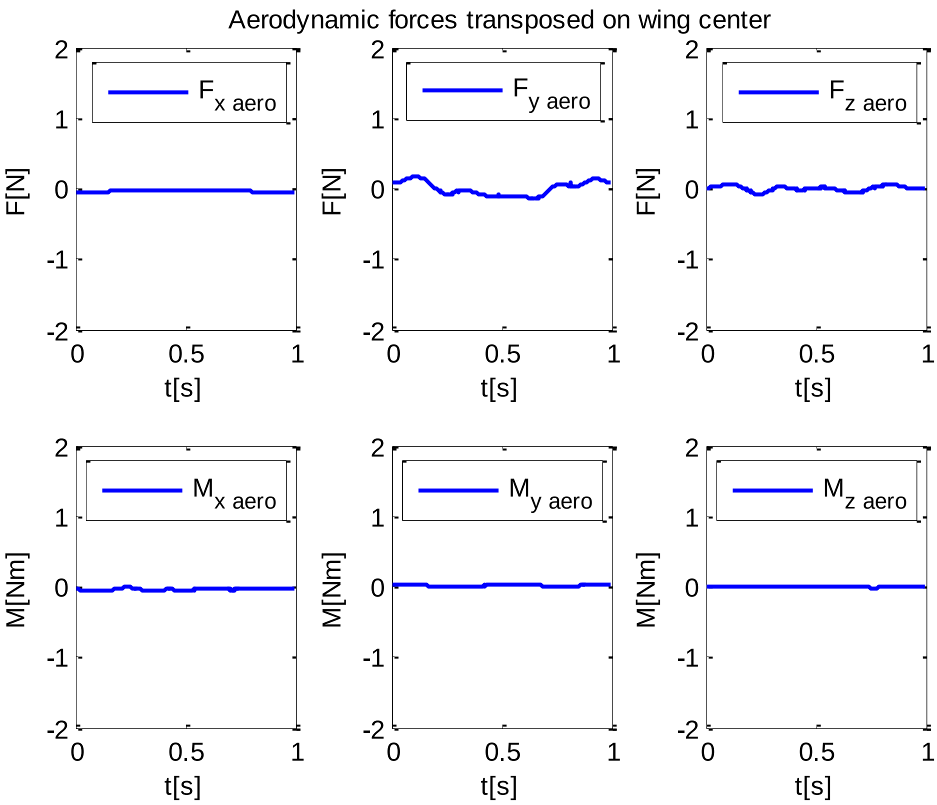

Figure 74 Determination of Aerodynamic loads through measurement and simulation of the reaction forces (see figure titles); $f = 1[\mathrm{Hz}]$ and $phs = 7.5[°]$

Appendix 9 Parts list and Costs

Parts				Amount	Price per unit	Supplier	Subtotal price
Standard parts			Gearbox	2	€ 419,65	Maxon Motor	€ 839,30
			Motor				
			Encoder				
			Controller	2	€ 0,00	UT	€ 0,00
			Force Sensor	1	€ 0,00	UT	€ 0,00
			Bearing	4	€ 16,20	Kuil Nicos	€ 64,80
			Gears	4	€ 19,90	Misumi	€ 79,60
			Circlip	1	€ 0,00	UT	€ 0,00
Manufacturing parts	Laser cutting (and bending)	Delrin Alternative	base plate	1	€ 0	UT	€ 0,00
			disc	1			
			plate	1			
			shackle A	2			
			mount plate A	2			
			mount plate B	2			
			shackle C	1			
			shackle B	2			
		wood	Wooden base plate	1			
	Lathing and Milling parts		key	2	€ 65	RM Precision	€ 130
			pin	2	€ 145		€ 290
			flex pin	6	€ 0	UT	€ 0
			bolt	1			
	Vacuum forming		shell	1	€ 0	UT	€ 0
Parts from Robird			Driveshaft-Pen	4	€ 0	CFS	€ 0
			shim_3x6x0.2	8			
			shim_3x6x0.5	4			
			Circlip-4mm	2			
			Flanger-3mm	8			
			Connecting-Rod	2			
			Wing-Spar-Connector	2			
			Shoulder-Shaft	1			
			Left Wing	1			
Total costs (excluding parts supplied by UT):							€ 1.403,70

Table 2 Parts list and costs for the Robird wind tunnel test setup

Appendix 10 Schedule

Month	March					April				May				June					July				August					September					October				
Tasks / Week	9	10	11	12	13	14	15	16	17	18	19	20	21	22	23	24	25	26	27	28	29	30	31	32	33	34	35	36	37	38	39	40	41	42	43	44	45
Problem understanding\ Design requirements																																					
Conceptual design\ Design proposals																																					
Actual design																																					
Detailed design																																					
Ordering parts & Assembly																																					
Report on the Design																																					
Develop extensive test plan including SI&PE																																					
Familiarization with sofware (Composer software)																																					
System identification and model validation																																					
Controller redesign, implementation and tweaking																																					
Prepare test setup and develop test plans (scripts)																																					
Conduct force measurement experiments																																					
Write final report																																					
Prepare presentation																																					
Graduate																																					

Table 3 Schedule